2013

Effect of thermal annealing and carbon implantation on the functional properties of nanocomposite TiSiN coatings on steel

Mohammad Shoeb Ahmed
Edith Cowan University

Edith Cowan University

Copyright Warning

EDITH COWAN UNIVERSITY
FACULTY OF COMPUTING, HEALTH AND SCIENCE
SCHOOL OF ENGINEERING

Effect of thermal annealing and carbon implantation on the functional properties of nanocomposite TiSiN coatings on steel

By

Mohammad Shoeb Ahmed

Supervisors: A/Professor Laichang Zhang (July 2012- March 2013)
Dr Zonghan Xie (July 2009- July 2012))

This thesis is presented in fulfilment of the requirements for the
Degree of Doctor of Philosophy

March 2013

USE OF THESIS

The Use of Thesis statement is not included in this version of the thesis.

Declaration

I certify that this thesis does not, to the best of my knowledge and belief:

i. incomplete without acknowledgement any material previously submitted for a degree or diploma in any institution of higher education;
ii. contain any material previously published or written by another person except where due reference is made in the text of this thesis; or
iii. Contain any defamatory material.
iv. Contain any data that does not been collected in a manner consistent with ethics approval

I also grant permission for the library at Edith Cowan University to make duplicate copies of my thesis as required.

Signature: Mohammad Shoeb Ahmed

Date: 28/02/13

Acknowledgements

I would like to express my sincere thanks and gratitude to the following people.

First and foremost, I wish to thank Dr. Zonghan Xie, who was my supervisor from July 2009 to July 2012 for his professional guidance, supervision and encouragement during the course of my PhD studies. Dr. Xie, it was a privilege to have you as my supervisor and thank you for imparting your extensive knowledge and experiences on hard and tough ceramic and nanocomposite thin coatings and for all our formal and informal discussions. This project would not have started or finished if it had not been for your diligence and dedication to your role as my supervisors. I also wish to thank to A/Prof. Laichang Zhang for taking over the supervisory role since July 2012 on behalf of ECU for submission of thesis successfully.

I would like to thank Dr. Zhong- Tao Jiang of Murdoch University for all his expert advice and support on the XPS study of TiSiN nanocomposite thin film via e-mail and for the weeks spent in Murdoch University teaching me XPS analysis properly. Dr. Jiang, thank you for responding and supporting me so promptly to all my enquiries and paper revision having a busy teaching schedule.

I would also like to thank to Dr. Zhi- Feng Zhou and Dr. Lawrance K.Y. Li. for this research supported by the 2010 ECU-Industry Collaboration Scheme and the Innovation and Technology Fund (ITF) of Hong Kong (Project No. 9440052 (ITS/082/06)). Dr. Zhi- Feng, thank you so much for always giving the samples for experimentation of this research project and for all your expert advices and support.

A big thank you to all those people who provided extensive technical support, contribution, expert advices and knowledge on this project especially Professor Paul Munroe for approval of 2010 travel grant (TAP 9029) offered by the Australian Microscopy & Microanalysis Facility (AMMRF) for FIB work in UNSW. A big thank to Dr. Xiaoli Zhou for his expert contribution and support on Finite element modelling of TiSiN nanocomposite coatings in this project.

Thank you to Dr. Magdalena Warjack for her expert contribution and support in the corrosion characterization of TiSiN nanocomposite thin coating during the busy teaching schedule.

Thank you to Wlliam Rickard of Curtin University for the technical support and advice during the use of FIB-SEM during the microstructural characterization of the nanocomposite coating.

Thank you to Hua Guo, my research colleague for his remarkable support in this research.

I thank to Edith Cowan University for the provision of a scholarship to support my research.

And last but not least, a big thank you to my entire colleagues, my wife and my parents for their endless support and understanding during the course of my studies.

List of Abbreviations

A	Area of contact at indentation
AFM	Atomic force microscopy
AgCl	Silver chloride
Al	Aluminium
AlN	Aluminium nitride
Ar	Argon
At.%	Atomic percentage
Au	Gold
a	Radius of contact
a-Si_3N_4	Amorphous silicon nitride
α	Co-efficient of Thermal expansion
bcc	Body centred cubic
BF	Bright field
C	Carbon
CN	Carbo-nitride
Cr	Chromium
CrN	Chromium nitride
CrNi	Chromium nickelide
Cu	Copper
CVD	Chemical vapour deposition
°C	Degree celcius
ΔT	Change of temperature
ΔE	Polarization resistance
Δi	Polarization current
DF	Dark Field
d	Grain size
d_c	Critical Grain size
2D	Two-dimension
3D	Three dimension
E	Elastic modulus
E_B	Binding energy
ECR	Electron cyclone resistance
E_{corr}	Corrosion potential
EDX	Energy dispersive X-ray
EM	Electro magnetic
eV	Electron volt
FESEM	Field emission scanning electron microscope
FIB	Focused Ion beam
GeV	Giga electron volt
GI-XRD	Grazing incident X-ray diffraction
GPa	Giga Pascal
H	Hardness
H_2	Hydrogen
H_{max}	Maximum hardness
HNO_3	Nitric acid
HCl	Hydrochloric acid
H_2SO_4	Sulfuric acid
h	Depth of indentation
Kr	Kripton
kV	Kilovolt
KeV	Kilo electron volt
K/s	Kelvin per second
KN	Kilo-newton

λ	Wavelength
Mn	Manganese
Mo	Molybdenum
MEVVA	Metal vapour vacuum arc
MN	Mega-newton
µm	Micrometre
mbar	milibar
mN	Milinewton
N	Nitrogen
NaCl	Sodium chloride
nc-TiN	Nanocrystalline titanium nitride
nm	Nanometre
ν	Poisson's ratio
O_2	Oxygen
P_{max}	Maximum load
pA	Pico-ampere
Pt	Platinum
PVD	Physical vapour deposition
P_g	Gas pressure
R	Indenter radius
RF	Radio frequency
R_P	Polarization resistance
S	Contact stiffness
SEM	Scanning electron microscopy
Si	Silicon
SiC	Silicon carbide
$SiCl_4$	Silicon chloride
σ	Stress
σ_R	Residual stress
σ_T	Thermal stress
σ_Y	Yield stress
TEM	Transmission electron microscopy
T_g	Gas temperature
Ti	Titanium
TiC	Titanium carbide
TiN	Titanium nitride
TiSiN	Titanium silicon nitride
TiAlN	Titanium aluminium nitride
TiAlSiN	Titanium aluminium silicon nitride
TiO	Titanium mono oxide
TiO_2	Titanium di oxide
TiB_2	Titanium boride
$TiCl_4$	Titanium chloride
UHV	Ultra high vacuum
U_k	Kinetic energy
UV	Ultra violet
V	Volume of the gas
V	Vanadium
W	Tungsten
WC	Tungsten carbide
W	Elastic recovery
WS	Scratch width
XPS	X-ray photo spectroscopy
XRD	X-ray diffraction
Xe	Zenon
Zr	Zirconium

TABLE OF CONTENT

LIST OF PUBLICATIONS

Type of publication	Number	References
Papers in referred Journals	5	1-5

1. Ahmed, M.S., Xiaoli, Z., Zhou, Z.F., Munroe, P.R., Tan, N.C., Lawrence, K.Y. Li., Xie, Z.H., Effect of Thermal Annealing Upon Residual Stress and Mechanical Properties of Nanostructured TiSiN Coatings on Steel Substrates, Journal of the American Ceramic Society, 94 (2011) 1546-1551.(Chapter 2)

2. Ahmed, M.S., Zhou, Z.F., Munroe, P.R., Lawrence, K.Y.Li., Xie, Z.H., Control of the damage resistance of nanocomposite TiSiN coatings on steels: roles of residual stress. Thin Solid Films, 519 (2011) 5007–5012.(Chapter 3)

3. Ahmed, M.S., Xiaoli, Z., Zhou, Z.F., Munroe, P.R., Lawrence, K.Y. Li., Jiang, Z.T., Rickard, W., Xie, Z.H., Corrosion behaviour of nanocomposite TiSiN coatings on steel substrates. Corrosion Science, 53 (2011) 3678-3687. (Chapter 4)

4. Ahmed, M.S., Xiaoli, Z., Munroe, P.R., Jiang, Z.T., Guo, H., Warjack, M., Rickard, W., Xie, Z.H., Corrosion- and Damage-Resistant Nitride Coatings for Steel, Journal of the American Ceramic Society, 95 (2012) 2997–3004. (Chapter 5)

5. Ahmed, M.S., Xiaoli, Z., Munroe, P.R., Jiang, Z.T., Xie, Z.H., Effect of carbon implantation on the TiSiN nanocomposite thin film, Journal of the American Ceramic Society.(Submitted) (Chapter 6)

Abstract

This PhD research contributes to the part of advanced materials technology. The machining industry currently faces tremendous pressures with the need for durable cutting tools suitable for eco-friendly high speed machining operations becoming acute. In this thesis innovative design and synthesis strategies are explored to tailor the properties of nanocomposite coatings. Advanced characterisation techniques are applied to identify the mechanisms that control the mechanical, tribological, and corrosion behaviours of these coatings. Cutting tools protected by these coatings are anticipated to exhibit a unique combination of superior toughness and greater resistance to wear and corrosion, providing significant economic and environmental benefits.

The thin ceramic coatings are commonly applied to various kinds of steel cutting and machining tools to enhance their mechanical and tribological properties. The most common ceramic coating is TiN. But the major issues that hamper the application of TiN are high friction co-efficient (typically~0.5), lower hardness, lower thermal stability (~500^0 C) and lower corrosion resistance.

To address some of these problems, TiSiN nanocomposite coatings are developed, which have super-hardness, better thermal stability (~1000^0C) and better corrosion resistance. But the as-deposited TiSiN coating still has high co-efficient of friction (~0.4) and high residual stress (~7-9 GPa) which consequently affect the adhesion and toughness of the coating. This project aims to address these problems by (a) the application of carbon implantation to modify the structure and chemistry of the surface layer of the nanocomposite coatings with reduced friction and residual stress; and (b) thermal annealing of the nanocomposite coating to reduce the residual stress with enhanced fracture toughness, better corrosion resistance and more thermal stability.

In addition, the role of microstructure, residual stress and defects of these hard coating in corrosive environment will be studied. For this research, a combination of microstructural and mechanical properties characterization, corrosion analysis, tribological test and finite element modelling facilities will be used. The study includes focused ion beam (FIB) milling and transmission electron microscopy (TEM), Synchrotron X-Ray Diffraction (XRD), X-ray Photo Spectroscopy (XPS), Energy dispersive X-Ray (EDX), nanoindentation, nano-scratching, potentio-dynamic polarization cell and Atomic force microscopy(AFM).

1. Introduction

Nanocomposite coatings represent a new generation of materials. Nanocomposite thin films comprise at least two phases, where the matrix can be either nanocrystalline or amorphous phase. The nanocomposite materials, due to (1) very small (≤10 nm) size of grains from which they are composed and (2) a significant role of boundary regions surrounding individual grains, behave in a different manner compared to that of the conventional materials with grains greater than 100 nm, and so they exhibit completely new properties[1-6]. The general characteristics of nanocomposite coating are a host material with another material homogenously embedded in it, with one (or both) of these materials having a characteristic length scale of 1-10nm as shown in the fig.1. An example is given in this figure, where 5-10nm TiN nanocrystals are embedded into an amorphous phase of Si_3N_4 to reach a super-hardness of 40 GPa [7, 8]. At present, it is developed by many researchers that -

1. There are two groups of hard (H≥20 GPa) and superhard (H≥40 GPa) nanocomposites: (i) nc-MeN/ hard phase and (ii) nc-MeN/Soft phase.
2. Nanocrystalline and / or X-ray amorphous films are created in transition regions between (i) the crystalline phase and the amorphous phase, (ii) two crystalline phases and/ or (iii)two different crystallographic orientations of grains of the same material.
3. There are huge differences in the microstructure of single-and two-phase films: here nc- denotes the nanocrystalline phase and Me = Ti, Zr, Ta, Mo, W, Cr, Al, etc. are elements forming nitrides.

Using these findings a complete concept of nanocomposites with enhanced hardness was developed. This concept is based on the geometry of nanostructured features, i.e. on the size of grains and the shape of crystallites.

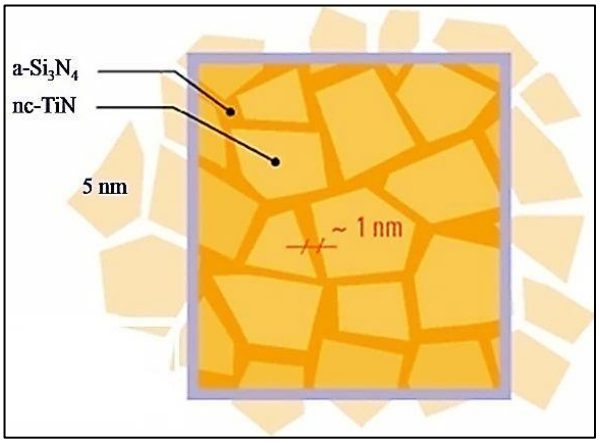

Figure1: The microstructure of TiSiN film shows nanocrystallites of TiN embedded in Amorphous Si_3N_4 phase [6].

1.1 Design of nanocomposite microstructure and origin of enhanced hardness

Nanocomposite thin films represent a new class of materials which exhibit special mechanical, electronic, magnetic and optical properties due to their size-dependent phenomena[1]. Many experiments clearly demonstrate that nanocrystalline and nanophase materials which are composed of small (≤10 nm) grains exhibit enhanced properties such as mechanical (hardness), tribological (friction), physical (field emission in ultra-nanocrystalline diamond, elements solubility, thermal conductivity, photocatalytic effect), optical, electrochemical, etc. These enhanced properties occur in the case when the grain boundary regions start to play a comparable or even dominant role over that of grains. Qualitatively new processes, such as grain boundary interaction, grain boundary enhancement or sliding, result in new unique physical and functional properties [9, 10]. Enhanced properties of nanophase materials do not meet the rule of mixture. For example, hardness of two-phase nanocomposite coating H_n is given by the following inequality [3]

$$\boldsymbol{H_n > (1 / V_n)(H_1V_1 + H_2V_2)} \qquad (1)$$

where H_1, H_2 and V_1, V_2 are the hardness and the volume of the first and second phase, respectively and V_n is the total volume of the nanocomposite coating. A maximum value of the enhanced hardness H_n can be more than two times greater than that of the harder component of the nanocomposite. Main mechanisms, which are responsible for the hardness enhancement, are (1) dislocation-dominated plastic deformation, (2) cohesive forces between atoms and (3) nanostructure of materials [6]. The magnitude of enhancement depends on processes operating in the material at a given range of the size d of grains of nanocrystals in nanocomposite. There is a critical value of the grain size $d_c \approx$ 10 nm at which a maximum value of H is achieved. A region around the maximum H_{max} at $d = d_c$ correspond to a continuous transition from the operation of intergranular processes at d>dc, dominated by dislocation activity and described by the Hall-Petch law ($H \sim d^{-1/2}$) to that of intergranular processes and at $d<d_c$ dominated by a small-scale sliding in grain boundaries.

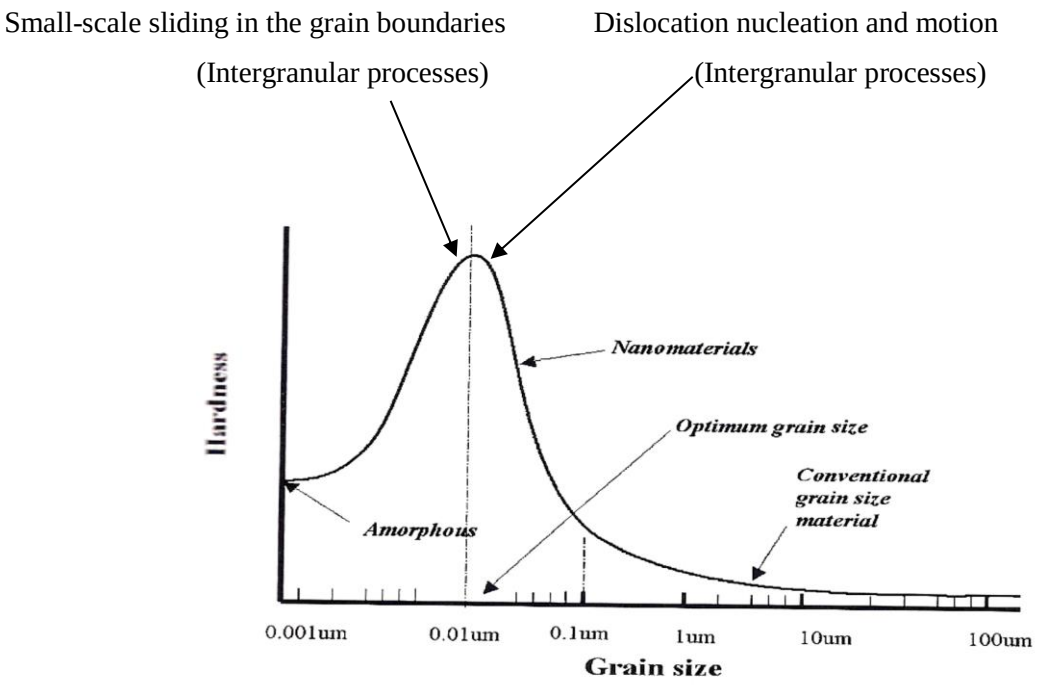

Figure 2: Hardness of material is shown as a function of grain size. When grain size is less than the optimum value (10 nm), hardness increases for grain boundary sliding. When grain size is higher than the optimum value (10 nm), the hardness is dominated by dislocation nucleation and motion [6].

In materials with d≤ 10 nm(1) the amount of atoms in grain boundary regions is greater than approximately 10% of that in nanograins and (2) dislocations already do not form and so besides chemical bonding namely a nanostructure of materials start to play a dominant role. The properties of nanocomposite materials strongly depend on the size of grains, their chemical composition, crystallographic orientation and lattice structure [6]. Therefore, the hardness enhancement can be explained by an existence of a mixture in nanocomposite comprised of at least two different kinds of grains[11].

Apart from hardness, good mechanical properties also include high toughness. High toughness can be obtained in nanocomposite thin films through the nanosize grain structure as well as deflection, meandering and termination of nanocracks. Veprek proposed a design concept for novel superhard ceramic/ ceramic nanocomposite coatings with high toughness [8, 11]. In this design, multiphase structure is used to maximize the interface complexity and ternary or quaternary systems with strong tendency of segregating into binary compounds used to form sharp and strong interface to avoid grain boundary sliding [7, 12]. The crystallite size is controlled to approximately 3-4 nm and the separation distance between crystallites maintained at less than 1 nm. Based on this design concept, Veprek and co-workers prepared nc-TiN/a-Si_3N_4/a & nc-$TiSi_2$, nc-TiN/a-Si_3N_4, nc-TiN/a-BN/a-TiB_2 super-hard nanocomposite coatings by

means of Plasma CVD. In order to obtain super-hardness, usually plastic deformation is strongly prohibited; dislocation movement and grain boundary sliding are prevented, thus probably causing a loss in ductility [13]. A certain degree of grain boundary sliding is necessary in order to improve the toughness of the nanocomposite coatings [14]. Usually, to overcome the brittleness of ceramic bulk materials, a second ductile phase is incorporated to improve the toughness of the nanocomposite coating [15].

1.2 Synthesis of thin nanocomposite Coating

Generally nanocomposite thin films can be prepared by Chemical vapour deposition (CVD) or Physical vapour deposition (PVD) techniques [16-18]. These groups can be divided in sub-groups and methods:

Physical vapour deposition (PVD):

I. Thermal evaporation
   - Pulsed laser deposition
   - Electron beam deposition

II. Sputter deposition
   - Magnetron sputtering
   - Ion beam sputtering

III. Arc vapour deposition
   - Vacuum arc deposition
   - Filtered arc deposition

IV. Ion implantation
   - Ion beam deposition

Chemical vapour deposition (CVD)

- Plasma enhanced CVD
- Plasma assistant CVD
- Electron cyclotron resonance
- CVD(ECR-CVD)

Different techniques are now available for the preparation of nanocomposite thin films. The most promising methods are chemical vapour deposition (CVD) and magnetron sputtering, although other methods such as Laser ablation, Thermal evaporation, ion beam deposition and ion implantation are also used by various researchers. High deposition rate and uniform deposition for complicated geometrics are the advantages of the CVD method compared to physical vapour deposition [8, 18]. However, the main concern for the CVD method is that the

precursor gases, $TiCl_4$, $SiCl_4$ or SiH_4, may pose problems in production because they are corrosive in nature and are fire hazards [6, 17]. Moreover, the incorporation of chloride in protective films may induce interface corrosion problems during exposure to elevated temperatures under working condition. For most applications, a low deposition temperature is required to prevent substrate distortion, substrate phase transformation and loss of mechanical properties [19, 20]. This is difficult to realize in the CVD process. These disadvantages can be overcome by the physical vapour deposition process [21]. The term Physical Vapour Deposition (PVD) describes an atomic deposition process at a relatively low temperature [22] . Originally, PVD was used to deposit metals by transport of vapours or gases in a vacuum, without involving a chemical reaction. The vapour is then transported between the source and substrate. After that, the condensation of vapours followed by film nucleation and growth on the surface of the substrate occurs. It is well known that low temperature PVD coating processes have been adopted to deposit TiSiN-based coatings onto steel substrates because the deposition temperature is limited to less than ~550°C, above the temperature at which phase transformation generally occurs in substrate steels [23]. As a result, post-coating treatment of steel substrates can be avoided and there is no dimensional change, which would be detrimental for the production of precision tooling [24]. Also, PVD processes are capable of producing both dense and adherent coating layers onto various substrates with little or no porosity and chemical compositions similar to that of the target [25]. Significant effort has been devoted to the preparation of nanocomposite thin films using magnetron sputtering since this technology is a low temperature and far less dangerous method compared to CVD [26, 27]. Also it is easily scalable for industrial applications. In magnetron sputtering, energetic ion bombardment is used to vaporize the source material, often referred to as the target, as shown in the figure 3.

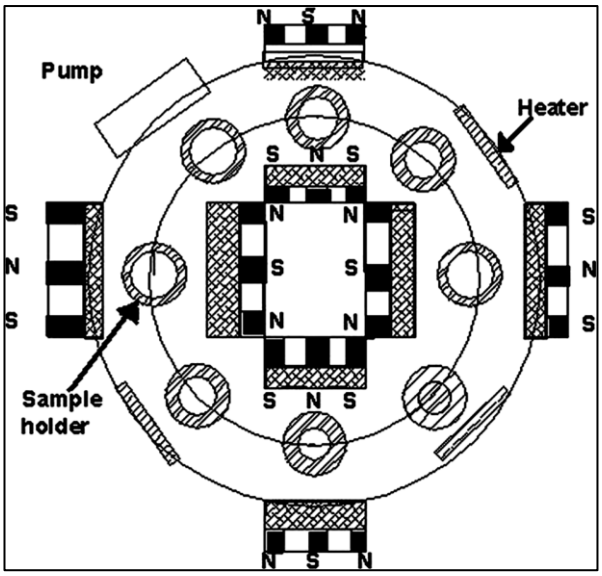

Figure 3: Schematic cross-sectional view of the closed field unbalanced middle frequency magnetron sputtering system [28].

The deposition system is filled with a noble gas, often argon, to a total pressure of 0.01 to 0.1 mbar. A negative potential of some kV is applied to the target. Positive ions naturally occurring in the gas will therefore be accelerated towards the target. When they impinge on the target, they transfer their momentum to surface atoms of the target, and if the value of the momentum in both directions is higher than the surface binding energy, a target atom will be sputtered. This sputtered flux of target atoms, which has a main direction, is then transported through the space towards the substrate [29, 30]. Depending on the gas pressure and the distance between substrate and target, the flux will be more or less scattered by the gas [31-33]. The average distance an atom can travel before a collision is called the mean free path. The mean free path L_m can be measured through:

$$\boldsymbol{L_m = \ kT_g \ / \sqrt{2}\pi P_g d g^2} \qquad (2)$$

where k is the Boltzman constant, T_g and P_g the gas temperature and pressure respectively, and the diameter of the gas molecule(d_{Ar} = 0.364 nm). During sputtering process, the film surface is ion bombarded, which can densify the growing film by enhancing the surface atom mobility. In addition, ion bombardment of the growing film can restrict the grain growth and permit the formation of nanocrystalline. The size and crystallographic orientation of grains can be controlled by the energy of bombarding ions [34]. Kinetic energy of ionized particles can be estimated by:

$$\boldsymbol{U_k \propto D_W V_S P_g^{1/2}} \qquad (3)$$

where U_k is the kinetic energy, D_w the target power density, V_S the substrate bias and P_g the gas pressure.

Magnetron sputtering is a very efficient method for a production of nanocomposite films. The nanocomposite films are formed in consequence of a combined action of four processes: (1) low-energy ion bombardment, (2) element mixing, (3) substrate heating and (4) energy released or consumed during the film formation[17, 35].Main advantages of the magnetron sputtering are the following: (1) the sputtering is a non-equilibrium process at anatomic level which makes it possible to replace a substrate heating (T_S) with the particle bombardment (E_p) and to form films at low Ts even close to the room temperature (RT); here T_s and E_p are the substrate temperature and the energy delivered to the growing film per condensing particle, respectively, (2) no problem in sputtering of alloys and their compounds, such as nitrides, carbides, etc., (3) condensing atoms have a high energy (several eV compared with approximately 0.1 eV in evaporation process) what enables (i) to form high-temperature phases on unheated substrates due to high cooling rates (~10^{14} K/s) and (ii) to perform a

selective reactive sputtering of nitride of alloys, i.e. to form a nanocomposite of the type nc-MeN / metal, due to a difference in the nitride decomposition temperatures for the element A and B of alloy AB; here nc- denotes the nanocrystalline phase and Me=Ti, Zr, Cr, W, Mo, etc., and (4) magnetrons can be easily scaled up into big industrial coating machines [35, 36]. For sputtering of nanocomposite coatings three basic sputtering systems can be used: (1) one magnetron with an alloyed target, (2) two magnetrons equipped with the targets made of different (i) metals (e.g. Ti, Si), (ii) alloys (e.g. TiAl, CrNi), (iii) compounds (e.g. TiB_2, $TaSi_2$) or their combinations, or (3) pulse operated dual magnetron which can easily control individual elements in the alloy film or makes it possible to deposit non-conductive materials at high deposition rates. Hard nanocomposite films are usually prepared by a reactive magnetron sputtering, i.e. the magnetron cathode (target) is sputtered in a mixture of Ar and reactive gas (nitrogen, oxygen, etc.)[37-39].

1.3 Thermodynamics of TiSiN nanocomposite formation

The generic design concept for the preparation of superhard nanocomposites with a high thermal stability and oxidation resistance is based on a strong, thermodynamically driven phase segregation in a binary (or ternary) system, that results in the formation of a nanostructure with "compositional modulation" with a sharp and strong interface[8, 13, 23, 40, 41]. The spinodal nature of the segregation of the TiN and Si_3N_4 phases during the deposition of the nc-TiN/a-Si_3N_4 nanocomposite, consisting of 3–4 nm small TiN nanocrystals "glued" together by about one monolayer of X-ray amorphous silicon nitride. When deposited under the conditions of a sufficiently high nitrogen pressure (0.3–1 mbar) that provides the thermodynamic driving force and sufficiently high temperature (≥550 ◦C) that assures the diffusion rate-controlled phase segregation to be completed during the deposition, the crystallite size is fairly uniform. The spinodal nature can be provided by thermodynamic calculations of the Gibbs free energy of the mixed phases as a function of their relative fraction which yields the "chemical spinodal" curve (i.e. the second derivative of the Gibbs free energy of the mixed system is negative) for the TiN/Si_3N_4 system consisting of immiscible, stoichiometric nitrides [23, 40]. In the case of the nanocomposites formed by spinodal decomposition, an isotropic nanostructure with sharp interfaces is formed automatically if the necessary thermodynamic (high chemical activity) and kinetic (sufficiently fast diffusion) conditions are met [23, 42, 43]. When nanocomposites are deposited from the vapour phase the transition metal nitride will nucleate to form the crystalline phase. In absence of elements leading to the formation of amorphous phases (e.g., silicon), the formation of the crystalline phase follows the known growth modes such as elongated crystals with preferred orientations. The addition elements of leading to amorphous phases, however,

drastically influences the growth mode of the crystalline phase. These grains continue to grow until parts of their surface become covered by the co-deposited amorphous phase. In the case of a-Si_3N_4 (at sufficient ion energy) this materials are diffusion barriers; the underlying grain thus is no longer exposed to the particle flux from the plasma leading to grain growth. As a consequence newly arriving crystallite-forming species will nucleate and in this way lead to reduced grain size. The higher the fraction of the amorphous phase is the faster the growing crystallites are covered with the amorphous phase [16, 21].

1.4 TiSiN coating microstructure

The structural designing of the nanocomposite TiSiN coating is based on their structure-properties relationship. The observed excellent properties of Ti-Si-N films are believed to depend strongly on their unique microstructures, namely, the crystalline TiN grains were surrounded by a thin amorphous Si_3N_4 layer when Si was incorporated into a growing TiN film under suitable deposition conditions [37, 39, 45-50]. The thin amorphous Si_3N_4 layer can serve as a barrier to grain growth and dislocation movement, and thus the mechanical properties and thermal stability of the formed nanocomposite TiSiN films are improved [12, 34, 51, 52].

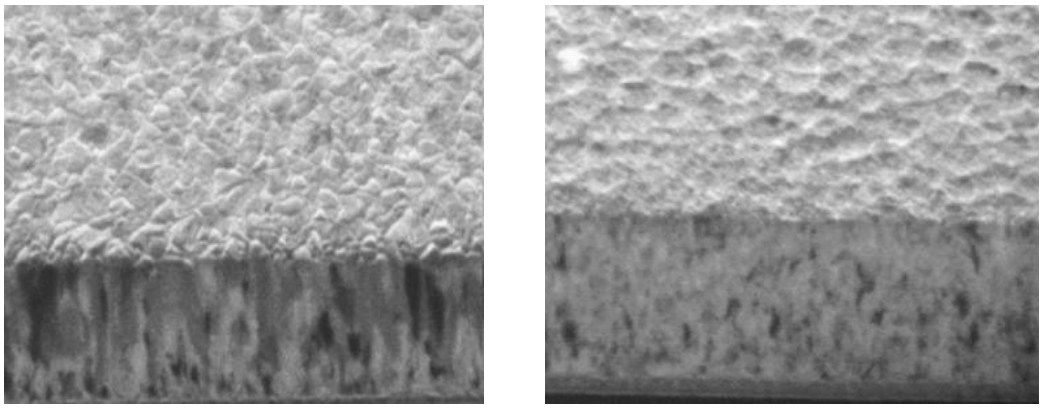

(a) (b)

Figure 4: The cross-sectional image: (a) the columnar grain morphology of TiN film on the substrate, (b) the addition of 5% Si changes the columnar grain to more dense microstructure in Ti-Si-N coating [43].

The crystallite growth of titanium nitride is not restricted by amorphous silicon nitride and forms therefore relatively large crystallites. The introduction of minor amounts (2 at.%) of an amorphous phase, such as silicon nitride, leads to an encapsulation of the growing TiN crystallites and thus prevents their further growth. The TiN crystallite size is constant at about 7–8 nm and coexists with silicon nitride, which covers the crystallite. This is probably the

regime where the system minimises its free energy by maximising the area of the nc-TiN/a-Si_3N_4 interface (i.e. the fraction of the atoms at the interface) and where maximum hardness is found. This is known as the percolation threshold. As the silicon content is raised above 8 at.% there is a slight decrease in the grain size to about 5 nm, however the separation between grains increases to a point where the interaction between the two phases is lost and the hardness reduces. Liu et al. reported on a Monte Carlo simulation of the microstructure of TiN/SiN_x films that showed the preference of SiNx adherence to the TiN grain boundary due to the driving force caused by the energy difference between TiN grain-boundary energy and TiN/SiN_x interfacial energy. They also modelled the evolution of the TiN grain size with increasing SiNx showing the average grain size of TiN decreases with the increase of the volume fraction of SiN_x [50]. Their simulation results show a good agreement with their experimental data. In the Ti–Si–N coating, the TiN layer grew in columnar structure as in the TiN coating.

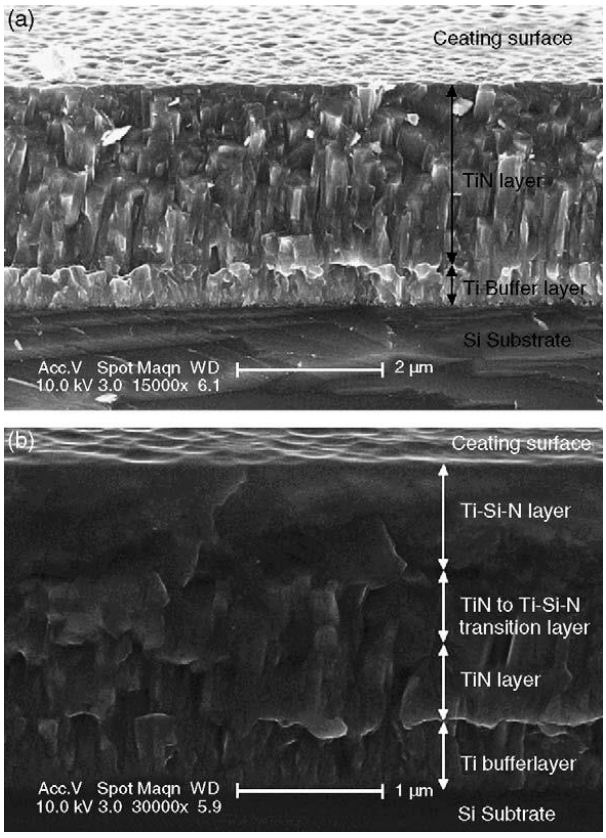

Figure 5 : Cross-sectional morphologies of (a) the TiN coating and (b)the Ti–Si–N coating (8.6 at.% Si) [27].

The transition layer also shows an obvious columnar feature, while the Ti–Si–N layer shows much denser structure than the TiN layer and no columnar features can be seen. The structure changed abruptly from the columnar structure to denser structure as the Si content increased to 5~8.6 at.% (Fig.4 & Fig.5). As the Si content increased to 3.7 at.% and 6.0 at.%,

columns still can be found. But the length and the diameter of the columns decrease as compared with the TiN coating. In the coating with Si content of 6.7 at.%, columns disappear and the coating shows a granular structure. As the Si content increased to 8.6 at.%, neither columnar structure nor granular structure can be seen, and the coating shows more denser than the coatings with less Si content [27, 43, 46]. Flink observed in-between the Ta–Si layer and the TiSiN film, there is a ~100 nm broad recrystallized band of TiN with grain size ~200 nm and without porosity. The film thickness has decreased from 2.0 to 1.5 mm during annealing at 1200 °C because of the diffusion of Ti, Si, and N from the film into the substrate [53] (Fig.6).

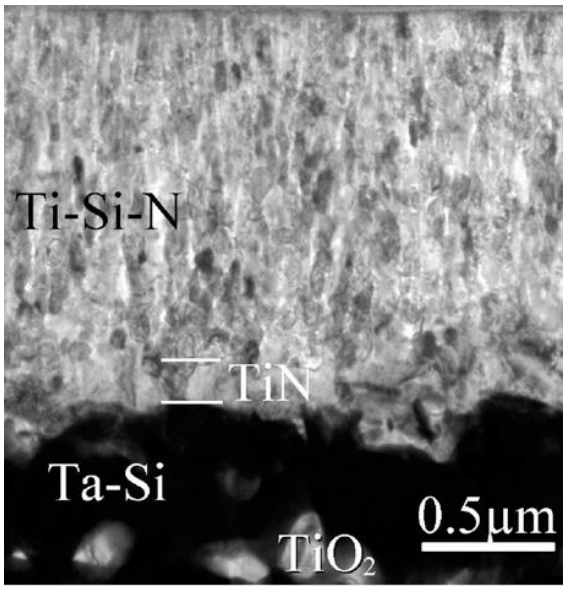

Figure 6: Bright field electron micrograph- FIB image of the microstructure of $(Ti_{0.81}Si_{0.19})N_{1.13}$ film on Ta substrate annealed at 1200 °C [53].

The focused ion beam (FIB) milling technique, however, has now established as an advanced tool for cross-section preparation and microscopy for a wide range of materials and composite [54, 55]. This has been due to its high precision milling and good imaging contrast, all the while imparting limited damage to the regions of interest. By using the FIB for cross-section preparation and imaging, it is possible to identify deformation mechanism of the nanocomposite coatings on ductile substrates. Nanoindentation, utilizing spherical indenters of varying radii, can be undertaken to characterize coating deformation and fracture behaviours and FIB can be used to mill through the indentations [57, 58]. The FIB may be used to rapidly prepare and image the site-specific cross-sections through coatings by sputtering, avoiding detrimental processes associated with polishing such as deformation, smearing and closing of existing cracks by mechanical abrasion [55, 58]. A typical FIB uses a liquid metal ion source to emit gallium ions in a high vacuum environment. These ions are accelerated by energy of between 5-50 keV and can be rapidly and precisely and selectively sputtered on a surface by using electrostatic lenses. After the gallium ion impact on the sample surface, the secondary

electrons/ions and atoms are ejected from the samples [55, 56]. Theses ejected secondary ions or electrons can be used for imaging the sample surface, similarly to a Scanning Electron Microscopy (SEM). First a wedge-like trench is made using high currents of gallium ion (Figure 7a) and subsequently polishing is performed with low current. Finally the cross-section is observed and images are taken by tilting the sample stage by 30 °- 45 ° at low currents (Figure 7b). Firstly, a gallium ion beam of high current (6,600 pA) is used to mill the specimen surface and create a wedge-like trench, and then the resultant rough cross-section is 'polished' at medium beam current (1,000 pA) to remove the deposition and smoothen the surface. Finally the cross-section is observed and imaged at low beam current (70 pA) with a sample tilt of 45°

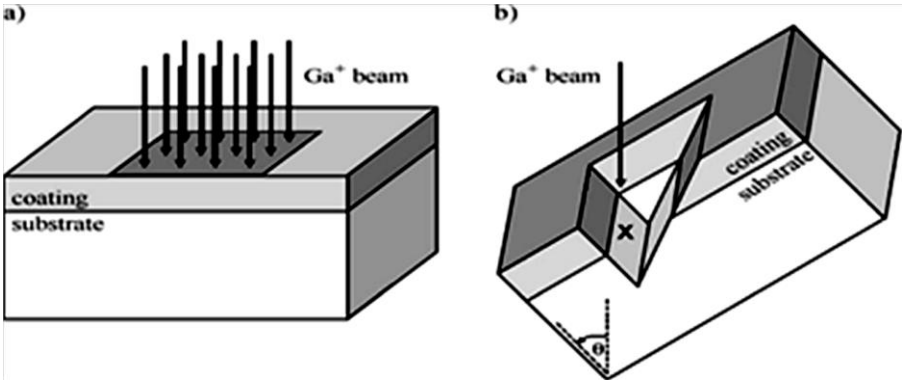

Figure 7: Preparing a cross-section using the FIB. The specimen is (a) milled using the ion beam and (b) tilted to an angle (h) so that the newly created surface (labeled x) can be imaged [54].

Transmission electron microscope integrated with FIB has been used to ascertain deformation and fracture processes both within the coatings and at the coating/substrate interface [12, 54, 59, 60]. The transmission electron microscope (TEM) is a powerful tool for the observation of thin metal films. It has been used to investigate the fine micro-structural features such as dislocations, crystalline defects, interfacial reaction, and foreign atom agglomerations, etc.

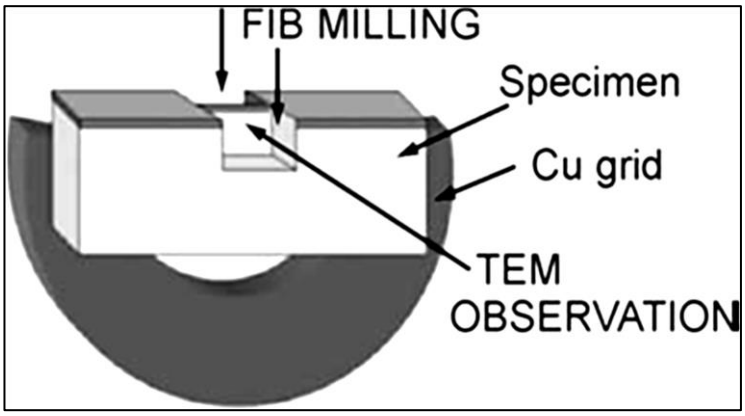

Figure 8: The above picture shows the FIB integrated with the TEM. FIB provides Ion beam for cross-sectional milling and TEM provides E-beam with high resolution for sample imaging and analysing [54].

1.5 X-Ray Diffraction of TiSiN coating

X-ray diffraction is used to measure the typical spacing's between layers or rows of atoms, size, shape and internal stress of small crystalline regions, eventually the crystalline structure and the lattice parameter with a specific wavelength of x-ray, it also helps to characterize the materials and their orientations in the thin epitaxial films. As the x-ray waves interact with the regular structure whose repeat distance is nearly same as the wavelength and gets interference between the waveform and the electronic state of the atoms and this phenomenon is known as diffraction; that denotes the coherent and elastic properties of scattering. This diffraction pattern consists of different reflections intensity of light to be used to detect the structure of the crystals. And the reflection maxima in the diffraction pattern represent the Bragg peaks. Actually this method is based upon Bragg's diffraction law mathematically explained as

$$\boldsymbol{2d\ sin\theta\ =\ n\lambda} \qquad (4)$$

where θ = ½(2θ), and d is the spacing between the lattice planes which is perpendicular the wave vector of incident and diffracted radiations [61, 62] (fig.9). With XRD, the crystallite size of TiN grains, crystal phases and internal residual stress of the TiSiN coating can be determined by the peak positioning, intensity, broadening and shifting in 2θ scale [22, 63].

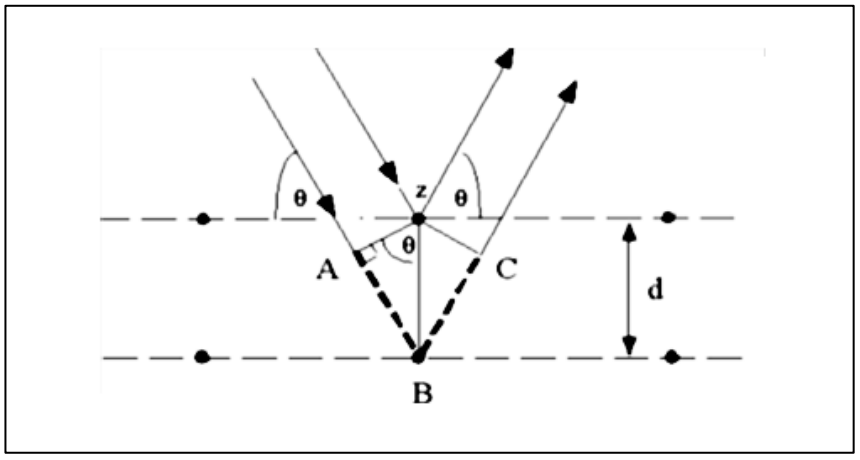

Figure 9: The Bragg's diffraction pattern showing the incident ray and diffracted ray from the corresponding crystal lattice planes [61, 62].

The TiN nanocrystals or grains in the nanocomposite TiSiN film synthesis depends on the Si addition, nitrogen partial pressure, substrate bias voltage and thermal treatment or annealing. The XRD results demonstrated that all the deposited $Ti_{1-x}Si_xN$ coatings possessed a preferred

orientation of (111), (200) and (200) peaks similar to NaCl B1structure and it is broadened with increasing Si content and the peak broadening suggests the decrease of TiN crystallite size in the deposited coatings as shown in fig. 10 [4, 27, 30 & 63].

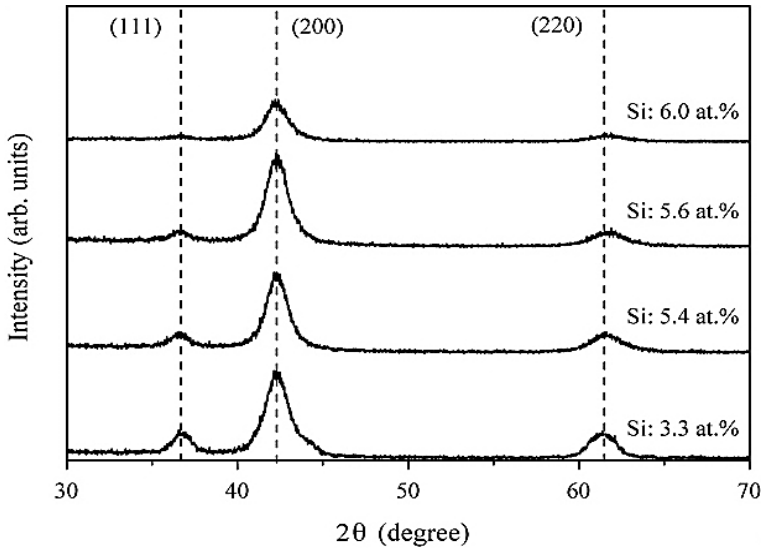

Figure 10: X-ray diffraction pattern showing the preferred peak (200) with broadened intensity of TiN crystals. The peak broadening responses to increased content of Si percentage in TiSiN nanocomposite film [63].

For the effect of increased nitrogen partial pressure, the average grain size of TiSiN film decrease from 12 nm to 8 nm. This can be attributed to the broadening and the reduction of XRD peak intensity of (111), (200), (220) and (311) peaks due to crystalline refining or more amorphous phase formed [28, 46] as shown in the fig.11.

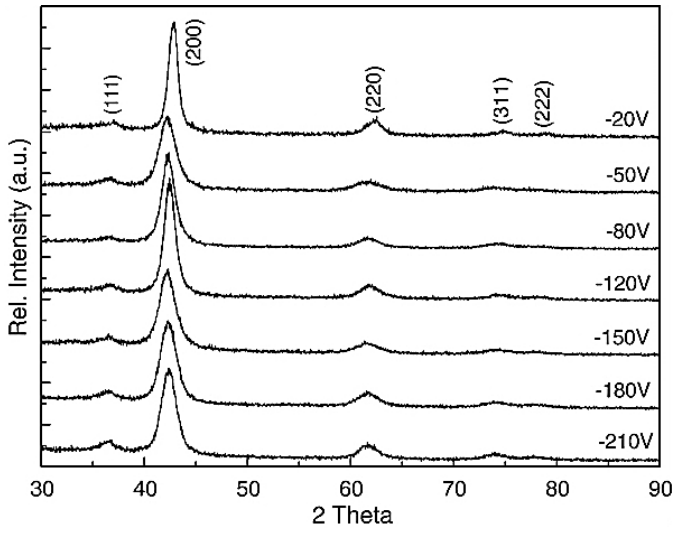

Figure11: XRD pattern of TiSiN film showing (111), (220) and (311) peak reduction and broadening with increased N_2 partial pressure in PVD process [46].

Higher energy X-ray from Synchrotron gives the deeper penetration depth as well as a narrow divergent angle. Plenty of research has been conducted by Synchrotron radiation for surface and sub-surface residual stress analysis in thin film technology [64-66]. A high intensity of Synchrotron X-rays with a narrow divergent angle enables the stress measurement in a very localized area whose dimension is less than one micrometer [65]. It is possible to conduct stress measurement with high accuracy by choosing the appropriate beam energy and wavelength from Synchrotron radiation.

1.6 TiSiN Coating composition

The composition of Ti, Si and N depend on Ti target current, Si target current and gas ratio of N_2 to Ar in magnetron sputtering process. The Ti, Si and N concentrations of the films are governed to a large extent by the reactions occurring on the target surface [26, 36, 46-48]. When the Si target current increases at fixed Ti target current, the relative Si concentration in films increases monotonically, while the reverse trend is seen for the Ti concentration (from the table1)

Table1: Relation between silicon composition and Silicon target current in magnetron sputtering technique.

Samples	Ti target current(A)	Si target current(A)	Ti at%	Si at%	N at%
Ti-Si-N(1)	5	0.5	41	3	56
Ti-Si-N(2)	5	1	37	9	54
Ti-Si-N(3)	5	1.5	28	14	58

The table shows the increased amount of Si with increasing the Si target current in the magnetron sputtering technique [26].

In other PVD processes such as cathodic are evaporation, arc ion plating and RF magnetron sputtering have other deposition parameters, which contribute to the Ti, Si and N concentration [26, 38, 68]. The flux of atoms from the targets mainly these three elements, although O_2 can also present to a minor extent. This oxygen contamination source is due to high Ti and Si reactivities with residual water in vacuum chamber during deposition and thermal annealing at higher temperature [27, 68-70]. Oxygen bond with Ti and Si as TiO_2 or SiO_2 phases may be present on the surface or in the TiN grain boundaries due to thermal annealing [24, 51, 70]. The carbon implantation on the nanocomposite TiSiN coating produces different carbon

concentration from the surface to subsurface in the nanocomposite coating [71-74]. Carbon may bond with Ti, Si, N and may produce TiC, SiC or carbonitrides (CN) or may present as graphite carbon form without any bonding.

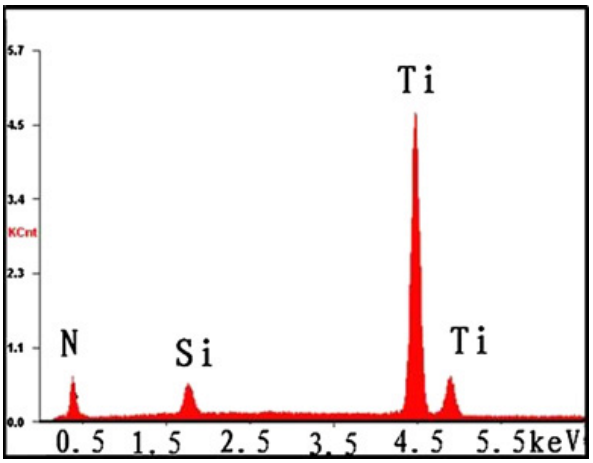

Figure12: EDX spectrum of TiSiN coatings showing N, Ti, and Si contents deposited at N2/Ar ratio of 3[75].

A number of free-standing EDX systems exist. EDX systems are most commonly found on scanning electron microscopes (SEM-EDX) and electron microprobes. Scanning electron microscopes are equipped with a cathode and magnetic lenses to create and focus a beam of electrons, and since the 1960s they have been equipped with elemental analysis capabilities. A detector is used to convert X-ray energy into voltage signals; this information is sent to a pulse processor, which measures the signals and passes them onto an analyzer for data display and analysis. The application of EDX has also been conducted for nanocomposite TiSiN thin coatings chemical characterization as shown in fig.12 [28, 75, 76, 77].

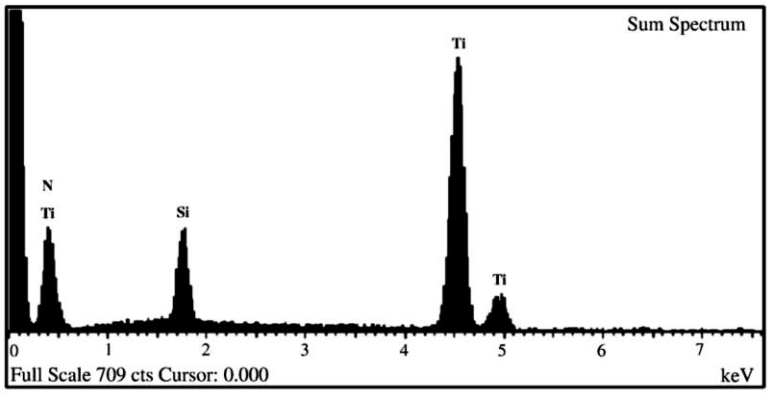

Figure13. EDX composition analyses of wear track against a WC-Co ball after sliding test in TiSiN coating [76]

The EDX spectrum in the figure 13 shows the Ti, Si and N spectrum peaks detected according to the X-ray collision with the elements in the TiSiN nanocomposite thin coating surface [76].

XPS analysis has specially been conducted for elemental analysis of surface and subsurface distribution [24, 26, 31, 38]. By XPS for TiSiN (Fig.14) with a silicon content of more than 10 at.%, Ti2p reveals the presence of two peaks at around ~455 ev for TiN and ~458 ev for Ti-O phase respectively; N 1s spectrum reveals the presence of two peaks characteristic of nitrogen in TiN and Si_3N_4 with binding energies at around ~397.0 and ~399eV, respectively. The intensity of the two peaks indicated that most of the nitrogen present in the TiN/Si_3N_4 nanocomposite coating is in the form of TiN with relatively small amounts of Si_3N_4. The Si2p spectrum gives a characteristic peak at a binding energy of ~108.0 eV corresponding to the Si 2p electrons in Si_3N_4. Peaks pertaining to free silicon (99.0 eV) and other silicon compounds were not observed, indicating that the bonding state of silicon was in the form of Si_3N_4 as shown in fig.14[24, 27, 78, 79, 80].

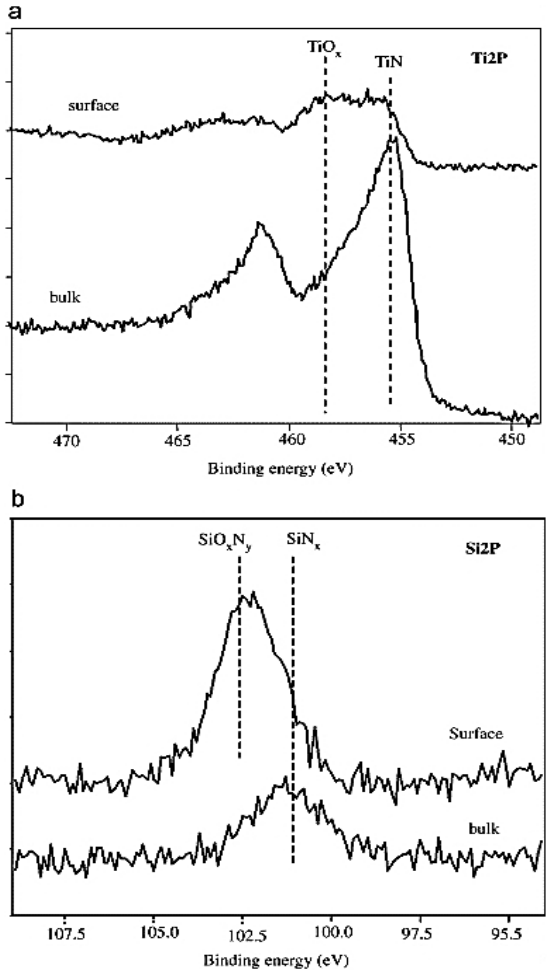

Figure14: XPS spectra recorded around Ti2p (a) and Si2p (b) lines at two different sputtering times for 4 x 5 nm TiSiN film [78].

1.7 Nanocomposite TiSiN coating deformation mechanism

Ceramic materials, with their higher lattice resistance, deform differently from metals and alloys at the nanometer scale. Nanocomposites deform in a quasi-plastic manner via cracking at the nanocrystalline grain boundaries [12] .At a critical applied stress, when the density of these nanocracks becomes sufficiently high, the cracks join up. The larger crack size leads to an increase in the stress intensity factor, causing further coalescence resulting in crack propagation along the grain boundaries [54, 81]. Nanocomposite coatings do not deform by conventional plastic deformation processes associated with shear, but rather by the formation of grain-sized intergranular cracks under local tension [12, 44]. Samples with low silicon contents (0.8 and 1.5 at.% Si) has a columnar grain structure which deforms by intergranular cracking and shear sliding at the grain boundaries, while samples with higher silicon contents (9.5 and 12.5 at.% Si) consisted of TiN nanocrystals ~5 nm in size connected by an amorphous Si_3N_4 matrix. The indented nanocomposite coatings contained a limited amount of intergranular cracking, and are thought to deform in a pseudo-plastic manner via nanocracking at the grain boundaries. At high enough applied loads, these nanocracks coalesce and propagate as intergranular cracks.

Two distinct layers at the substrate/coating interface are found by Cairney for the specimen containing 9.5 at.% Si. These two layers are thought to be (i) metallic Ti adjacent to the silicon substrate deposited in the initial stages, followed by (ii) TiN between the Ti interlayer and the TiN/SiN coating, which is deposited for a brief period after the N gas is introduced to the chamber, but before the Si magnetron source is turned on[12]. Extensive shear bands are observed in the deformation region along with an amorphous region directly below the indent of TiSiN coating with different silicon content. In some cases, crystalline phases are seen within the amorphous region. The deformation mechanisms in nanoindented Si are dominated by complex phase transformation processes where diamond cubic Si undergoes slip, but also transforms to a metallic Si phase on loading. On unloading, the metallic Si transforms to either amorphous Si, or a crystalline Si- phase depending on the unloading rate. Radial cracks form in the coating near the interface with the substrate but do not penetrate into the substrate and some radial cracks in different Si content coating grow completely through the coating and into the substrate. These cracks are thought to have occurred, due to the high level of residual stress in the films. In the case of the steel substrate, the deformation zone appears to contain many small, nanometer-sized grains which may be the result of recrystallisation which takes place due to the high levels of shear deformation under the indenter. In the figure 15, deformation occurs via cracking and shear sliding along the boundaries between the columnar

TiN grains of coating contained 0.8 at.% Si. The cracks are stopped at the base of the coating by the ductile layer of metallic Ti. As the load is increased, the cracks widen at the base of the coating as both the ductile steel substrate and interfacial Ti layer undergo plastic deformation.

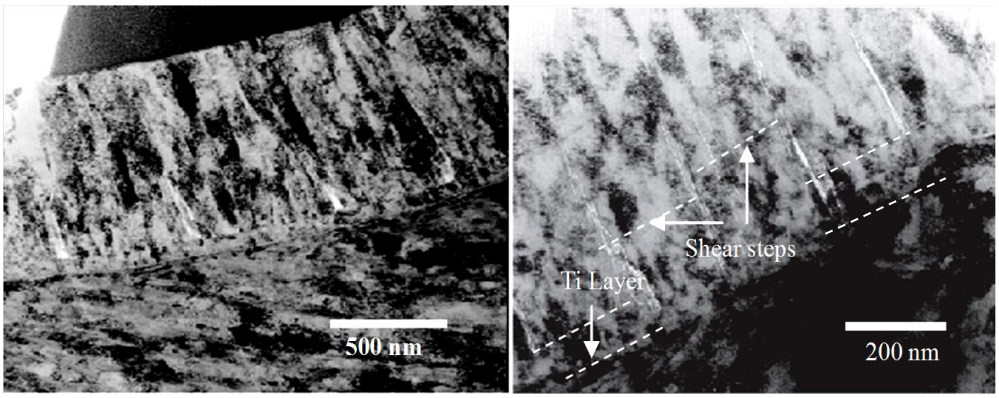

(a) (b)

Figure 15: The TEM image of the TiSiN coating containing 0.8% Si indented with a load of 400 mN. The right one is taken from the centre of the indent and the left one is taken from the edge of the indented area. Columnar grain sliding make the shear steps in the coating [12].

Fine intergranular cracks with a large amount of crack branching can be found in TiSiN film contained 12.5 at% Si, following a tortuous path along the boundaries between the TiN nanocrystals (fig.16).

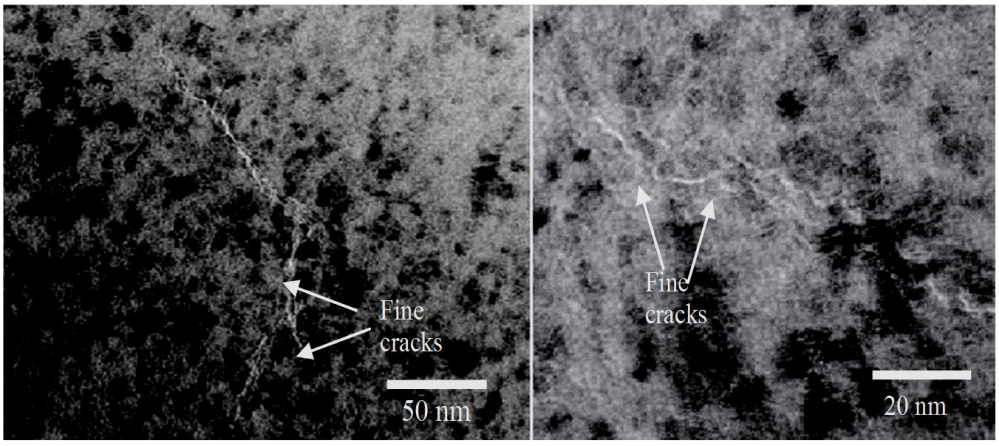

(a) (b)

Figure 16: The TEM image of the TiSiN coating containing 12.5% Si indented with a load of 400 mN. The right one is the higher magnified image of the left one. Fine intergranular cracks with a tortuous path along the boundaries between the nanocrystals with a large amount of crack branching can be observed [12].

No evidence of true plastic deformation was observed in the microstructures examined in the previous research. No debris from dislocation motion was observed nor were any of the

signs of plasticity, such as deformation twinning, elongation of grains and voids formation at grain boundaries and triple junctions, observed in the TiSiN nanocrystalline deformed coatings.

1.8 Mechanical properties of TiSiN caoting

Mechanical properties of nanocomposite coatings are well characterized by their hardness, H, Young' modulus $E^* = E / (1- \upsilon^2)$ and elastic recovery W_e. Thee quantities can be evaluated from loading/unloading curves measured by a dynamic microhardness tester. Measured values of H and E^* permit to calculate the ratio H^3/E^{*2}, which gives and information on a resistance of the material to plastic deformation. The likelihood of plastic deformation is reduced in materials with high hardness H and low modulus E^*. In general, a low modulus is desirable as it allows the given load to be distributed over a wide area [5, 16].

Hardness usually implies resistance to deformation and, for metals, resistance to plastic deformation. Thin film coatings for tool materials have to be hard in order to function as a tool without suffering undue deformation, but they also have to be sufficiently tough to withstand bending loads imposed by cutting forces, and to sustain shocks generated by interrupted cuts at high speeds and feed rates. Therefore, hard protective coatings, such as TiSiN-based materials, are becoming more and more important to prolong the service life [46- 49]. It is not an intrinsic property of a material, but rather depends on a number of properties including the elastic modulus, yield strength and strain hardening behaviour [5, 11]. Also, hardness is related to wear resistance since high hardness is beneficial in resisting abrasive wear. Veprek suggested that nano-composite nc-TiN/a-Si_3N_4 coatings by CVD or PVD has high hardness (>50 GPa) and very high elastic modulus [11] and fracture toughness at temperature of 1000 °C which is used suitably for dry and hard machining[8]. Hardness and elastic modulus testing by nanoindentation are the most commonly used techniques for characterization of the mechanical properties of materials in thin film form, including nanocomposite TiSiN coatings [46, 49, 53, 82]. Nano-/micro-indentations are regarded as good methods in hardness determination of thin films and coatings.

Indentation into the specimen surface provides information related to the resistance to deformation of the thin film. The indenter is brought into contact with the specimen and if sufficient force is applied, this may cause permanent deformation of both the coating and/or the substrate. The resulting force-displacement data allows not only hardness to be determined, but also, properties such as elastic modulus and fracture toughness. Therefore, indentation methods are finding increasing use in the study of mechanical properties of thin film materials over a wide range of size scales. In the case of micro-hardness indentation, the forces involved are usually in the range from 0.1N to 5N and the depth of penetration is measured in a range from a

few μms to ten's of μms in size. The area of contact is calculated from direct measurements of the dimensions of the residual impression left in the specimen surface upon the removal of load. However, the thickness of typical TiSiN ceramic coatings used rarely exceeds a few μms and is often much less [2-4]. Therefore, the forces required to press the indenter into such a surface without significant substrate deformation must be well below those normally used in conventional micro-hardness testers. These requirements have led to the development of a relatively new technique for measuring hardness, known as nanoindentation [5, 6, 83, 84].

The hardness and Young's modulus values of Ti–Si–N films have been found by nanoindentation up to 34 GPa and 275 GPa, respectively, with 15.6 at.% Si contents [82]. Kim found that the incorporation of small amount of Si (7.6 at.%) to TiN enhanced the hardness up to about 30 GPa measured by nanoindentation. As the Si content increased, the hardness of Ti–Si–N coating layer largely increased, reached a maximum of approximately 38 GPa at Si content of 11 at.% [85]. Jiang found that the hardness and elastic modulus of the films increase with increasing Si content, and reach a maximum for a film at 9 at.% Si (hardness = 35 GPa and elastic modulus = 383.2 GPa). With further increase in Si content, both hardness and elastic modulus values decrease gradually [26]. The hardness increases with Si concentration, reaching a maximum value of 37 GPa in a range of 5–8 at.% Si, and then decreases to 22 GPa at 22.5 at.% Si. Young's modulus also reaches to a maximum value of 360 GPa at approximately 3 at.% of Si [37].

1.8.1 Mechanical properties of post treatment carbon implantation

In order to improve the fracture toughness of TiSiN coating, ductile Ti or TiN buffer layers are incorporated into the middle of superhard nanocomposite coatings to form a multilayer structure [59, 86, 87]. The number and thickness of Ti or TiN buffer layers are varied in order to obtain the optimal configuration. The toughening mechanisms of the coating may be related to the crack deflection, ductile interlayer ligament bridging, and crack tip blunting. By post implantations of hard coatings, improved surface hardness and wear performance can be expected, without damaging the in-depth layers [54, 59, 87, 88]. For instance, carbon implantations result in increased hardness values and low friction coefficient (~0.2) [73, 89-92]. In addition, the implantation may also reduce the residual stress level in the coatings by the self-annealing effect [93-97]. The oxidation and corrosion resistant behaviour of TiSiN film makes it important in surface engineering application [101-103]. Xu reported that the indentation results revealed that hardness enhancement (~10%) was only found on sample (S-2)1×10^{17} atoms/cm^2. The hardness of (S-1) 5×10^{16} atoms/cm^2 (30.3 GPa) remained almost the same as without implantation (S-0 ~30.6 GPa). The hardness of sample S-2 increased to 33.5 GPa, whereas the

hardness of samples S-3(5×10^{17} atoms/cm^2) and S-4 (1×10^{18} atoms/cm^2) dropped to ~13 GPa. The presence of new phases can give increase the coating hardness compared with titanium nitrides. Thus, the formation of carbide bonds (e.g. Ti–C or Ti–C–N) as assumed from the XPS and XRD may be responsible for the increase of hardness recorded for the samples implanted with lower implantation doses. On the contrary, the reduction of hardness with higher implantation doses is mainly attributed to the substantial amount of amorphous or graphitic carbon formed on the coating surface [71]. The nano-hardness data of other research shows an increase in hardness (35.17 GPa) with carbon implantation, albeit with a lower hardness (33.65 GPa) at a higher carbon doses. The lower hardness is attributed to the presence of a thicker carbonaceous surface layer at higher dose [92].

1.8.2 Mechanical properties of thermal annealed TiSiN coating

The vacuum post annealing (up to 900 ^{o}C) can promote the fracture toughness and adhesion strength of the coating [69, 78]. The TiSiN film was annealed in many researches for improving the toughness and oxidation resistance for using in cutting, drilling or many thermal surfacing environments [22, 24, 41, 42, 103, 104] In the study of Barchila, the Raman data showed that the nanocomposite TiSiN coatings started to oxidize at 800 °C as compared to TiN, which have been oxidized even at 500 °C. To isolate the oxidation induced spectral changes as a result of heating of the coatings in air, the samples were also annealed in vacuum at 850 °C under similar conditions. The Raman data of the vacuum-annealed coatings showed no phase transformation even after annealing up to 850 °C [24]. Mannling found no hardness decrease for TiN–Si_3N_4 nanocomposite coatings up to an annealing temperature of 800 °C [41]. Flink found the films with Si content 0.04~0.09 retain the hardness at 30.2 ~38.8 GPa after annealing up to 1000°C [53].

1.9 Residual stress of TiSiN nanocomposite coatings

One important property of thin films, which has been studied extensively in recent years, is their stress state. Advances in thin film technology therefore have been accompanied by efforts to measure the stress and even to control the stress in thin films [105]. The residual stress plays an important part in any coating for adhesion and bonding with substrate and also influences fracture toughness by hindering crack propagation [106, 107]. The amount of residual stress increases with increasing in film thickness [107]**.** Further, the performance of a film system is influenced by the residual stress present in the film, especially the strength, hardness and wear resistance [108]**.** Liu reported that the residual stress present in TiSiN films

depends on the Si addition in the film [109]**.** Nose observed that the residual stresses have their maximum compressive stress (bottom means the maximum compressive stress in the fig. 17) at approximately 8 at % Si [37].

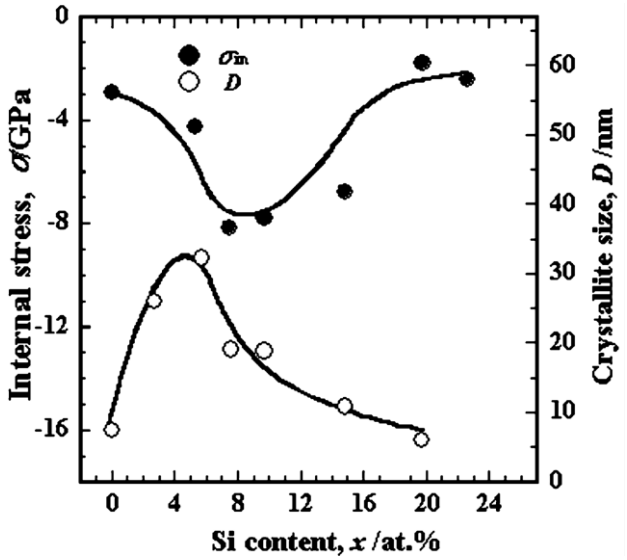

Figure17: Internal stress and crystallite size of Ti–Si–N films deposited without bias application nor substrate heating as a function of the Si content [37].

Bendavid observed that the residual stress values over the entire range of silicon content in the film were 4.5 to 7.0 GPa. The variation in the grain size and composition may be responsible for changes in the magnitude of the stress. The stress data does not follow the same trend as the hardness with the change of silicon content, which implies that the high hardness of the as-deposited films is not an artefact due to high compressive stress but a consequence of a nanocomposite structure (fig.18) [43].

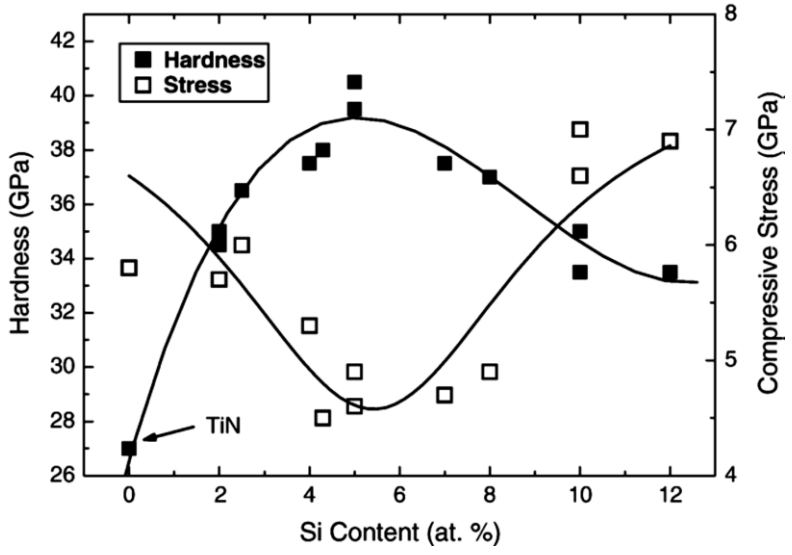

Figure 18: Dependence of the measured hardness and compressive stress of the Ti–Si–N films on the silicon content in the films [43].

For the substrate bias voltage from -20 to -50 V, compressive stress clearly dominates in the coatings reaching a maximum of approximately 1.6 GPa at -40 V. This high compressive stress was attributed to ion bombardment (atomic peening effect) taking place at relatively low deposition pressures of 0.09 Pa. Since intrinsic stresses are the consequence of relatively low deposition temperatures, heat treatment at higher temperatures should result in significantly lowered residual stress levels [110]. Chang found that as bias voltage increased, decreasing grain size with the increasing residual stress can be attributed to the effect of Si atoms being added in the TiN structure [46].

In general, the residual stress in a PVD coating consists of two main components: thermal (termed extrinsic) and intrinsic [110]. Thermally-induced stresses will be generated during the coating-substrate system's cool down from the deposition temperature to room temperature after deposition. The coefficients of thermal expansion ($\Delta\alpha$) of the film and its substrate are not the same, and a change of temperature (ΔT) occurs during deposition. Cooling will produce thermal stresses between the film and its substrate, which may deform the film/substrate. Intrinsic stress is generated in the coating by the structural mismatch between the substrate and the coating and/or by growth defects caused by ion bombardment during deposition [110]**.** It is well known that the intrinsic stress, tensile or compressive depending on the deposition conditions, can be generated during the growth of sputter-deposited thin films [109]. It can be seen that control of residual stress is very important in coating technology.

X-ray diffraction or $Sin^2\psi$ method has been used for evaluating the deposition residual stress by using the glancing incident angle [64, 111, 112]. The principle of the $sin^2\psi$ method can be briefly summarized. The interreticular distance is taken as a strain gauge. Varying the ψ angle of measurement between the normal to the surface and the normal to the (hkl) diffracting planes enables to measure the strain in different grain orientation for the same <hkl> direction and thus to follow the shift of the diffraction peak position due to in plane macro stresses. The stress is then estimated applying the linear elasticity formalism which rely the measured strain to the stress through the elastic constant tensor of the material. Assuming an isotropic biaxial stress state and using the rational formalism to express the strain, the $sin^2\psi$ relation is given by [64]:

$$\boldsymbol{ln(a_d) = [(1 + \nu) / E]\sigma sin^2\psi - (2\nu / E)\sigma + ln(a_0)} \qquad (5)$$

where a_0 is the stress free lattice parameter, a_d the strained lattice parameter, σ the in plane residual stress. E and ν are the Young modulus and Poisson's ratio, respectively. When plotting $ln(a_d) = f(sin^2\psi)$ curves, a linear behaviour is expected and the macro stress is then deduced from the slope and the stress free lattice parameter from the ordinate origin.

The Synchrotron X-ray procedure is very effective as synchrotron radiation analysis which provides the X-rays with extremely high intensity as well as a narrow divergent angle. The high energy X-ray provides stress information from the surface and sub-surface region [64-66, 113, 114]. The stresses in thin film can be measured by the following equation [113,114]:

$$\sigma = -(E/1+\nu)[\varepsilon(\psi_2)-\varepsilon(\psi_1)/\sin^2\psi_2-\sin^2\psi_1] \quad (6)$$

where E and ν are Young's modulus and Poisson's ratio of the film, respectively, and ψ is the angle between the normal to the lattice plane and the normal to the film surface. Expressing the lattice strain ε in terms of the diffraction peak angle 2θ, the above equation becomes

$$\sigma = -[E/2(1+\nu)]\pi/180\cot(\theta_0)[2\theta(\psi_2)-2\theta(\psi_1)/\sin^2\psi_2-\sin^2\psi_1] \quad (7)$$

$$= K.M$$

where K is the stress constant, and M is the slope of the 2θ vs $\sin^2\psi$ diagram.

Nanoindentation techniques have been used for intrinsic residual stress measurement of ceramic and nanocomposite thin film. This technique uses load-displacement information by spherical indenter, yield strength and modulus of the thin films [115, 116]. In this method Swadener proposed the formula for measuring the residual stress by the nanoindentation through:

$$\sigma^R = \sigma_y(1 - 1.26/\pi \left[\frac{E_a a_0}{\sigma_y R}\right]) \quad (8)$$

here σ_y is the yield stress of the ceramic coating, E_a is the effective elastic modulus of the coating, R is the indenter radius, a_0 is the contact radius of spherical indenter calculated from-

$$a_0 = (2Rh_c - h_c^2)^{1/2} \quad (9)$$

and h_c is the contact depth calculated from-

$$h_c = \tfrac{1}{2}(h_{max} + h_f) \quad (10)$$

where h_{max} is the maximum indentation depth at maximum load and h_f is the final depth of contact after unloading at loading-unloading curve.

1.10 Nanocomposite TiSiN coating wear resistance properties

The wear mechanisms of hard coatings have been categorized as oxidation, abrasion, cracking, spalling, adhesion and cohesion etc. The wear behaviours of deposited coatings are a combined function of friction coefficient, counter materials and film adhesion strength [46, 48]. Wear is generally a physical (rather than chemical) form of materials degradation. It is a complex surface phenomenon that occurs mainly due to sliding and impact of hard particles against solid surfaces, even in the presence of self lubricants by chemical reaction [46, 48]. Therefore, wear resistant surface coatings play an important role as they improve the life of tools, dies and machine components. In TiSiN, it was observed if the concentration of Si_3N_4 increased; the improvement of the wear resistance was very high. This improvement in the wear resistance could be due to lower friction coefficient of Si_3N_4 and increased hardness of the nanocomposite TiN/ Si_3N_4 [24, 32-35, 46]. Guo observed that the coating layer had a maximum hardness of 42 GPa at a DC substrate bias of -150 V. TiSiN thin films coated on tungsten cemented carbide tools had excellent adhesion, and the critical load exceeded 150 N as shown in fig.19 [49].

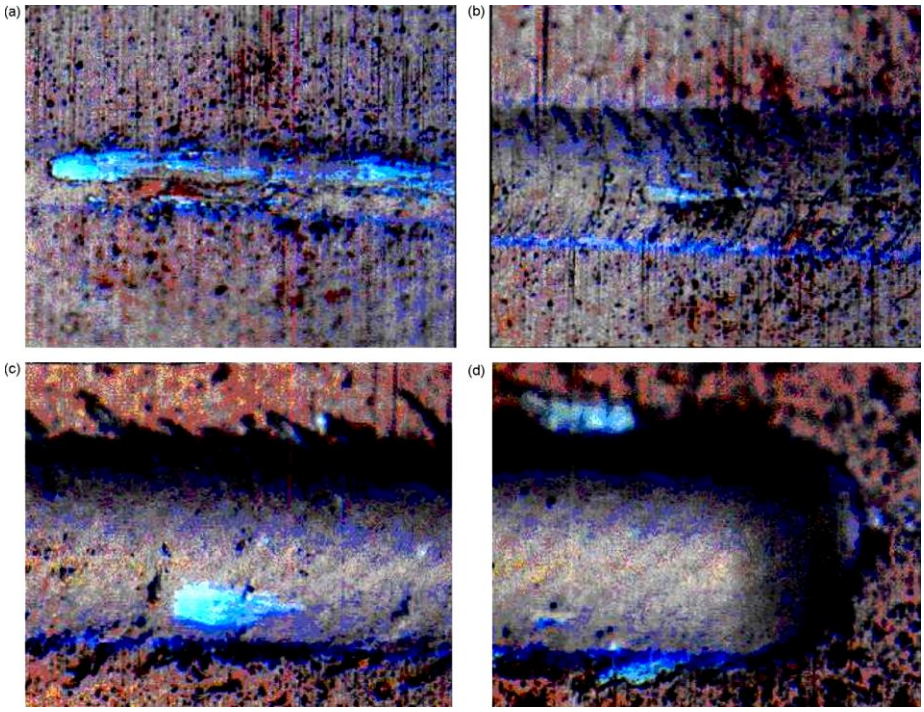

Figure 19: Micrographs of failure events used in scratch testing of TiSiN coatings at a DC substrate bias of 150 V, (a) LC1(18 N), (b) LC2(62 N), (c) LC3(136 N) and (d) LC4(157 N)[49].

Cheng found that the tribological behaviours of the TiSiN coatings are strongly dependent on the Si content of the coatings and the ball material as shown in fig.20 [48].

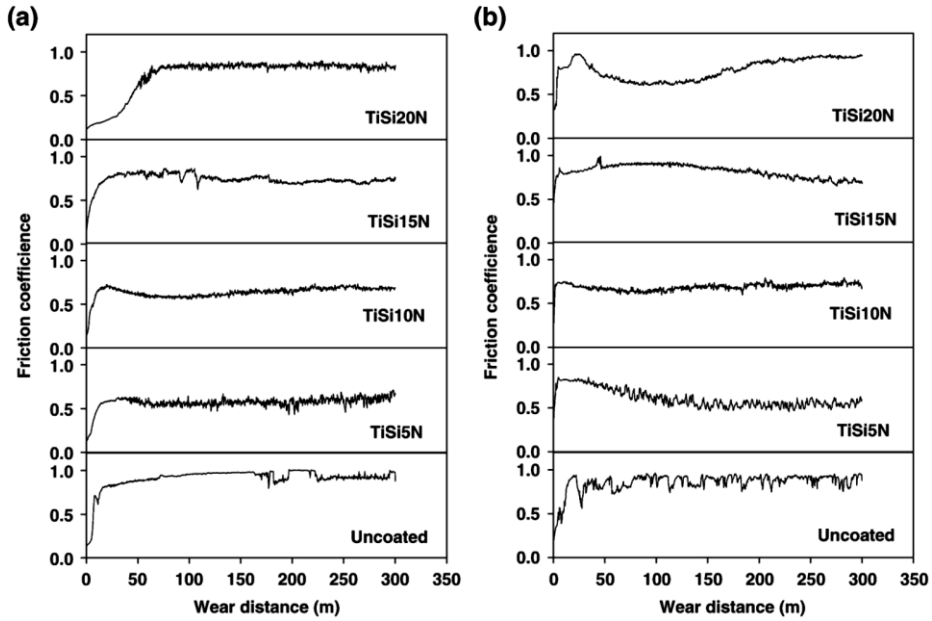

Figure 20: Typical surface profiles of the wear track on the uncoated and TiSi5N, TiSi10N, TiSi15N, and TiSi20N coatings coated 440A stainless steel coupons tested against (a) Al_2O_3 and (b) 302 stainless steel balls [48].

Nanoscratch tests were performed to obtain the frictional properties; and the scratch tracks were observed by FIB-SEM for getting insight of the wear damage mechanism (Fig.21) [57, 117].

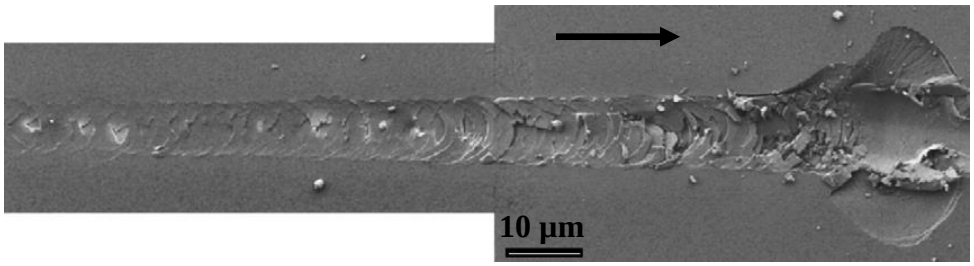

Figure 21: FIB image taken from top of scratch track, showing ring crack formation. Arrow indicates the sliding direction of the indenter. Indenter tip radius: 5mm [87].

Scratch testing was carried out using a conical indenter of 5µm tip radius (R) over a load range of 0–300 mN at a loading speed of 5 mN/s and sliding speed of 5 m/s. Following scratch testing, the width of the scratch tracks WS was measured under field emission scanning electron microscopy and plotted against normal loads PN [87, 117].

1.11 TiSiN Coating Adhesion with substrate

The adhesion of the coating to the substrate is an important property in a thin film-substrate composite. The stress required to remove a coating from the substrate is taken as a measure of adhesive strength. If the adhesion strength is inadequate, premature failure of the coated part occurs due to coating detachment [20]. Good adhesion between the coating and the substrate is required for use in practical applications. The adhesion strength of a coating depends on the extent of both chemical and physical interactions between the coating and substrate materials and the microstructure of the interfacial region. Accordingly, the interface plays a very important role in determining the adhesive strength of coatings. Zhang reported that Poor adhesion may be attributed to a low degree of chemical bonding, poor interfacial contact, low fracture toughness and high internal stresses [6]. In Zhang's study about TiSiN adhesion, it can be seen that the adhesion strength decreases with increasing the Si content in the coatings. For the coatings with Si content no more than 8.6 at.%, the rank of adhesion strength is in the range from HF1 to HF3, which reflects good adhesion strength quality of these coatings onto the HSS substrates, whereas the HF5 and HF6 adhesion quality of the Ti–Si–N coating with Si content of 12.0 at.% and Si_3N_4 coating, respectively, indicate poor adhesion quality onto the HSS substrates shown in fig.22 [27]. After 150 kgf load indentation, it will be observed using SEM to evaluate the adhesion strength. The damage to the coating will be compared with a classified adhesion strength quality figure HF1-HF6 [118], where HF1 means the best without any spallation activities and HF6 means the worst with large spallation of the coating.

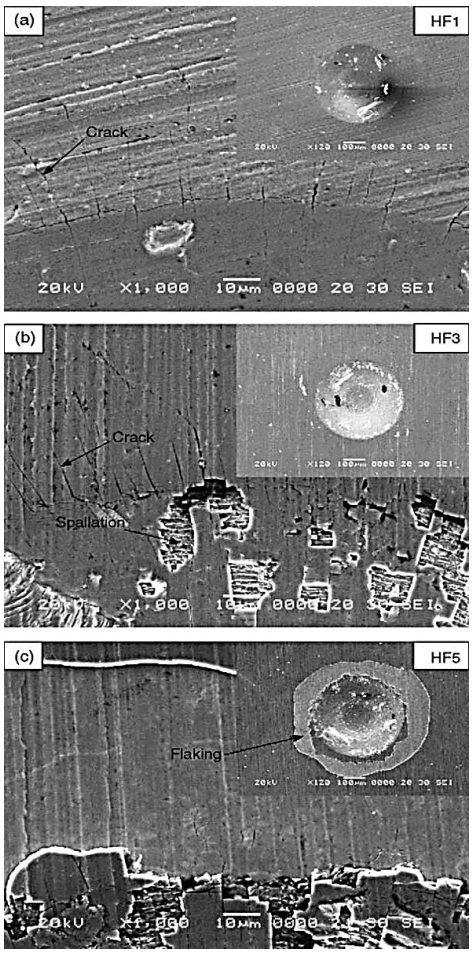

Figurer 22: SEM images of indentations on (a) the TiN coating and the Ti–Si–N coatings with Si content of (b) 8.6 at.%, and (c) 12.0 at.% after the Rockwell-C adhesion tests [27].

1.12 Corrosion behaviour of the coating

All type of coatings applied to substrate materials are multifunctional, providing corrosion control, an aesthetic surface appearance, abrasion and impact resistance. Nanocomposite coating may protect substrate by barrier protection [7, 45]. Barrier protection is achieved when coatings completely isolate the substrate from the environment. A promising coating was TiN because of his high hardness and chemically stable and pleasing gold appearance [120-122]. But when more rigorous use environment is considered, the conventional TiN coatings show the insufficiencies, especially in corrosion resistance. Therefore, incorporation of Si into TiN has achieved the improved performance in corrosion resistance [45, 100]. It has been found that the addition of silicon in TiN coating provide TiSiN nanocomposite structure with features of dense nanocrystalline and amorphous structure and lower porosities or pinholes [100, 102, 123]. The Macroscopic defect (porosities) and the columnar grains of TiN mostly contribute to corrosion in the TiN coating [124-126]. The columnar structure leads to

straight grain boundaries and open (through coating) porosity which provides efficient diffusion channels for the corrosive electrolyte penetrate down to the substrate [121, 122, 125-138]. With the Si addition, the TiSiN coating layer structure becomes denser over the TiN interlayer between the main coating and the substrate. This results in decreasing the opportunity for the through coating defects or open pore to form and in restricting the diffusion of reactive species down to the coating/steel substrate interface[123]. So, the diffusion process is slow and difficult through the TiSiN nanocomposite coating for the immiscible phases.

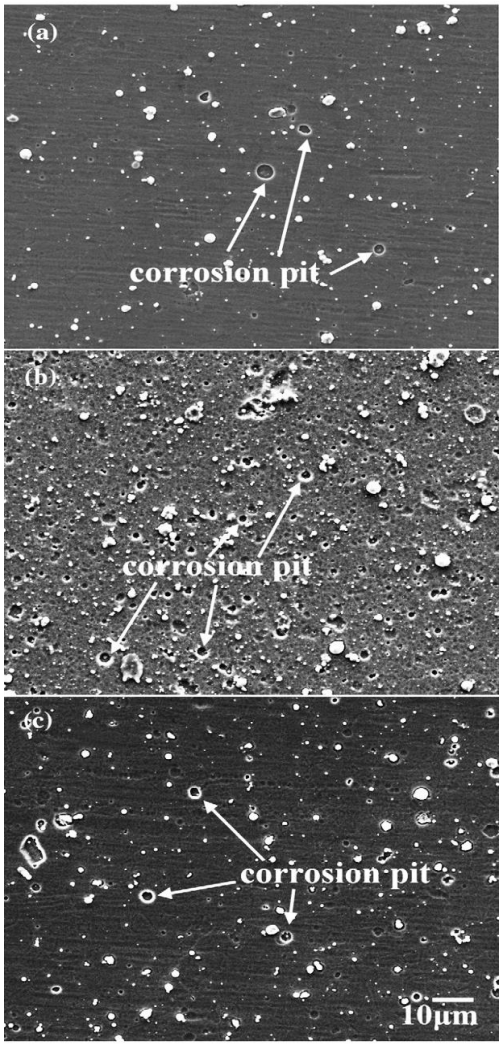

Figure 23: SEM surface morphology of (a) TiSiN, (b) TiAlN and (b) TiSiN/TiAlN multilayered coatings (S5) after corrosion testing in 1 N H_2SO_4 solution [139].

It is evident from the figure 23 shows SEM micrographs of the TiSiN, TiAlN, TiSiN/TiAlN multilayer coatings after an immersion test. Few corrosion pits were observed on the surface of the TiSiN and TiSiN/TiAlN multilayer coatings, and there were only rare of macroparticles were found which peeled off from the surface due to the corrosion tests [139]. Carbon implantation may provide Ti-C or Si-C bonding with extra barrier layer on the surface for corrosion protection [140]. The corrosion potential and corrosion current density of TiSiN showed better result than the TiN coating in the previous research.

1.13 Carbon ion implantation deposition process on nanocomposite Ti-Si-N coatings

Among the nanocomposite coatings, TiSiN is an excellent candidate for use in high speed machining conditions duet o its high hardness (<50 GPa), thermal stability, oxidation [24, 27, 30] and corrosion resistance [45, 97]. However, the friction coefficient of the nanocomposite coatings is high (~0.4to 0.6) for dry machining, forming and biomedical tools [44, 48, 129]. Ion implantation [25, 90, 91] has been found to be an alternative and efficient method to modify surface properties without affecting the originally excellent properties (e.g. high hardness) of in-depth layers. Many studies have been carried out on the effect of the implantation of noble-gas ions (Ar+, Kr+, Xe+)[141-144], metal ions[145, 146], carbon[26, 88, 147] and nitrogen [38, 148] ions on various substrates for improving adhesion, mechanical and tribological properties in the field of mechanical manufacturing. The post-treatment of carbon ion implantation has been shown to be of great interest recently for improving the tribological behaviour of hard ceramic coatings with reduced residual stress [93], yielding increased wear resistance and life time of the tools[89, 96]. The application of carbon implantation may modify the structure and chemistry of the surface layer of the ceramic coatings to impart self-lubricating ability to them. The metal vacuum arc ion source (MEVVA) (fig. 24) is one kind of advanced ion source to produce high current, multiply charged and metallic ion beams with a large area. This kind of source can provide ions of nearly all the metal elements in the periodic table, with a pulsed beam current of over one ampere for most heavy metallic ions [149, 150].

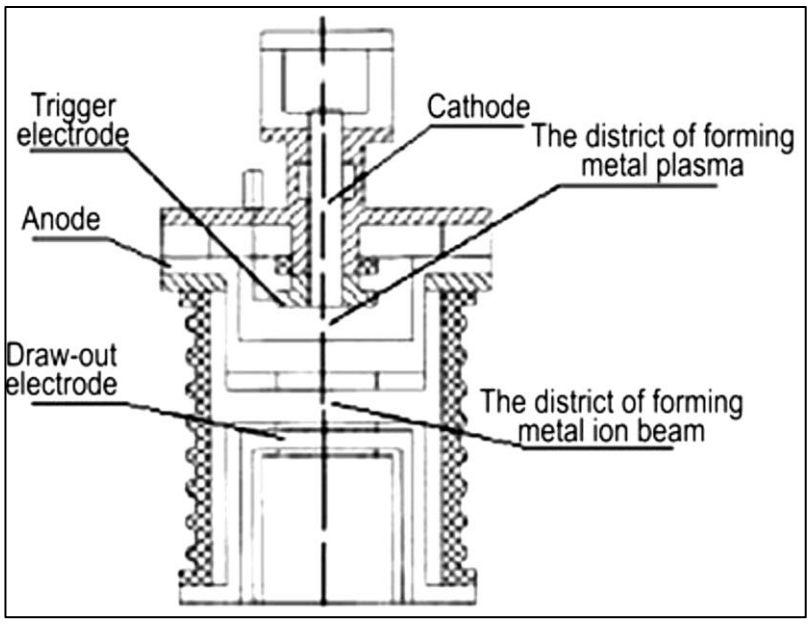

Figure 24: Schematic diagram of MEVVA ion source [150].

MEVVA ion implanter differs from the 'conventional' type of ion implanter in the fact that it uses an arc to evaporate metal and the metal vapour is then ionised. This method has a high throughput of non-mass analysed metal ions, and therefore, it has more potential for industrial tribological applications [90]. Using the MEVVA ion source, carbon and Ti ions have been implanted on TiN, TiAlN and TiAlSiN coatings deposited by physical vapour deposition [25, 88, 91, 145] for improving their mechanical and tribological properties. Pure carbon coatings, owing to their excellent mechanical and tribological properties, smooth surface, chemical inertness, and good biocompatibility, are good candidates for various biomedical applications, especially for the articulating surface of implants. The process of carbon ion implantation on substrate materials, before the deposition of coatings, has been demonstrated to be an effective method to improve the adhesion strength. The highly energetic ions sputter-cleans the substrate materials, get implanted onto the substrate materials as a composition gradient layer, and serves as nucleation sites for subsequent deposition [94, 147]. A threshold was found, up to which the implantation improved all wear characteristics of the coating, resulting in an improved lifetime to spallation. For carbon, there is believed to be a mechanism whereby implanted carbon ions diffuse from their Gaussian-type distribution towards the surface, where a thin carbonaceous overlayer forms [90]. The implantation depth, chemical composition, microstructure and nanohardness depended strongly on the implanted carbon doses [91].

1.14 Finite Element Modelling

Finite element modelling (FEM) was used to analyse stress distributions within TiSiN-based multilayer coatings under moderate indentation loading, as compared to monolithic coatings, to identify stress concentrations and their influence on crack initiation within the structure[8, 151]. The results of this study are expected to deepen the understanding of the indentation stress, structural layering on the deformation and fracture behaviour of super-hard coatings [152]. In the simulation, a 2D axial symmetry model was used to reduce computational time without compromising accuracy. For all the simulations, it was assumed that the coating is perfectly adhered to the substrate and, that the contact between the coating and the indenter is frictionless. All the interfaces between different layers were assumed to be perfectly bonded. Assuming that the loading process is slow, static analysis was adopted. The indenter and the substrate were identical for all models. The indenter being used has a spherical tip with a radius of 5μm. The substrate was simulated using a rectangle of 48μm (height) × 50μm (width). Taking into account the thickness of the coatings (i.e., 2μm), the overall height of the block is 50μm. The substrate was divided into two sections as indicated in the fig. 25.

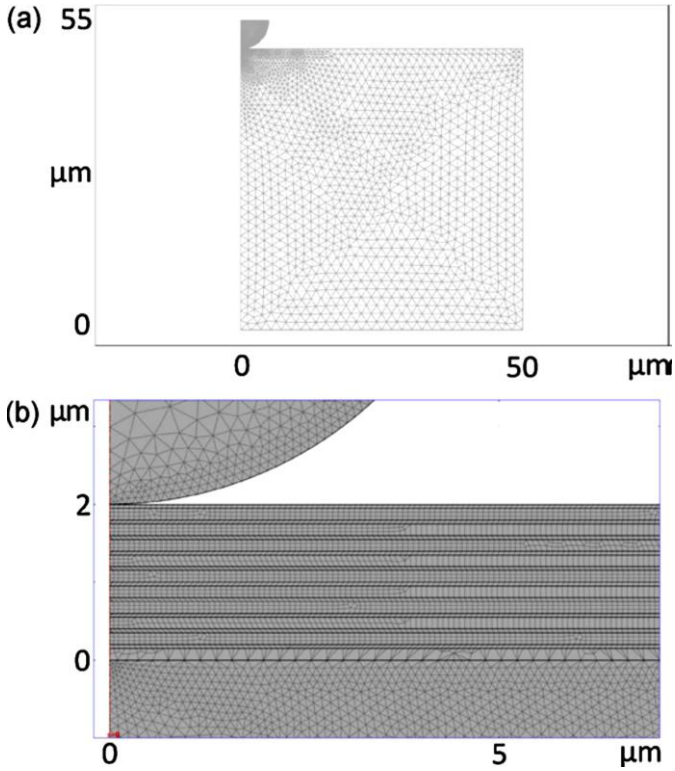

Figure 25: Model configuration used in this work. (a) Overall model layout and (b) mesh around the indentation contact in multilayer coatings [152].

The mesh within a smaller square of 10µm×10µmdirectly below the indenter was refined for accuracy (Fig. 25(b)). Details of the boundary conditions are described below. The left-hand side of the complete structure, including the indenter, coating and substrate, makes up the axial symmetry axis. The bottom and the right-hand boundaries were fixed in the z and r directions, respectively, but allowed to move in the other directions.

Due to the fact that the model dimension is considerably larger than the coating thickness, the resultant edge effect from the boundary constraints is negligible. The movement of the indenter was simulated as a downwards displacement of 200 nm. This corresponded to an indentation load less than 50 mN, under which the coatings exhibited pure elastic deformation. The deformation of the substrate was modelled in an elastic–plastic manner. Simulations in this work (Fig.26) showed that, at an indentation depth of 200 nm, within the multilayer coating the maximum radial stress, shear stress and equivalent stress are, respectively, 52%, 54% and 62% of those in the monolithic TiSiN coating [152]. The simulation results also showed that not only the maximum stresses were reduced, but also the stress distributions were modified, resulting in an overall reduction in the stress level throughout the coatings. This is particularly clear for shear stress, for which a reduction throughout the coatings can be clearly observed.

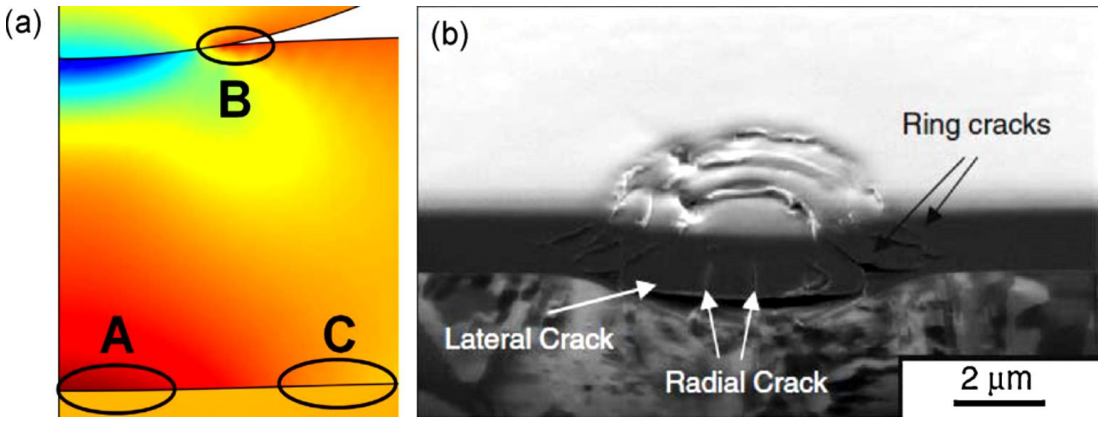

Figure 26: Correlation between stress concentrations and sites of crack initiation. (a) Simulated radial (A and B) and shear stress (C) concentration in hard coatings on ductile substrates. (b) Experimental observation of locations of radial cracks (corresponding to A in (a)), ring cracks (corresponding to B in (a)), and lateral cracks (corresponding to C in (a)) in a homogeneous diamond-like carbon coating on steel substrate [152].

1.15 Aims and motivation

With the as-deposited TiSiN coating samples, this research aims to structural, compositional and mechanical characterization of the coatings. The as-deposited coatings are thermally annealed with proper control of the mechanical properties. The changes of internal residual stress through the coatings microstructure which are inevitable during deposition are characterized after annealing and simulated by finite element modelling. The crystalline phase characterization and the compositional changes due to annealing are also characterized. The changes of damage mechanism of the nanocomposite TiSiN coatings with the change of residual stress are characterized. The corrosion morphology of the coatings is characterized by comparing between the as-deposited sample and the high temperature annealed sample in severe corrosive environment. The preferential factors that govern the mechanical and corrosion damage through the coating up to the substrate in acidic environment are simulated by the finite element analysis. The effect of mechanical damage and the stress distribution on the corrosion morphology of the coatings are characterized and computed by finite element analysis between the nanocomposite and columnar structured coatings in the same severe environment. The nanocomposite coatings are implanted with carbon ion and characterized for changing of residual stress and the tribological properties with the change of ion dosing rate.

As demonstrated by the literature TiSiN nanocomposite coating displays great potential in the coating industry as hard and tough material and great corrosion resistant application on the steel substrate. However, despite its demonstrated ability to use hard and tough coated mechanical components and perform magnificently, there still exist considerable areas in which

the full potential of TiSiN has not been exploited, one of these being is the fracture toughness measurement by nanoindentation and insitu corrosion damage characterization by FIB and XRD in bio-chemical solution. Moreover, the lack of fracture toughness measurement especially the crack deflection through the grain sliding or grain shearing is an issue to further development of TiSiN nanocomposite coatings. And also the corrosion mechanism charaterization in bio-solution opens the future research opportunity for further development of TiSiN coating system.

1.16 Research outline, methods and techniques

In the following sections, a general overview of the research framework, and the methods and techniques which have been used in this project will be presented. Whilst full details of each experiment is not supplied and can be found in succeeding chapters, this outline serves to provide a summary of the research structure and links to some of the chapters in this thesis. The discussion will be presented in order of the chapter by which they appear in the thesis.

1.16.1 Characterization of the thermally annealed and carbon implanted TiSiN nanocomposite coatings

Chapter 2 describes the Effect of thermal annealing upon residual stress and mechanical properties of nanostructured TiSiN coatings on steel substrates. Nanostructured TiSiN coatings were deposited onto a tool steel substrate. The coated samples were then annealed under vacuum at temperatures ranging from 400°C to 900°C. Both mechanical properties and residual stresses in the coatings were determined using nanoindentation methods, assisted by finite element analysis. Nanoindentation was used to determine the mechanical properties and residual stress in the treated coatings. Finite element analysis was applied to quantify the extrinsic stress in these coatings. Grazing incidence X-ray diffraction (GI-XRD) was used to characterise the microstructural factors that control the residual stress and mechanical properties of TiSiN coatings on steel. X-ray photoelectron spectroscopy (XPS) was used to probe the surface chemistry of the coatings.

Chapter 3 describes the process of controlling the damage resistance and adhesion strength of nanocomposite TiSiN coatings on steels by optimization of residual stress in the coatings. Thermal annealing is usually applied to improve the adhesion strength of nanocomposite coatings by reducing residual stress. But the effect of residual stress on the

damage resistance of these coatings remains unclear, primarily due to the difficulties associated with the subsurface observation of the contact damage in these coatings. To tackle this problem, focused ion beam (FIB) microscopy has been used to directly examine the subsurface structure of ceramic coatings on ductile substrates, enabling the identification of the mechanisms through which ceramic coatings deformed. In this work, TiSiN coatings, both as-deposited and thermally annealed, on steel substrates were prepared. FIB was used to characterise the coating microstructure. Nanoindentation was performed to measure the residual stress of the coatings. Rockwell C tests were carried out to assess their adhesion strength. FIB was also used to evaluate the damage resistance of the coatings by probing the interaction of coating microstructure with nanoindentation-induced cracks. In the end, a direct link of the residual stress with the damage resistance and adhesion of nanocomposite coatings on steels was established.

Chapter 4 describes the detailed mechanisms that govern the corrosion of the nanocomposite coated steels, following immersion tests in concentrated nitric acid solution. Pitting corrosion has been frequently observed in ceramic coatings deposited on steel substrates, originating from surface defect sites. Electron microscopy, surface X-ray diffraction (XRD) and X-ray photoelectron spectroscopic techniques have been used to probe the mechanisms under which these ceramic coated steels corroded. But a detailed understanding of initiation and propagation of corrosion in surface-treated steels is lacking and the factors that control the expansion of pitting remains unclear. Though mechanical properties of ceramic coatings are anticipated to deteriorate during corrosion, no data are available to date to substantiate such a hypothesis, making it difficult to predict the service life of ceramic coated steels in corrosive environments. Little effort has been made so far to clarify the effect of compressive residual stress on the corrosion behaviour of ceramic-coated steels. In this study, FIB, along with XRD, X-ray photoelectron spectroscopy (XPS) and nanoindentation testing, were used to characterise the microstructural evolution in both surface and subsurface after corrosion tests and determine key factors that control the corrosion process. The change of mechanical properties of the coatings under the influence of corrosion was also quantified. In addition, the effect of residual stress on the corrosion progression was clarified by finite element analysis (FEA).

Chapter 5 describes the effect of mechanical damage upon the corrosion resistance of the hard and tough nitride coated metal parts as damage is often seen in these coated metal parts during mechanical contact and little work has been done so far. Passive oxide layer was reported to form on the surface of both columnar CrN and nanocomposite TiSiN coatings previously. But the nature of the oxide layer formed on both types of coatings and its role in corrosion prevention remain unclear. Such knowledge is essential to controlling the corrosion damage of the treated metal parts and thus extending their service life. To address these challenging issues, CrN and TiSiN coatings were engineered onto steel substrates and examined. The surface

chemistry of the coatings was probed by X-ray photoelectron spectroscopy (XPS). Potentiodynamic polarisation measurements were conducted to determine the corrosion resistance. The surface morphology before and after polarisation measurements was examined by electron microscopy to allow investigation of the roles of surface oxide layers in controlling the corrosion resistance of the coatings. In addition, nanoindentation was conducted, in combination with immersion tests and subsurface observations clarifying how prior mechanical damage regulated the corrosion resistance of these coatings. Finally, finite element analysis (FEA) was also used to gain a deeper understanding of the stress distribution and damage tolerance in both coatings establishing a clear link between the structural integrity and the corrosion resistance of the coated steels.

Chapter 6 describes the effect of carbon implanation on TiSiN nanocomposite coatings in terms of structural, mechanical and tribological properties prepared by metal vapour vacuum arc process. Nowadays ion implantation has been employed to alter the near-surface structure and properties of semiconductors, metals and metal alloys without the loss of bulk properties. The changes were investigated with different carbon ion doses on coating surface. The friction coefficient of TiSiN nanostructured coating was found to be high (~0.4 to 0.6) for dry machining, forming and biomedical tools. Ion implantations have been found to be an alternative and efficient method to modify surface properties without affecting the originally excellent properties (e.g. high hardness) of in-depth layers in previous studies. Research have been carried out on the effect of the implantation of noble-gas (Ar^+, Kr^+, Xe^+), metals, carbon and nitrogen ions into various substrates for improving adhesion, mechanical and tribological properties in the field of mechanical manufacturing. The post-treatment of carbon ion implantation has been shown to be of great interest in recent time for improving the tribological behaviour of hard ceramic coatings with reduced residual stress, increased yielding strength, wear resistance and life time of the tools. However, detailed research about the effect of carbon implantation process on the nanocomposite coating is still limited. After implantation, the samples were characterized and explained by means of the cross-sectional transmission electron microscopy (TEM), X-ray diffraction (XRD), FIB/SEM, energy dispersive spectrometry (EDS), X-ray photo-electron spectroscopy (XPS), residual stress and nanoscratching measurement and also Rockwell C adhesion strength measurement etc. This chapter will provide the idea of designing and fabricating the effective and unique cutting, forming and drilling tools with lower friction and perfect mechanical properties.

1.17 References

1. Zhang, S., Sun, D., Fu, Y., Du, H., Toughening of hard nanostructural thin films: a critical review. Surface & Coatings Technology, 198 (2005) 2-8.
2. Musil, J., Vlcek, J., Magnetron sputtering of hard nanocomposite coatings and their properties. Surface & Coatings Technology, 142-144 (2001) 557-566.
3. Musil, J., Hard nanocomposite films prepared by reactive magnetron sputtering, in Nanostructured Thin Films and Nanodispersion Strengthened Coatings, A.A. Voevodin, et al., Editors. (2004) Springer: Dordrecht. 43-56.
4. Musil, J., Hard and superhard nanocomposite coatings, Surface & Coatings Technology, 125 (2000) 322-330.
5. Musil, J., Kunc, F., Zeman, H., Polakova, H., Relationships between hardness, Young's modulus and elastic recovery in hard nanocomposite coatings, Surface & Coatings Technology, 154 (2002) 304-313.
6. Zhang, S., Sun, D., Bui, X.L., Magnetron Sputtered Hard and yet tough nanomposite coatings with Case studies: Nanocrystalline TiN embedded in amorphous SiNx, in Nanocomposite thin fims and Coatings, Sam Zhang, et al., Editors. 2007, Imperial College Press: London. 1-104.
7. Veprek, S., Zhang, R.F., Veprek-Heijman, M.G.J., Sheng, S.H., Argon, A.S., Superhard nanocomposites: Origin of hardness enhancement, properties and applications. Surface & Coatings Technology, 204 (2010) 1898-1906.
8. Veprek, S., Zhang, R.F., Veprek-Heijman, M.G.J., Chemistry, physics and fracture mechanics in search for superhard materials, and the origin of superhardness in nc-TiN/a-Si_3N_4 and related nanocomposites, Journal of Physics and Chemistry of Solids, 68 (2007) 1161-1168.
9. Veprek, S., Veprek-Heijman, M.G.J., Industrial applications of superhard nanocomposite coatings, Surface & Coatings Technology, 202 (2008) 5063-5073.
10. Holubar, P., Jilek, M., Sima. M., Present and possible future applications of superhard nanocomposite coatings, Surface and Coatings Technology, 133-134 (2000) 145-151
11. Veprek, S., Argon, A.S., Towards the understanding of mechanical properties of super- and ultrahard nanocomposites, Journal of Vacuum Science & Technology B, 20 (2002) 650-664.
12. Ma, L.W., Cairney, J.M., Hoffman, M.J., Munroe, P.R., Deformation and fracture of Ti-Si-N nanocomposite films, Thin Solid Films, 479 (2005) 193-200.
13. Veprek, S., Veprek-Heijman, M.G.J., Karvankova, P., Prochazka, J., Different approaches to superhard coatings and nanocomposites, Thin Solid Films, 476 (2005) 1-29.
14. Zhang, S., Wang, H.L., Ong, S.E., Sun, D., Bui, X.L., Hard yet tough nanocomposite coatings - Present status and future trends, Plasma Processes and Polymers, 4 (2007) 219-228.

15. Zhang, S., Bui, X.L., Zeng, X.T., Li, X.M., Towards high adherent and tough a-C coatings, Thin Solid Films, 482 (2005) 138-144.

16. Voevodin, A.A., Shatansky, D.V., Levashov, E.A., Moore, J.J., Nanostructured Thin Films and Nanodispersion Strengthened Coatings, Series II, Vol. 155 (2003) Dordrecht: Kluwer Academic Publishers, 1-321.

17. Zhang, S., Ali, N., Nanocomposite thin fims and Coatings: Processing, Properties and Performance, Vol. 1. (2007), London: Imperial College Press, 1- 607.

18. Ohring, M., Materials Science of Thin Films: Deposition and Structure, 2nd ed, (2002) New Jersey Press: Elsevier, 1-783.

19. Zhong, D., Mishra, B. Moore, J.J., Madan, A., Effect of pulsed plasma processing on controlling nanostructure and properties of thin film/coatings, Surface Engineering, 20 (2004) 196-204.

20. Simunkova, S., Blahova, O., Stepanek, I., Mechanical properties of thin film-substrate systems, Journal of Materials Processing Technology, 133 (2003) 189-194.

21. Shtansky, D.V., Multicomponent nanostructured thin films. Deposition, characterization, testing and application, in Nanostructured Thin Films and Nanodispersion Strengthened Coatings, A.A. Voevodin, et al., Editors. Vol- 155 (2003), Springer: Netherlands, 155-165.

22. Mayrhofer, P.H., Mitterer, C., Hultman, L., Clemens, H., Microstructural design of hard coatings, Progress in Materials Science, 51 (2006) 1032-1114.

23. Zhang, R.F., Veprek, S., On the spinodal nature of the phase segregation and formation of stable nanostructure in the Ti-Si-N system. Materials Science and Engineering A, 424 (2006) 128-137.

24. Barshilia, H.C., Deepthi, B., Prabhu, A. S. A., Rajam, K.S., Superhard nanocomposite coatings of TiN/Si_3N_4 prepared by reactive direct current unbalanced magnetron sputtering, Surface & Coatings Technology, 201 (2006) 329-337.

25. Shum, P.W., Li, K.Y., Shen, Y.G., Improvement of high-speed turning performance of Ti-Al-N coatings by using a pre-treatment of high-energy ion implantation, Surface & Coatings Technology, 198 (2005) 414-419.

26. Jiang, N., Shen, Y.G., Mai, Y.W., Chan, T., Tung, S.C., Nanocomposite Ti-Si-N films deposited by reactive unbalanced magnetron sputtering at room temperature, Materials Science and Engineering B, 106 (2004) 163-171.

27. Zhang, C.H., Lu, X.C., Wang, H., Luo, J. B., Shen, Y.G., Li, K.Y., Microstructure, mechanical properties, and oxidation resistance of nanocomposite Ti-Si-N coatings, Applied Surface Science, 252 (2006) 6141-6153.

28. Li, Z.G., Miyake, S., Makino, M., Wu, Y.X., Structure and properties of Ti–Si–N films with ~10 at.% Si deposited using reactive magnetron sputtering with high-flux low-energy ion assistance, Thin Solid Films, 516 (2008) 6548-6552.

29. Rodil, S.E., Olaya, J.J., Unbalanced magnetic field configuration: plasma and film properties, Journal of Physics-Condensed Matter, 18 (2006) S1703-S1719.

30. Martina, P.J., Bendavid, A., Cairney, J.M., Nanocomposite Ti–Si–N, Zr–Si–N, Ti–Al–Si–N, Ti–Al–V–Si–N thin film coatings deposited by vacuum arc deposition, Surface & Coatings Technology, 200 (2002) 2228-2235.

31. Koch, C.C., Structural nanocrystalline materials: an overview. Journal of Materials Science 42 (2007) 1403-1414.

32. Ma, D.Y., Ma, S.L., Xu, K.W., The tribological and structural characterization of nano-structured Ti-Si-N films coated by pulsed-d.c. plasma enhanced CVD, Vacuum, 79 (2005) 7-13.

33. Diserens, M., Patscheider, J., Levy. F., Mechanical properties and oxidation resistance of nanocomposite TiN-SiNx physical-vapor-deposited thin films, Surface and Coatings Technology 120–121 (1999) 158-165.

34. Musil, J., Vlcek, J., Regent, F., Kunc, F., Zeman, H., Hard nanocomposite coatings prepared by magnetron sputtering. Key Engineering Materials, 230-232 (2002) 613-622.

35. Musil, J., Novák, P., Čerstvý, R., Soukup, Z., Tribological and mechanical properties of nanocrystalline- TiC/a-C nanocomposite thin films, Journal of Vacuum Science & Technology A, 28 (2010) 244-249.

36. No, J.T., O, J.H., Lee, C., Evaluation of Ti–Si–N as a diffusion barrier between copper and silicon, Materials Chemistry and Physics 63 (2000) 44-49.

37. Nose, M., Deguchi, Y., Mae, T., Honbo, E., Nagae, T., Nogi, K., Influence of sputtering conditions on the structure and properties of Ti-Si-N thin films prepared by r.f.-reactive sputtering. Surface & Coatings Technology, 174-175 (2002) 261-265.

38. Sharkeev, Y.P., Bull, S.J., Perry, A.J., Klingenberg, M.L., Fortuna, S.V., Michler, M., Manory, R.R., Shulepov, I.A., On high dose nitrogen implantation of PVD titanium nitride, Surface & Coatings Technology, 200 (2006) 5915-5920.

39. Zhang, R.F., Veprek, S., Phase stabilities of self-organized nc-TiN/a-Si_3N_4 nanocomposites and of $Ti_{1-x}S_xN_y$ solid solutions studied by ab initio calculation and thermodynamic modelling, Thin Solid Films, 516 (2008) 2264-2275.

40. Veprek, S., Jilek, M., Super- and ultrahard nanacomposite coatings: generic concept for their preparation, properties and industrial applications. Vacuum, 67 (2002) 443-449.

41. Mannling, H. D., Patil, D. S., Moto, K., Jilek, M., Veprek, S., Thermal stability of superhard nanocomposite coatings consisting of immiscible nitrides, Surface and Coatings Technology 146 –147 (2001) 263-267.

42. Sambasivan, S., Petuskey, W.T., Phase Chemistry in the TI-SI-N system Thermo-mechanical review with phase-stability diagrams, Journal of Materials Research, 9 (1994) 2362-2369.

43. Bendavid, A., Martin, P.J., Preston, E.W., Cairney, J., Xie, Z.H., Hoffman, M., Deposition of nanocomposite thin films by a hybrid cathodic arc and chemical vapour technique. Surface & Coatings Technology, 201 (2006) 4139-4144.

44. Chang, C.L., Hsieh, T.J., Effect of C_2H_2 gas flow rate on synthesis and characteristics of Ti-Si-C-N coating by cathodic arc plasma evaporation, Journal of Materials Processing Technology, 209 (2009) 5521-5526.

45. Chang, C.L., Lin, C.T., Tsai, P.C., Ho, W.Y., Liu, W.J., Wang, D.Y., Mechanical and corrosion properties of (Ti,Si)N coating synthesized by cathodic arc plasma evaporation. Surface & Coatings Technology, 202 (2008) 5516-5520.

46. Chang, C. L., Lin, C.T., Tsai, P.C., Ho, W.Y., Wang, D.Y., Influence of bias voltages on the structure and wear properties of TiSiN coating synthesized by cathodic arc plasma evaporation. Thin Solid Films, 516 (2008) 5324-5329.

47. Jun, K., Shimogaki, Y., Development of TiSiN CVD process using TiCl4/SiH4/NH3 chemistry for ULSI anti-oxidation barrier applications, Science and Technology of Advanced Materials, 5 (2004) 549-554.

48. Cheng, Y.H., Browne, T., Heckerman, B., Meletis, E.I., Mechanical and tribological properties of nanocomposite TiSiN coatings. Surface & Coatings Technology, 204 (2010) 2123-2129.

49. Guo, C.T., Lee, D., Chen, P.C., Deposition of TiSiN coatings by arc ion plating process. Applied Surface Science, 254 (2008) 3130-3136.

50. Liu, Z. J., Zhang, C.H., Shen, Y.G., Mai, Y.W., Monte Carlo simulation of nanocrystalline TiN/amorphous SiNx composite films, Journal of Applied Physics, 95 (2004.) 758-760.

51. Steyer, P., Pilloud, D., Pierson, J. F., Millet, J.P., Charnay, M., Stauder, B., Jacquot, P., Oxidation resistance improvement of arc-evaporated TiN hard coatings by silicon addition, Surface & Coatings Technology, 201 (2006) 4158-4162

52. Jedrzejowski, P., Klemberg-Sapieha, J.E., Martinu, L., Relationship between the mechanical properties and the microstructure of nanocomposite $TiN/SiN_{1.3}$ coatings prepared by low temperature plasma enhanced chemical vapor deposition. Thin Solid Films, 426 (2003) 150-159.

53. Flink, A., Beckers, M., Sjolen, J., Larsson, T., Braun, S., Karlsson, L., Hultman, L., The location and effects of Si in (Ti1-xSix)Ny thin films, Journal of Materials Research, 24 (2009) 2483-2498.

54. Xie, Z. H., Hoffman, M., Moon, R. J., Munroe, P. R., Deformation of a hard coating on ductile substrate system during nanoindentation: Role of the coating microstructure, Journal of Materials Research, 21 (2006) 437-447.

55. Cairney, J.M., Munroe, P.R., Hoffman, M., The application of focused ion beam technology to the characterization of coatings. Surface & Coatings Technology, 198 (2005) 165-168.

56. Munroe, P.R., The application of focused ion beam microscopy in the material sciences, 60 (2009) 2-13

57. Xie, Z. H., Munroe, P.R., Moon, R. J., Hoffman, M., Characterization of surface contact-induced fracture in ceramics using a focused ion beam miller, Wear, 255 (2003) 651-656.

58. Wo, P.C., Munroe, P.R., Vasiliev, M., Xie, Z.H., Alameh, K., Kotov, V., A novel technique for microstructure characterization of garnet films. Optical Materials, 32 (2009) 315-322.

59. Wo, P.C., Munroe, P.R., Zhou, Z.F., Li, K.Y., Xie, Z.H., Effects of TiN sublayers on the response of TiSiN nanocomposite coatings to nanoidentation and scratching contacts. Materials Science and Engineering A, 527 (2010) 4447-4457.

60. Wo, P.C., Munroe, P.R., Zhou, Z.F., Xie, Z.H., LI, K.Y., Cross-sectional Transmission electron microscopy of deformed microstructures in monolithic and multilayer TiSiN/TiN films, International Journal of Modern Physics B, 24 (2010) 18-25.

61. Patterson, A.L., The Scherrer Formula for X-Ray Particle Size Determination, Physical Review, 56 (1939) 978-982

62. Klug, H.P., Alexander, L.E., X-ray diffraction procedures for polycrystalline and amorphous Materials (1974), 2nd ed. New York: Wiley-Interscience. 1- 965.

63. Yang, S. M., Chang, Y.Y., Wang, D. Y., Lin, D.Y., Wu, W.T., Mechanical properties of nano-structured Ti-Si-N films synthesized by cathodic arc evaporation, Journal of Alloys and Compounds, 440 (2007) 375-379.

64. Tanaka, K., Akiniwa, Y., Diffraction Measurements of Residual Macrostress and Microstress Using X-Rays, Synchrotron and Neutrons, JSME International Journal, 47 (2004) 252-263.

65. Matsue, T., Hanabusa, T., Ikeuchi, Y., Kusaka, K., Alteration of internal stresses in SiO_2/Cu/TiN thin films by X-ray and Synchrotron radiation due to heat treatment, Vacuum, 80 (2006) 836-839.

66. Hanabusa, T., Kusaka, K., Matsue, T., Nishida, M., Sakata, O., Sato, T., Evaluation of Internal Stresses in Single-,double- and Multi-layered TiN and TiAlN thin films by Synchrotron Radiation, JSME International Journal, 47 (2004) 312-317.

67. Rebouta, L., Tavares, C. J., Aimo, R., Wang, Z., Pischow, K., Alves, E., Rojas, T. C., Odriozola, J.A., Hard nanocomposite Ti-Si-N coatings prepared by DC reactive magnetron sputtering, Surface & Coatings Technology, 133-134 (2000) 234-239.

68. Mege-Revil, A., Steyer, P., Thollet, G., Chiriac, R., Sigala, C., Sanchez-Lopez, J. C., Esnouf, C., Thermo-gravimetric and in situ SEM characterisation of the oxidation phenomena

of protective nanocomposite nitride films deposited on steel, Surface & Coatings Technology, 204 (2009) 893-901.

69. Ahmed, M.S., Xiaoli, Z., Zhou, Z.F., Munroe, P.R., Tan, N.C., Lawrence, K.Y.Li., Xie, Z.H., Effect of Thermal Annealing Upon Residual Stress and Mechanical Properties of Nanostructured TiSiN Coatings on Steel Substrates, Journal of the American Ceramic Society, 94 (2011) 1546-1551.

70. Pilloud, D., Pierson, J.F., Marco de Lucas, M.C., Cavaleiro, A., Study of the structural changes induced by air oxidation in Ti–Si–N hard coatings, Surface & Coatings Technology, 202 (2008) 2413–2417.

71. Michel, M.D., Muhlen, L.V., Achete, C.A., Lepienski, L.M., Fracture toughness, hardness and elastic modulus of hydrogenated amorphous carbon films deposited by chemical vapor deposition, Thin Solid Films, 496 (2006) 481-488.

72. Y.F. Xu, Y.F., Shum, P.W., Zhou, Z.F., Li, K.Y., Effect of high-energy carbon ion implantation on Ti-Al-Si-N coatings by metal vapour vacuum arc, Surface & Coatings Technology, 204 (2010) 1914-1918.

73. Shum, P.W., Zhou, Z.F., Li, K.Y., A study of the structural, mechanical and tribological properties of Ti-Al-N coatings Post-treated by carbon Implantation, Advanced Materials Research, 75 (2009) 7-12.

74. Teixeira, V., Soares, P., Martins, A. J., Carneiro, J., Cerqueira, F., Nanocomposite Metal Amorphous-Carbon Thin Films Deposited by Hybrid PVD and PECVD Technique, Journal of Nanoscience and Nanotechnology, 9 (2009) 4061-4066.

75. Zou, C.W., Wang, H.J., Li, M., Yu, Y.F., Liu, C.S., Guo, L.P., Fu, D.J., Characterization and properties of TiN-containing amorphous Ti-Si-N nanocomposite coatings prepared by arc assisted middle frequency magnetron sputtering, Vacuum, 84 (2010) 817-822.

76. Chang, C.L., Lee, J.W., Tseng, M.D., Microstructure, corrosion and tribological behaviors of TiAlSiN coatings deposited by cathodic arc plasma deposition, Thin Solid Films, 517 (2009) 5231-5236.

77. Chen, L., Du, Y., Wang, S.Q., Wang, A.J., Xu, H.H., Mechanical properties and microstructural evolution of TiN coatings alloyed with Al and Si, Materials Science and Engineering A, 502 (2009) 139-143.

78. Varesi, E., Paviaa, G., Zenkevich, A., Lebedinskii, Y., Besana, P., Giussania, A., Modelli, A., Structural and physical analysis on MOCVD Ti–Si–N films, Journal of Physics and Chemistry of Solids, 68 (2007) 1046–1051.

79. Chang, C.L., Chen, J.H., Tsai, P.C., Ho, W.Y., Wang, D.Y., Synthesis and characterization of nano-composite Ti–Si–N hard coating by filtered cathodic arc deposition, Surface & Coatings Technology, 203 (2008) 619–623.

80. Bhowmick, S. Xie, Z.H., Hoffman, M., Jayaram, V., Biswas, S.K., Nature of contact

deformation of TiN films on steel, Journal of Materials Research, 19 (2004) 2616-2624.

81. Musil, J., Zeman, H., Kunc, F., Vlcek, J., Measurement of hardness of superhard films by microindentation, Materials Science and Engineering A, 340 (2003) 281-285.

82. Chawla, V., Jayaganthan, R., Chandra, R., A study of structural and mechanical properties of sputter deposited nanocomposite Ti–Si–N thin films, Surface & Coatings Technology, 204 (2010) 1582–1589.

83. Pharr, G.M., Oliver, W.C., Measurement of thin film mechanical properties using nanoindentation, MRS Bulletin, 17 (1992) 28-33.

84. Oliver, W.C., Pharr, G.M., Measurement of hardness and elastic modulus by instrument indentation: Advances in understanding and refinements to methodology, Journal of Materials Research, 19 (2004) 3-20.

85. S. H. Kim, J. W. Jang, S. S. Kang, K. H. Kim, Synthesis and mechanical evaluation of nanocomposite coating layer of nc-TiN/a-Si_3N_4 on SKD 11 steel by sputtering, Journal of Materials Processing Technology 130–131 (2002) 283–288.

86. M. P.Wojtan, S. Meier, J. Patscheider, Transmission electron microscopy characterization of TiN/SiNx multilayered coatings plastically deformed by nanoindentation, Thin Solid Films 518 (2010) 4890-4897.

87. Xie, Z.H., Hoffman, M., Munroe, P., Bendavid, A., Martin, P.J., Deformation mechanisms of TiN multilayer coatings alternated by ductile or stiff interlayers, Acta Materialia, 56 (2008) 852-861.

88. Xie, Z.H., Singh, R., Bendavid, A., Martin, P.J., Munroe, P.R., Hoffman, M., Contact damage evolution in a diamond-like carbon (DLC) coating on a stainless steel substrate, Thin Solid Films, 515 (2007) 3196–3201.

89. Chang, C.L., Wang, D.Y., Characterization of surface enhancement of carbon ion-implanted TiN coatings by metal vapor vacuum arc ion implantation, Nuclear Instruments & Methods in Physics Research Section B-Beam Interactions with Materials and Atoms, 194 (2002) 463-468.

90. Endrino, J.L.R., Escobar Galindo, R., Zhang, H.S., Allen, M., Gago, R., Espinosa, A., Anders, A., Structure and properties of silver-containing a-C(H) films deposited by plasma immersion ion implantation, Surface & Coatings Technology, 202 (2008) 3675-3682.

91. Manory, R.R., Mollica, S., Ward, L., Purushotham, K.P., Evans, P., Noorman, J., Perry, A.J., The effects of MEVVA ion implantation on the tribological properties of PVD-TiN films deposited on steel substrates, Surface & Coatings Technology, 155 (2002) 136-140.

92. Shum, P.W., Li, K.Y., Shen, Y.G., Improvement of high-speed turning performance of Ti-Al-N coatings by using a pre-treatment of high-energy ion implantation, Surface & Coatings Technology, 198 (2005) 414-419.

93. Weng, K.W., Chen, Y.C., Han, S., Hsu, C.S., Chen, Y.L., Wang, D.Y., Effects of ion implantation on the microstructure and residual stress of filter arc CrN films, Thin Solid Films, 516 (2008) 5330–5333.

94. Bilek, M.M.M., McKenzie, D.R., Tarrant, R.N., Lim, S.H.M., McCulloch, D.G., Plasma-based ion implantation utilising a cathodic arc plasma, Surface & Coatings Technology, 156 (2002) 136-142.

95. Seidel, F., Stock, H.R., Mayr, P., Carbon, nitrogen and oxygen implantation into TiN coatings, Surface and Coatings Technology, 108–109 (1998) 271-275.

96. Sharkeev, Y.P., Gritsenko, B.P., Fortuna, S.V., Perry, A.J., Modification of metallic materials and hard coatings using metal ion implantation, Vacuum 52 (1999) 247-254.

97. Shum, P.W., Zhou, Z.F., Li, K.Y., Optimisation of carbon implantation pre-treatments on the adhesion strength of amorphous carbon coatings on AISI 440C steel substrates, Surface & Coatings Technology, 166 (2003) 213-220.

98. Chang, C.L., Wu, C.W., Tribological and corrosion behaviors of TiSi(N,O) coatings prepared by cathodic arc plasma deposition, Thin Solid Films, 517 (2009) 5219-5223.

99. Hirschfeld, M.K., Pfohl, C., Rie, K.T., Schultze, J.W., Corrosion properties of titanium based hard coatings on steel, Materials Science and Engineering Technology 29 (1998) 484-495.

100. Jehn, H.A., Improvement of the corrosion resistance of PVD hard coating–substrate systems, Surface and Coatings Technology, 125 (2000) 212-217.

101. Park, J.H., Kwon, S.H., Lee, M.H., Kim, K.H., Effect of Si Addition on the Corrosion Behavior of Ti–Si–N Coatings Prepared by a Hybrid Coating System, Electrochemical and Solid-State Letters, 12 (2009) C13-C15.

102. Lukaszkowicz, K., Sondor, J., Kriz, A., Pancielejko, M., Structure, mechanical properties and corrosion resistance of nanocomposite coatings deposited by PVD technology onto the X6CrNiMoTi17-12-2 and X40CrMoV5-1 steel substrates, Journal of Materials science, 45 (2010) 1629-1637.

103. Yin, L.C., Luan, S., Lv, G.H., Wang, X.Q., Huang, J., Jin, H., Feng, K.C., Yang, S.Z., Effect of Silane Flow Rate on Structure and Corrosion Resistance of Ti-Si-N Thin Films Deposited by a Hybrid Cathodic Arc and Chemical Vapour Process, Chinese Physics Letters, 25 (2008) 4072-4075.

104. Ahmed, M.S., Zhou, Z.F., Munroe, P.R., Lawrence, K.Y.Li., Xie, Z.H., Control of the damage resistance of nanocomposite TiSiN coatings on steels: roles of residual stress, Thin Solid Films, 519 (2011) 5007-5012.

105. Mege-Revil, A., Steyer, P., Cardinal, S., Thollet, G., Esnouf, C., Jacquot, P., Stauder, B., Correlation between thermal fatigue and thermomechanical properties during the oxidation of multilayered TiSiN nanocomposite coatings synthesized by a hybrid physical/chemical vapour deposition process, Thin Solid Films, 518 (2010) 5932-5937.

106. Mariusz B., Seo, D., Residual stress development in UMS TiN coatings, Surface & Coatings Technology, 200 (2005) 1476 -1482.

107. Tonshoff, H.K., Karpuschewski, B., Mohlfeld, A., Seegers, H., Influence of stress distribution on adhesion strength of sputtered hard coatings, Thin Solid Films 332 (1998) 146-150.

108. Bhowmick, S., Kale, A.N., Jayaram, V., Biswas, S.K., Contact damage in TiN coatings on steel, Thin Solid Films, 436 (2003) 250-258.

109. Vlasveld, A.C., Harris, S.G., Doyle, E.D., Lewis, D.B., Munz, W.D., Characterisation and performance of partially filtered arc TiAlN coatings, Surface & Coatings Technology, 149 (2002) 217-224.

110. Liu, Z.J., Jiang, N., Shen, Y.G., Li, X.N., Stress-induced surface damages in Ti-Si-N films grown by magnetron sputtering, Thin Solid Films, 516 (2008) 7609-7614.

111. Bielawski, M., Residual stress control in TiN/Si coatings deposited by unbalanced magnetron sputtering, Surface & Coatings Technology 200 (2006) 3987- 3995.

112. Atar, E., Sarioglu, C., Demirler, U., Kayali, E.S., Cimenoglu, H., Residual stress estimation of ceramic thin films by X-ray diffraction and indentation techniques, Scripta Materialia, 48 (2003) 1331-1336.

113. Ma, C.H., Huang, J.H., Chen, H., Residual stress measurement in textured thin film by grazing-incidence X-ray diffraction, Thin Solid Films, 418 (2002) 73-78.

114. Mendibide, C., Steyera, P., Esnouf, C., Goudeau, P., Thiaudiere, T.D., Gailhanou, M., Fontaine, J., X-ray diffraction analysis of the residual stress state in PVD TiN/CrN multilayer coatings deposited on tool steel, Surface & Coatings Technology, 200 (2005) 165-169.

115. Hanabusa, T., Kusaka, K., Matsue, T., Nishida, M., Sakata, O., Sato, T., Evaluation of internal stresses in TiN thin films by synchrotron radiation, Science direct, 74 (2004) 571-575.

116. Swadener, J.G., Olivas, E.R., Nanoindentation measurement of surface residual stresses in particle-reinforced metal matrix composites, Scripta Materialia, 54 (2006) 263-268.

116. Suresh, S., Giannakopoulos, A.E., A new method for estimating residual stresses by instrumented sharp indentation, Acta Materialia, 46 (1998) 5755-5767.

117. Wow, P.C., Munroe, P.R., Xie, Z., Zhou, Z.F., Li, K.Y., Three-dimensional Visualization of Scratch-Induced Subsurface Damage in TiSiN/TiN Multilayer Coating Using Focused Ion Beam–Scanning Electron Microscopic Tomography Technique, Journal of the American Ceramic Society, 94 (2011) 1598-1604.

118. Heinke, W., Leyland, A., Matthews, A., Berg, G., Friedrich, C., Broszeit, E., Evaluation of PVD nitride coatings, using impact, scratch and Rockwell-C adhesion tests, Thin Solid Films, 270 (1995) 431-438.

119. Xie, Z., Hoffman, M., Munroe, P., Singh, R., Bendavid, A., Martin, P.J., Microstructural response of TiN monolithic and multilayer coatings during microscratch testing, Journal of Materials Research, 22 (2007) 2312-2318.

120. Subramanian, B., Ashok, K., Subramanian, K., Sastikumar, D., Selvan, G., Jayachandran, M., Evaluation of corrosion and wear resistance TiN coated on mild steel with brush plated nickel interlayer, Surface Engineering, 25 (2009) 490-495.

121. Liu , C., Bi, Q., Leyland, A., Matthews, A., An electrochemical impedance spectroscopy study of the corrosion behaviour of PVD coated steels in 0.5 N NaCl aqueous solution: Part II, EIS interpretation of corrosion behaviour, Corrosion Science, 45 (2003) 1257-1273.

122. Grips, V. K.W., Barshilia, H.C., Selvi, V.E., Kalavati, Rajam, K.S., Electrochemical behavior of single layer CrN, TiN, TiAlN coatings and nanolayered TiAlN/CrN multilayer coatings prepared by reactive direct current magnetron sputtering, Thin Solid Films, 514 (2006) 204-211.

123. Yoo, Y.H., Le, D.P., Kim, J.G., Kim, S.K., Vinh, P.V., Corrosion behavior of TiN, TiAlN, TiAlSiN thin films deposited on tool steel in the 3.5 wt.% NaCl solution, Thin Solid Films, 516 (2008) 3544-3548.

124. Olaya, J.J., Rodil, S.E., Muhl, S., Sanchez, E., Comparative study of chromium nitride coatings deposited by unbalanced and balanced magnetron sputtering, Thin Solid Films, 474 (2005) 119-126.

125. P. Panjan, P., Kek-Merl, D., Zupanič, F., Čekada, M., Panjan, M., SEM study of defects in PVD hard coatings using focused ion beam milling, Surface & Coatings Technology, 202 (2008) 2302-2305.

126. P. Panjan, P., Cekada, M., Panjan, M., Kek-Merl, D., Growth defects in PVD hard coatings, Vacuum, 84 (2010) 209-214.

127. Ding, X.Z., Tan, A.L.K., Zeng, X.T., Wang, C., Yue, T., Sun, C.Q., Corrosion resistance of CrAlN and TiAlN coatings deposited by lateral rotating cathode arc, Thin Solid Films, 516 (2008) 5716-5720.

128. Cˇekada, M., Panjan, P., Kek-Merl, D., Panjan, M., Kapun, G., SEM study of defects in PVD hard coatings, Vacuum, 82 (2008) 252-256.

129. Serro, A.P., Completo, C., Colaco, R., Dos Santos, F., Da Silva, C.L., Cabral, J.M.S., Araujo, H., Pires, E., Saramago, B., A comparative study of titanium nitrides, TiN, TiNbN and TiCN, as coatings for biomedical applications, Surface & Coatings Technology, 203 (2009) 3701-3707.

130. Liu, C., Leyland, A., Bi, Q., Matthews, A, Corrosion resistance of multi-layered plasma-assisted physical vapour deposition TiN and CrN coatings, Surface and Coatings Technology, 141 (2001) 164-173.

131. Cai, F., Yang, Q., Huang, X.A., Wei, R.H., Microstructure and Corrosion Behavior of CrN and CrSiCN Coatings, Journal of Materials Engineering and Performance, 19 (2010) 721-727.

132. Chim, Y.C., Ding, X.Z., Zeng, X.T., Zhang, S., Oxidation resistance of TiN, CrN, TiAlN and CrAlN coatings deposited by lateral rotating cathode arc, Thin Solid Films, 51 (2009) 4845-4849.

133. Stockemer, J., Winand, R., Brande, P.V., Comparison of wear and corrosion behaviors of Cr and CrN sputtered coatings, Surface and Coatings Technology, 115 (1999) 230-233.

134. Li, Y.Y., Wu, F.B., Microstructure and corrosion characteristics of CrN/NiP sputtering thin films, Thin Solid Films, 518 (2010) 7527-7531.

135. Liu, C., Bi, Q., Matthews, A., EIS comparison on corrosion performance of PVD TiN and CrN coated mild steel in 0.5 N NaCl aqueous solution, Corrosion Science, 43 (2001) 1953-1961.

136. Perillo, P.M., Corrosion Behavior of Coatings of Titanium Nitride and Titanium-Titanium Nitride on Steel Substrates, Corrosion, 62 (2006) 182-185.

137. Yang, Q., Zhao, L.R., Cai, F., Yang, S., Teer, D.G., Wear, erosion and corrosion resistance of CrTiAlN coating deposited by magnetron sputtering, Surface & Coatings Technology, 202 (2008) 3886-3892.

138. Ahn, S.H., Choi, Y.S., Kim, J.G., Han, J.G., A study on corrosion resistance characteristics of PVD Cr-N coated steels by electrochemical method, Surface and Coatings Technology, 150 (2002) 319-326.

139. Chang, C.L., Chen, W.C., Tsai, P.C., Ho, W.Y., Wang, D.Y., Characteristics and performance of TiSiN/TiAlN multilayers coating synthesized by cathodic arc plasma evaporation, Surface & Coatings Technology, 202 (2007) 987-992.

140. Guo, L.B., Wang, Y.L., Song, F., He, F., Huang, Y., Yan, L.H., Wan, Y.Z., Formation and characterization of Si_5C_3 type silicon carbide by carbon ion implantation with a MEVVA ion source, Materials Letters, 61 (2007) 4083-4085.

141. W. Ensinger, W., Lensch, O., Knecht, J., Volz, K., Matsutani, T., Kiuchi, M., Pitting corrosion of aluminum coated by ion beam assisted deposition of carbon with argon ions at different ion-to-atomarrival ratios, Surface and Coatings Technology, 158-159 (2002) 594-598.

142. Budzynski, P., Skuratov, V. A., Kochanski, T., Mechanical properties of the alloy Ti–6Al–4V irradiated with swift Kr ion, Tribology International, 42 (2009) 1067-1073.

143. Pelletier, H., Nelea, V., Mille, P., Muller, D., Mechanical properties of pulsed laser-deposited hydroxiapatite thin films implanted at high energy with N^+ and Ar^+ ions . Part II : Nano-scratch test with spherical tipped indenter, Nuclear Instruments & Methods in Physics Research B, 216 (2004) 275-280.

144. Perry, A. J., Valvoda, V., Rafaja, D., Williamson, D.L., Sartwell, B.D., On the residual stress and picostructure of titanium nitride films I: Implantation with argon or krypton, Surface & Coatings Technology, 54-55 (1992) 180-185.

145. Zhang, T., Wu Y., Yenwen, Z., Formation and behaviour of ceramic layer by ion-deposited Ti coating using FMEVAD and Ti and C-dual implantation, Nuclear Instruments & Methods in Physics Research B, 184 (2001) 509-514.

146. Chang, Y.Y., Wang, D.Y., Wu, W., Tribological enhancement of CrN coatings by niobium and carbon ion implantation, Surface and Coatings Technology, 177-178 (2004) 441-446.

147. Shum, P.W., Zhou, Z.F., Li, K.Y., Enhancement of adhesion strength and tribological performance of pure carbon coatings on Ti-6Al-4V biomaterials with ion implantation pre-treatments, Tribology International, 40 (2007) 313-318.

148. Bull, S.J., Sharkeev, Y.P., Fortuna, S.V., Shulepov, I.A., Perry, A.J., Mechanism of TiN-coated tool life by nitrogen implantation, Materials Research Society 16 (2001) 3293-3303.

149. Zhao, W.J., Zhao, Z.Q., Ren, X.T., Metal Ion Sources for Ion Beam Implantation, American Institute of Physics 106 (2008) 344-347.

150. Hai, Z., Fei, C., Jianping, W., Study on the Properties of TiN Coatings on Previously Ion-Implanted Pure Magnesium Surface by MEVVA Ion Implantation, Plasma Science and Technology, 9 (2007) 725-727.

151. Veprek, S., Mukherjee, S., Karvankova, P., Mannling, H.D., He, J.L., Moto, K., Prochazka, J., Argon, A.S., Limits to the strength of super- and ultrahard nanocomposite coatings, Journal of Vacuum Science & Technology A, 21 (2003) 532-544.

152. Zhao, X., Xie, Z., Munroe, P., Nanoindentation of hard multilayer coatings: Finite element modelling, Materials Science and Engineering A, 528 (2011) 1111-1116.

Chapter 2 Effect of thermal annealing upon residual stress and mechanical properties of nanostructured TiSiN coatings on steel substrates

This chapter was published as an article in the journal of Journal of American Ceramic Society, 2011 vol. 94, pp 1546-1551. Whilst all efforts were made to retain the original features of this article, minor changes such as the layout, number formats, and font size and style were implemented in order to maintain consistency in the formatting style of the thesis.

2.1 Abstract

Nanostructured TiSiN coatings were deposited onto a tool steel substrate. The coated samples were then annealed under vacuum at temperatures ranging from 400°C to 900°C. Both mechanical properties and residual stresses in the coatings were determined using nanoindentation methods, assisted by finite element analysis. Intrinsic residual stress was found to be dominant in the as-deposited coatings, but decreased with increased annealing temperature. In contrast, thermal annealing has little impact on either the Young's modulus or hardness of the coatings at temperatures up to 800°C. Grazing incidence X-ray diffraction analysis (GI-XRD) indicated that stress relaxation occurred in nanocrystalline TiN grains during thermal annealing. Direct subsurface observation, enabled by focused ion beam microscopy, revealed that microstructural characteristics, responsible for both the Young's modulus and hardness of the coatings remained unaffected during thermal annealing. The degradation of mechanical properties for the coatings annealed at 900°C resulted primarily from the formation of a thin, soft titanium oxide layer at the outer surface.

2.2 Introduction

Nanostructured TiSiN coatings commonly consist of TiN nanocrystallites embedded in an amorphous matrix of silicon nitride [1, 2]. These coatings possess very high hardness and good chemical resistance and, have potential for a wide range of applications from cutting tools to jet engines [2, 3]. It is well known that the mechanical performance of ceramic coatings is

strongly influenced by internal residual stress [4-6]. For example, compressive stresses greater than 10 GPa have been measured in TiSiN coatings using X-ray diffraction (XRD) [4, 7]. The residual stress in TiSiN coatings deposited by physical vapour deposition (PVD) on steel substrates consists of both intrinsic and extrinsic element [8-10]. Intrinsic stresses result primarily from growth defects caused by ion bombardment during deposition [4, 5]. In contrast, extrinsic stress (often termed thermal stress) is principally due to a mismatch in the coefficient of thermal expansion between the coating and its substrate [11, 12]. Extrinsic stress is determined by the deposition temperature and is independent of post-deposition heat treatment [10]. Thermal annealing has been used to reduce intrinsic stresses that are dominant in PVD coatings [11, 13]. Defect annihilation has been found to be responsible for the reduction of intrinsic stress in TiSiN coatings [14]. However, no detailed investigation has been carried out to elucidate any concomitant structural evolution during thermal annealing and its impact on the mechanical properties and residual stress of TiSiN coatings. Compared with the conventional XRD or Stoney's curvature method, nanoindentation has established itself as a simple and effective means to measure the residual stress in thin films and surfaces [15, 16]. In this study, following deposition of TiSiN coatings on a steel substrate, thermal annealing was performed over a range of temperatures. Nanoindentation was used to determine the mechanical properties and residual stress in the treated coatings. Finite element analysis was applied to quantify the extrinsic stress in these coatings. Grazing incidence X-ray diffraction (GI-XRD) was used to characterise the microstructural factors that control the residual stress and mechanical properties of TiSiN coatings on steel. X-ray photoelectron spectroscopy (XPS) was used to probe the surface chemistry of the coatings.

2.3 Experimental

2.3.1 Sample preparation

TiSiN coatings were deposited onto a AISI M42 tool steel substrate (hardened to HRC 65) using a close-field unbalanced magnetron sputtering system (UDP650, Teer Coatings Ltd., UK) that contains three high-purity Ti targets and one Si target. The polished steel substrates (surface roughness, Ra ~0.03 μm) were mounted on a turntable holder between the targets and the target-to-substrate distance was 17 cm. Before deposition, the chamber was evacuated to a background pressure lower than 2×10^{-6} Torr, then a bias voltage of -500 V was used to bombard the substrate for 30 minutes in order to remove the oxide layer and impurities on the surface. During deposition, the bias voltage was reduced to-60 V, and the working pressure of Ar/N_2 mixed gas was kept at 1.3×10^{-3} Torr. A Ti buffer layer of ~0.22 μm in thickness and a TiN

transition layer ~1 μm in thickness were first deposited to improve the adhesion of the TiSiN coatings to the substrates. The substrates were rotated at a speed of 10 rpm to obtain homogenous composition through the coatings. The surface temperature of the central heater (5 kW) was kept at 550°C during deposition. The substrate temperature was measured to be 400°C by infrared thermometer, since it was separated from the heater and heated by radiation. The coating composition was adjusted by controlling the sputtering power applied to each target (Fig. 1). The resultant TiSiN coatings were ~3 μm in thickness and composed of ~40 at.% of Ti, ~10 at.% of Si and ~50 at.% of N. Assuming the volume of constituent atoms equals that of the resultant compounds, the volume percentage of TiN and Si_3N_4 phase was calculated to be 78 % and 22%, respectively. After deposition, the coating samples were annealed for 3 hours in a vacuum furnace (1×10^{-6} Torr) at 400, 500, 600, 700, 800 and 900 °C, respectively.

2.3.2 Nanoindentation tests: mechanical properties and overall residual stresses

A nanoindentation method was used to determine the residual stresses of the coatings and is briefly described here [16]. The geometric parameters involved are shown in Fig. 2. When the contact radius, *a*, is small compared to the indenter radius, *R*, the relation between the penetration depth, *h*, and the contact radius is given as:

$$h = \frac{a}{R^2} \qquad 1)$$

According to the Hertzian contact theory [17, 18], the applied load *P* is related to *h* by

$$P = \frac{4}{3} E_e R^{1/2} h^{3/2} \qquad 2)$$

where E_e is the effective Young's modulus. The mean contact pressure P_m, i.e., the applied load divided by the contact area, can be obtained from Equations 1) and 2) as,

$$P_m = \frac{P}{\pi a^2} = \frac{4aE_e}{3\pi R} \qquad 3)$$

According to the Von Mises yield criteria, the contact pressure at the onset of yielding of the coating can be expressed as:

$$P_m = 1.06\,(\sigma_y - \sigma_R) \qquad 4)$$

where σ_R is the residual stress in the coating. By combining Equations 3) and 4), the residual stress can be determined as:

$$\boldsymbol{\sigma_R = \sigma_Y\left(1 - \frac{1.26}{\pi}\left[\frac{a_0 E_e}{\sigma_Y R}\right]\right)} \quad 5)$$

where a_o is the contact radius at the onset of yielding of the coating and $\frac{a_0 E_e}{\sigma_Y R}$ can be derived by plotting $\frac{h_r}{h}$ against $\frac{a_0 E_e}{\sigma_Y R}$ and extrapolating the data set of $\frac{a_0 E_e}{\sigma_Y R}$ to $\frac{h_r}{h}$= 0. The yield stress, σ_Y, of the coatings is assumed to be one-third of its hardness [19].

A nanoindentation workstation (Ultra-Micro Indentation System 2000, CSIRO, Sydney, Australia), equipped with a spherical indenter of 5 μm radius, was used to measure the residual stress of the TiSiN coatings. Five peak loads, i.e., 10, 20, 30, 40 and 50 mN, were applied to each specimen. 20 indentations were performed for each of the peak loads. A Berkovich indenter was subsequently used to determine the mechanical properties of the coatings, according to a method described elsewhere [20]. Loading and partial unloading tests were carried out under load control with a maximum load of 50 mN. For each test, 20 incremental steps were used. Prior to nanoindentation tests, the area function of the indenter tips was calibrated using standard fused silica specimen [20]. The maximum penetration depth during the tests was found to be less than 10% of the TiSiN coating thickness, which ensured only the coating properties were measured.

2.3.3 Finite element analysis: thermal stress

A commercial finite element modelling software (Comsol Multiphysics 3.5a AB, USA) was used to analyse thermal stress in TiSiN coatings. Two phases, i.e., TiN and Si_3N_4, exist within the coating, characterised by nanocrystal TiN columnar grains bonded by an amorphous Si_3N_4 matrix (Fig. 3 (a)).Two sources are believed to contribute to thermal stress in the coatings: the first source is the mismatch of the coefficient of thermal expansion between the TiN grains and the amorphous Si_3N_4 matrix; the second is the difference in the coefficient of thermal expansion between the TiSiN coating itself and the substrate. A three-dimensional model was employed, firstly, to consider the thermal stress resulted purely from the first source. Looking from the top surface, the coating assumes a multi-cell structure with each cell being a square, composed of a TiN column surrounded by amorphous Si_3N_4 matrix (Fig. 3 (b)). The diameter of the TiN column was assumed to be 50nm. The thickness of the TiSiN coating was 3,000 nm, which is 60 times the column diameter. To construct a finite element model with a geometry which is computationally effective, a section of 100 nm in thickness was used. Models with a film thickness of 3,000 nm were also tested, and the results showed that the present model was valid. It is noted that both the Ti and TiN interlayers were not considered in the model.

The thermal stress from the second source can be seen as a "drag" to the coating layer by the substrate on cooling following deposition, due to the coefficient of thermal expansion of the substrate being larger than that of the TiSiN coating. In the model the thickness of the substrate was set to be 5 mm, which is significantly greater than that of the coating (i.e., 3 μm). Assuming that the bonding between the coating and the substrate is perfect, the substrate would dominate the thermal contraction and determine the final dimensions of the coating. The bending of the substrate is negligible. The boundary conditions are described as follows: the x=0, y=0 and z=0 planes are fixed in the x, y, and z directions, respectively; the x=50nm, y=50nm and z=100 nm planes are allowed to move in the x, y and z directions, respectively. The plane displacements were calculated during simulation. The cooling process was simulated from 400^{o}C. Room temperature was estimated to be 20^{o}C. The physical and mechanical properties used in the simulation are given in Table I.

2.3.4 Glancing incidence X-ray diffraction (GI-XRD): structural analysis of TiSiN coatings

The crystal structure of both as-deposited and annealed coatings was characterised by GI-XRD (Bruker D8 Discover, Karlsruhe, Germany) using CuKα radiation with wavelength, λ of 0.15 nm and an incidence angle of 2°. The patterns were collected over the 2θ range of 20° to 80°.The voltage and current of the X-ray tube were 40 kV and 40 mA, respectively. A step size of 0.02º 2θ was used with a count rate of 4 sec/step.

2.3.5 X-ray photoelectron spectroscopy (XPS): surface chemistry of TiSiN coatings

The surface bonding structure of both as-deposited and annealed TiSiN coatings was probed by XPS (Kratos Axis Ultra DLD XPS spectrometer, Manchester, UK) with AlKα radiation (h_v = 1,253.6 eV). The X-ray anode was operated at 450W and the voltage and the emission current were kept at 12 kV and 12 mA, respectively. The pass energy was fixed at 80 eV to ensure sufficient resolution and sensitivity. The base pressure of the analyzer chamber was maintained at about 10^{-6} Torr. The sample was mounted horizontally on the holder before being transferred into the analyzer chamber. Binding energies were calibrated using C (1s = 284.6 eV), Cu (2p = 932.67 eV), Ag (3d = 368.27 eV) and Au (4f = 83.98 eV).

2.3.6 Cross-sectional observation of the coating microstructure

Sectioning and imaging of the samples was performed using a focused ion beam (FIB) workstation (FEI xP200 focused ion beam microscope, FEI Company, Hillsboro, OR, USA). The procedure has been described elsewhere [21]. Cross-sectional transmission electron microscopy (TEM) specimens were also prepared using the FIB system. Specimens were examined using a field emission gun transmission electron microscope (Philips CM200, Eindhoven, The Netherlands).

2.4 Results

The overall residual stresses in the as-deposited and annealed samples were determined from nanindentation tests using Equation (5)(in which the contact depth, a_0, at the onset of yielding is derived from Fig. 4 (a)) and found to decrease with increasing annealing temperature (Fig. 4 (b)). For the as-deposited sample, the residual stress was 10 ± 1 GPa. Following thermal annealing at 400 °C, the residual stress decreased by ~31%. A further decrease by ~85% was observed after thermal annealing at 900 °C, which reduced the residual stress to 1 ± 0.2 GPa. According to finite element analysis (Figure 5(a)), the average thermal stress components in a plane parallel to the coating surface (i.e., x-y plane) were found to be ~1.0 GPa (second principal stress, compressive) and ~1.1 GPa (third principal stress, compressive), respectively. The average thermal stress in a direction perpendicular to the coating surface was considerably smaller and thus negligible (Figure 5(b)). The resultant equivalent thermal stress (i.e., Von Mises stress) was found to be ~1.1 GPa (Figure 5(c)). For as-deposited coating, the ratio of the thermal stress to the overall residual stress is about 10%, therefore, the intrinsic stress is dominant. Assuming the thermal stress is constant and independent of thermal annealing forallthe samples[10], the decrease of measured residual stress indicates a reduction in the intrinsic stress with increased annealing temperature.

Both Young's modulus and hardness of the as-deposited coating sample appear to decrease following thermal annealing at 400 °C (Fig. 6). However, there was only a slight difference in mechanical properties between the samples annealed at 400 °C and a higher temperature up to 800 °C. Specifically, the Young's modulus of the as-deposited coating was measured to be 510 ± 17 GPa. It decreased by ~4 % when subjected to thermal annealing at 400 °C and a further slight decrease of ~3 % was observed after thermal annealing at 800 °C (Fig. 6(a)). The hardness of the as-deposited coating was measured to be 55 ± 3.2 GPa. It decreased

by ~12 % following thermal annealing at 400 °C and a further decrease of ~6 % was observed after annealing at 800 °C (Fig. 6(b)). Overall, the coatings remained superhard (i.e.,> 40 GPa) and extremely stiff up to 800°C. However, a sudden decrease in mechanical properties, i.e., the Young's modulus by ~13 % and the hardness by ~15 %, was observed after annealing at 900°C.

The broadened peaks from X-ray analysis, as shown in Fig. 7, may result from both nanocrystalline TiN grains and intrinsic stress in the as-deposited and annealed TiSiN coatings up to 800 °C[22]. Assuming that the number of defects such as dislocations and stacking faults was significantly reduced by thermal annealing at 900 °C, the size of TiN grains, *d*, was thus measured to be ~10 nm for the sample annealed at 900 °C, according to the Scherrer formula [23]:

$$\boldsymbol{d = \frac{C\lambda}{\beta cos\theta}} \qquad 6)$$

where $\boldsymbol{C}$ is a constant and equal to 0.91 and $\boldsymbol{\beta}$ is the peak width at half maximum of TiN (220) peak height. The observed peak shift and sharpening with increasing annealing temperature is apparently associated with the stress relaxation of TiSiN coatings. The fact that the TiN (220) reflection is dominant in the XRD diffractogram indicates that a strong fibre-like texture exists, which is consistent with TEM analysis. However, it is worth noting that the observed asymmetry of the (220) reflection from the sample annealed at 900°C indicates a thin layer of titanium oxide might have formed at the coating surface with overlapping peaks.

XPS analysis was used to probe the new phase apparent on the surface of the sample annealed at 900°C (Fig. 8). The as-deposited sample showed only one peak at 454.7eV, which corresponds to the binding energy of Ti-N. In comparison, the sample annealed at 900°C showed not only the characteristic peak of Ti-N bond, but also a distinct peak at the binding energy of 457.3 eV, indicative of the existence of TiO phase on the surface. Note that the binding energy range of TiO_2 is 458.4 to 459 eV which is not dominant in XPS spactra comparing to TiO phase peak.

The microstructure of both the as-deposited and samples annealed at 800°C and 900°C was examined using FIB (Fig. 9). For all these coatings, a TiN transition layer is visible underneath the outer nanostructured TiSN coating is. The TiN layer is bonded to the steel substrate by a thin Ti buffer layer. No significant change in microstructure can be observed with increasing the thermal annealing temperature.

2.5 Discussion

The residual stresses in PVD coatings have been observed to increase with the coating thickness [4, 11], indicating that the growth-induced (intrinsic) stress plays an increasingly important role in the residual stress of the coatings. By comparing nanoindentation tests with finite element analysis, the dominant role of the intrinsic stress in the residual stress of TiSiN coatings on steel was revealed. It is well known that the intrinsic stress is associated with structural defects, for example, point defects in the coatings. During thermal annealing, atoms in the as-deposited locations moved to less energetic, stable positions, driven by the reduction of strain energy introduced during film growth. The exact extent of structural recovery apparently depends on the annealing temperature. Notably, the thermal stress of TiSiN coatings on steel can also be calculated using an analytical formula [10]:

$$\boldsymbol{\sigma_T = (E_F/1 - \nu_F)(\alpha_F - \alpha_s)(T_{rm} - T_D)} \quad 7)$$

where $\boldsymbol{E_F}$ is the Young's modulus of the film, $\boldsymbol{\nu_F}$ Poisson's ratio of the film (i.e., 0.25), $\boldsymbol{\alpha_F}$ the coefficient of thermal expansion of the film, α_s the coefficient of thermal expansion of steel substrate (i.e.,13× 10^{-6} K^{-1} in Table I), T_{rm} room temperature (i.e., 20°C) and T_D substrate temperature during deposition (i.e., 400°C). $\boldsymbol{\alpha_F}$ is derived from 0.78 ×$\boldsymbol{\alpha TiN}$ + 0.22 ×αSi_3N_4, where $\boldsymbol{\alpha TiN}$ and $\boldsymbol{\alpha Si_3N_4}$ are the coefficient of thermal expansion of TiN and Si_3N_4, respectively (see Table I). The thermal stress of TiSiN coatings is calculated to be 1.10 GPa, which is consistent with the thermal stress determined by the finite element analysis. The major advantage of the finite element analysis is that it can reveal the detailed distribution of all the thermal stress components, as indicated in Fig. 5.

The decrease of hardness of ceramic coatings when subjected to thermal annealing has been observed for binary carbide [24] and nitride coatings [25]. For those coatings, the hardness was regulated by the Hall-Petch effect. The reduction of hardness was attributed to both a decrease in dislocation density and the growth of new, stress-free grains [24]. For nanostructured TiSiN coatings, the hardness is primarily controlled by grain boundary sliding [26]. Although stress relaxation occurred in TiN grains, manifested by the sharpening and shifting of TiN (220) peak [24, 27], no marked change took place in terms of their nanocomposite structure. Since the annealing had little impact on the volume and nature of grain boundary phase (i.e., amorphous Si_3N_4 matrix), a high hardness was maintained which is consistent with the observation by Veprek [28]. The slight decrease in hardness with increasing thermal annealing temperature might result from an increase in TiN grain size. A marked

decrease in hardness for the sample annealed at 900°C apparently resulted from the formation of a thin, soft TiO layer at the outer surface of the TiSiN coating.

The Young's modulus of a solid is determined by its bonding nature [29, 30].Thermal annealing at temperatures up to 800°C had little effect on the nature of bonding in TiSiN coatings. Therefore, their Young's modulus remained high. As with the hardness, the decrease of Young's modulus for the sample annealed at 900°C resulted from the formation of a less stiff oxide layer at the top surface. The oxide phases have been detected on the surface of annealed TiSiN coatings by others previously [14, 31]. It should be pointed out that beneath the thin TiO layer, the mechanical properties of the TiSiN coating would remain comparable to that of the samples annealed at lower temperatures, indicated by their similar microstructure in this work. An investigation on the impact of such thin oxide layer upon the corrosion resistance of the TiSiN coating is under way.

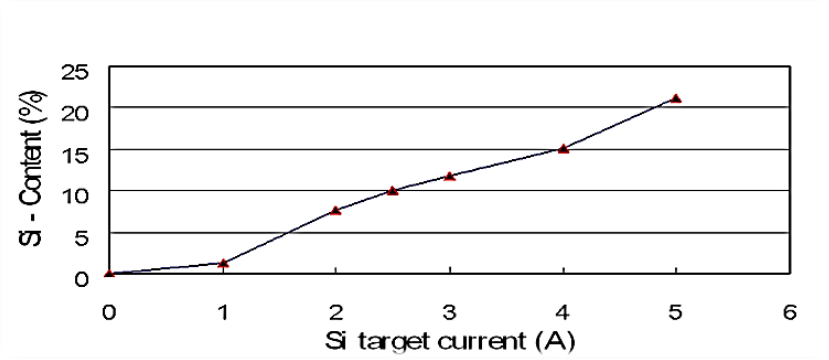

Figure 1: Variation of Si content in TiSiN coatings against Si target current, determined by X-ray photoelectron spectroscopy (XPS). Note that higher Si target current increases the Si content in the resultant TiSiN coatings. In this work, Si target current was set at 2.5 A to ensure nanostructured TiSiN was developed, which is composed of ~10 at.% of Si.

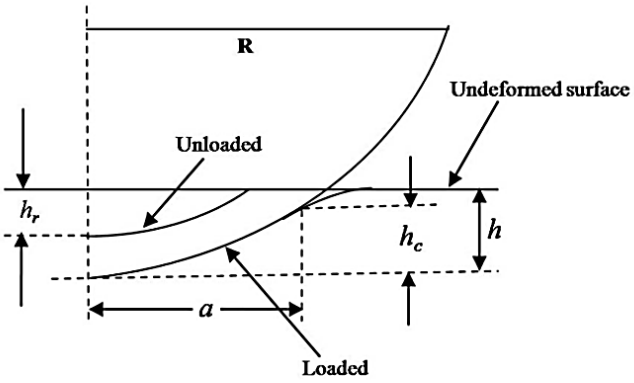

Figure 2: Schematic illustration showing the response of a coated surface to an indentation cycle. Note R is the indenter radius, a, the contact radius, h, the penetration depth at peak load, h_c, is the contact depth at peak load, and h_r, the residual depth of indentation upon unloading [16].

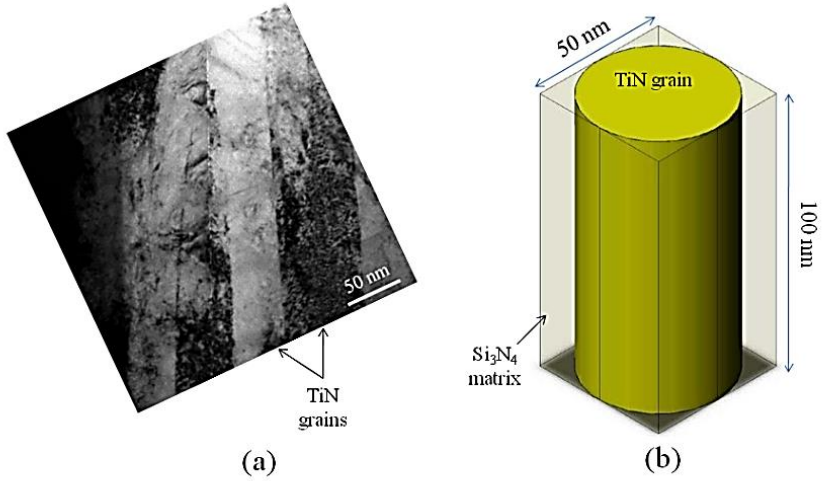

Figure 3(a): Cross-sectional bright field transmission electron micrograph (X-TEM) of a TiSiN coating on steel, showing vertically aligned, columnar TiN grains (~50 nm in diameter). (b) Model geometry used in simulation, showing a TiN grain surrounded by an amorphous Si_3N_4 phase.

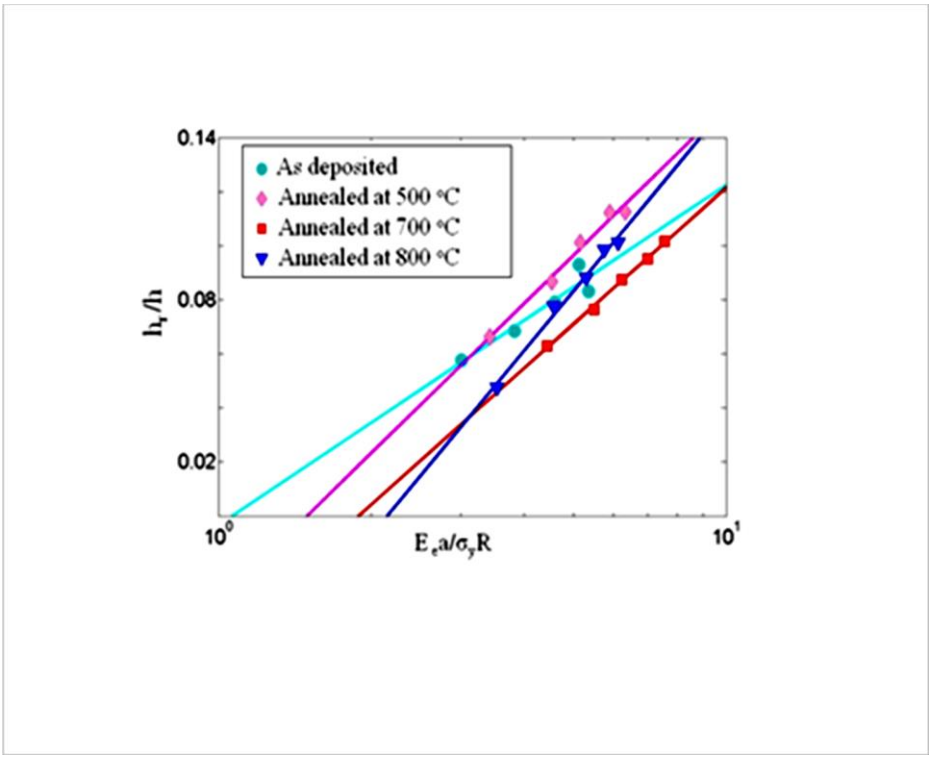

Figure 4(a): Relation of the elastic recovery parameter h_r/h with $E_e a/\sigma_y R$ for both as-deposited and annealed TiSiN coatings. The linear fits are used to determine a_0 at $h_r = 0$.

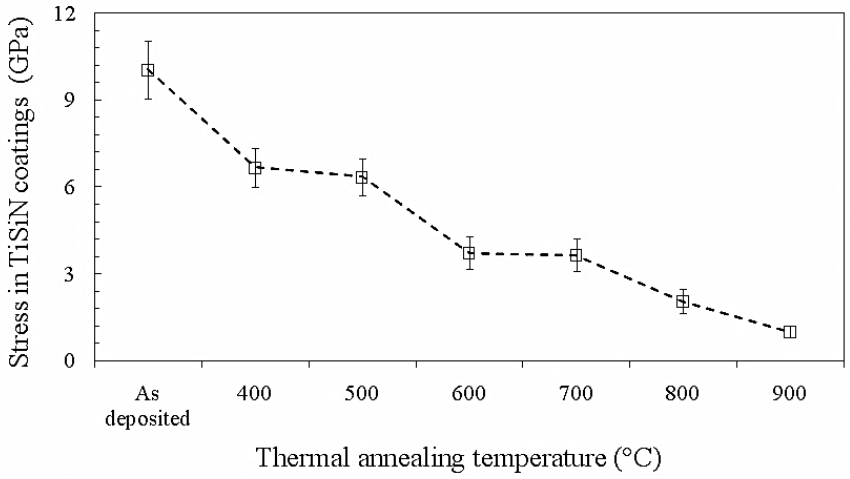

Figure 4(b): Overall residual stress in TiSiN coatings as a function of annealing temperature.

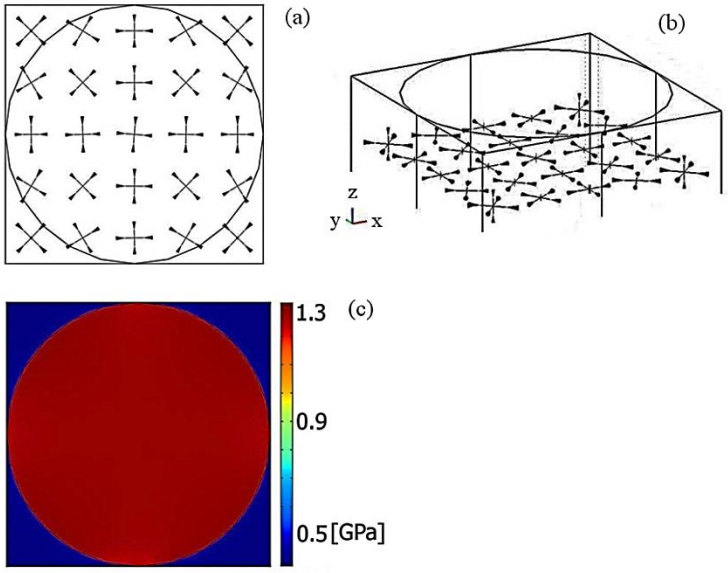

Figure 5: Finite element analyses of thermal stresses in TiSiN coatings on steel. (a)Thermal stress distribution in a plane parallel to the coating surface. (b) Thermal stress distribution in a plane normal to the coating surface (i.e., along z direction). (c) Equivalent stress distribution in a plane parallel to the coating surface. Note equivalent stress distribution is uniform along the z direction.

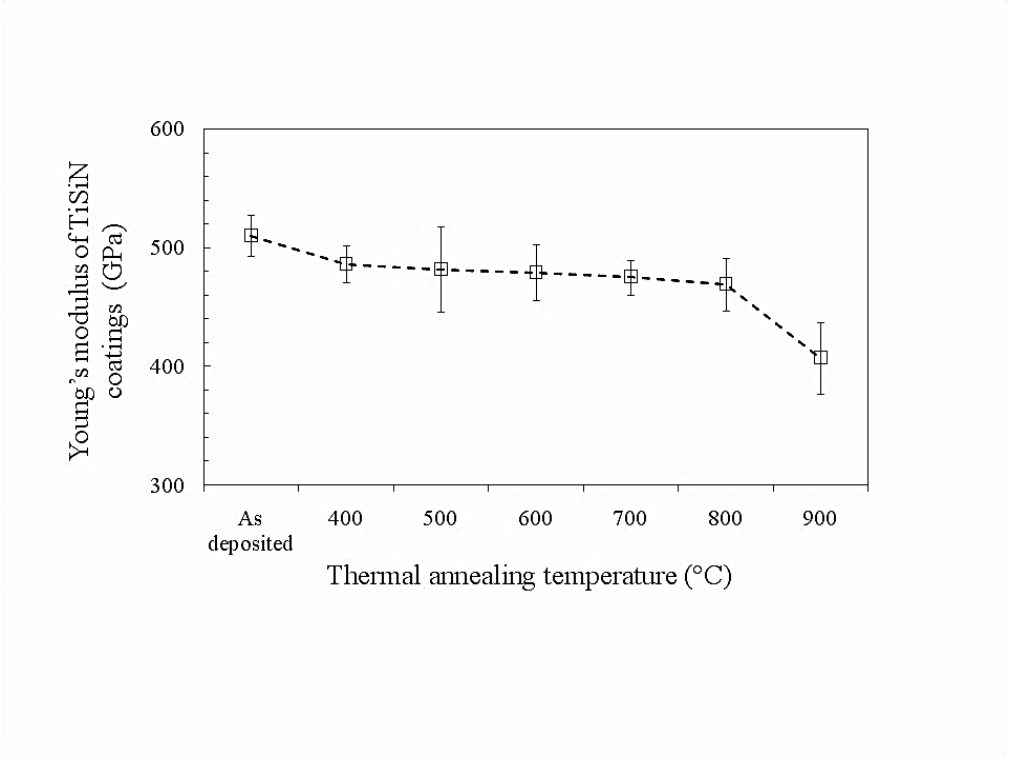

Figure 6(a): Variation of Young's modulus of TiSiN coatings with thermal annealing temperature.

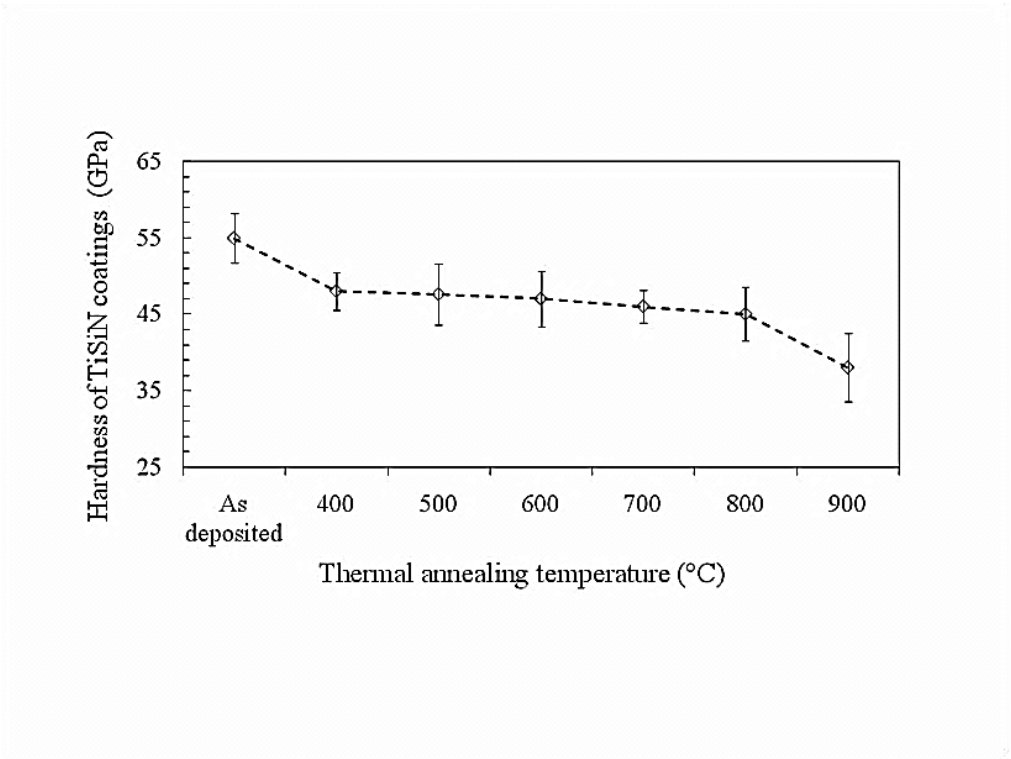

Figure 6(b): Variation of hardness of TiSiN coatings with thermal annealing temperature.

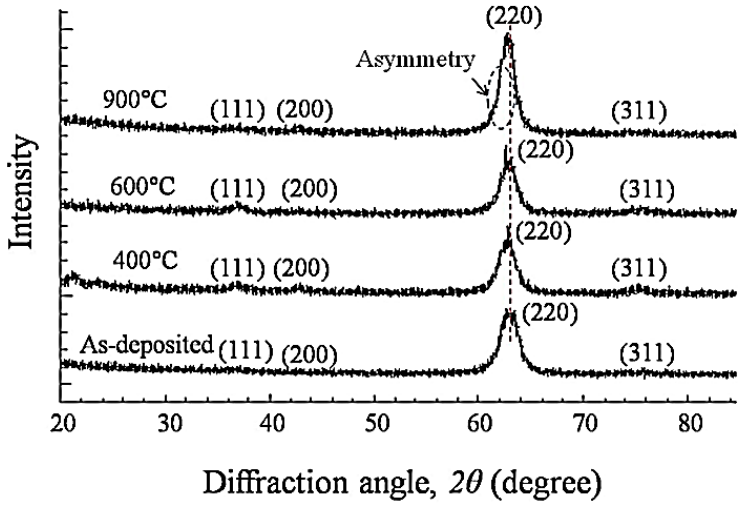

Figure 7: GI-XRD patterns of as-deposited and annealed TiSiN coatings. Patterns have been offset for ease of viewing. Asymmetry of TiN (220) reflection was indicated for the sample annealed at 900 °C.

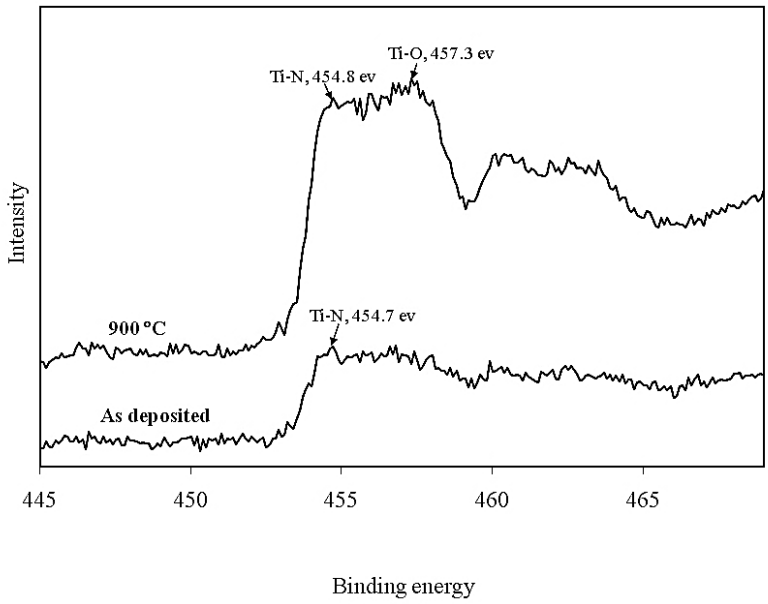

Figure 8: XPS spectra showing the surface bonding states for both as-deposited and annealed sample at 900 °C. Ti-O bond is identified in the annealed sample, indicating that an oxide layer has formed during thermal annealing.

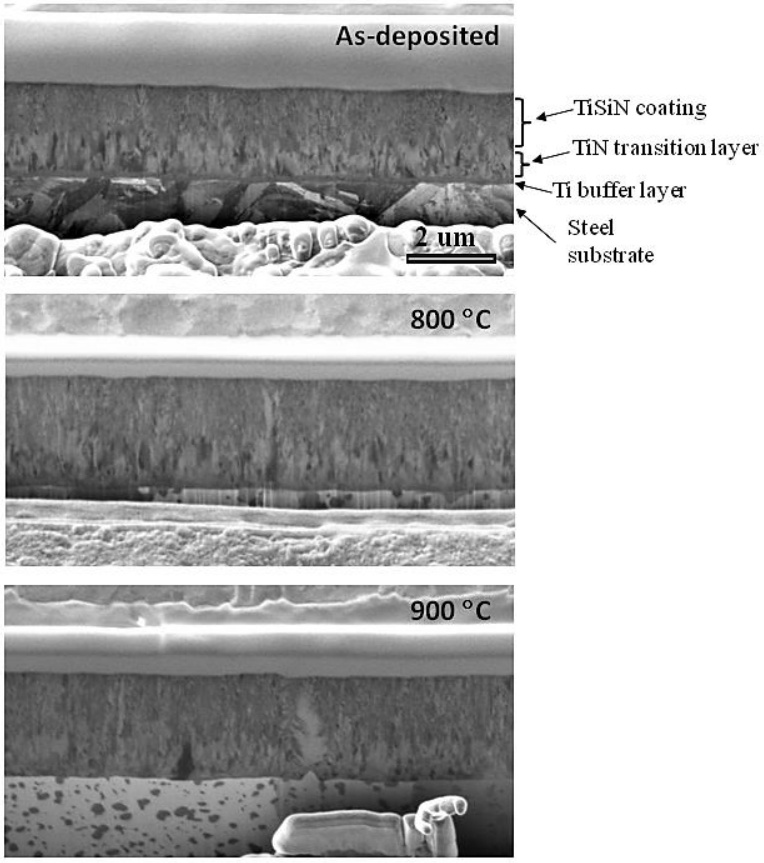

Figure 9: Cross-sectional focused ion beam (FIB) micrographs of a) as-deposited, b) 800 °C and c) 900 °C annealed TiSiN coating on steel, showing a Ti buffer layer, a TiN transitional layer and a nanostructured TiSiN coating. No marked change in microstructure with thermal annealing can be identified.

Table I Physical and mechanical properties of the materials used in simulations

Physical and mechanical properties of TiN and Si_3N_4 used in the simulation[ξ]

	Density (kg/m^3)	Elastic modulus (GPa)	Poisson's ratio	Co-efficient of thermal expansion ($\times 10^{-6}$)
TiN	5,400	590	0.25	11
Si_3N_4	3,190	210	0.25	2.5
AISI M42 steel	-	200	0.30	13

[ξ]Data source:

a) http://www.nist.gov/msel/ceramics/
b) http://www.efunda.com/materials/alloys/

2.6 Conclusions

The effect of thermal annealing upon the mechanical properties and residual stress of nanostructured TiSiN coatings on steel was investigated by means of nanoindentation, finite element modelling, X-ray diffraction, XPS and FIB. The following conclusions can be drawn:

1) Intrinsic stress was found to be considerably greater than thermal stress in nanostructured TiSiN coatings. High intrinsic stress resulted from the structural defects in these coatings.
2) Intrinsic stress can be reduced significantly by the thermal annealing. The extent of stress relaxation depended on thermal annealing temperature.
3) Thermal annealing at temperatures up to 800°C had little impact on the grain boundary structure and bonding states in TiSiN coatings. Therefore, excellent mechanical properties were maintained.
4) Degradation of mechanical properties of TiSiN coatings annealed at 900°C resulted from the formation of a thin, ductile TiO layer on the top surface of the coating during thermal annealing. The present study has demonstrated that thermal annealing can be used to minimise the undesirable compressive residual stress level in nanostructured TiSiN coatings, while maintaining the excellent mechanical properties of these coatings.

2.7 References

1. Guo, C.T., Lee, D., Chen, P.C., Deposition of TiSiN coatings by arc ion plating process, Applied Surface Science, 254 (2008) 3130-3136.

2. Zhang, C.H., Lu, X.C., Wang, H., Luo, J.B., Shen, Y.G., Li, K.Y., Microstructure, mechanical properties, and oxidation resistance of nanocomposite Ti-Si-N coatings, Applied Surface Science 252 (2006) 6141-6153.

3. Jiang, N., Shen, Y.G., Mai, Y.W., Chan, T., Tung, S.C., Nanocomposite Ti-Si-N films deposited by reactive unbalanced magnetron sputtering at room temperature, Materials Science Engineering B. 106 (2004) 163-17.

4. Yang, S.M., Chang, Y.Y., Wang, D.Y., Lin, D.Y., Wu, W.T., Mechanical properties of nano-structured Ti-Si-N films synthesized by cathodic arc evaporation, Journal of Alloys and Compounds, 440 (2007) 375-379.

5. Liu, Z.J., Jiang, N., Shen, Y.G., Li, X., Stress-induced surface damages in Ti-Si-N films grown by magnetron sputtering, Thin Solid Films, 516 (2008) 7609-7614.

6. Barshilia, H.C., Deepthi, B., Prabhu, A.S.A., Rajam, K.S., Superhard nanocomposite coatings of TiN/Si_3N_4 prepared by reactive direct current unbalanced magnetron sputtering, Surface & Coatings Technology 201 (2006) 329-337.

7. Nose, M., Deguchi, Y., Mae, T., Honbo, E., Nagae, T., Nogi, K., Influence of sputtering conditions on the structure and properties of Ti-Si-N thin films prepared by r.f.-reactive sputtering, Surface & Coating Technology, 174-175 (2002) 261-265.

8. Zhang, S., Sun, D., Fu, Y.Q., Du, H., Zhang, Q., Effect of sputtering target power density on topography and residual stress during growth of nanocomposite nc-TiN/a-SiNx thin films, Diamond Related Materials, 13 (2004) 1777-1784.

9. Vlasveld, A.C., Harris, S.G., Doyle, E.D., Lewis, D.B., Munz, W.D., Characterisation and performance of partially filtered arc TiAlN coatings, Surface & Coatings Technology, 149 (2002) 217-224.

10. Bielawski, M., Residual stress control in TiN/Si coatings deposited by unbalanced magnetron sputtering, Surface & Coatings Technology, 200 (2006) 3987-3995.

11. Bielawski, M., Seo, D., Residual stress development in UMS TiN coatings, Surface & Coatings Technology, 200 (2005) 1476 – 1482.

12. Vijgen, R.O.E., Dautzenberg, J.H., Mechanical measurement of the residual stress in thin PVD films, Thin Solid Films, 270 (1995) 264-269.

13. Oettel, H., Wiedemann, R., Residual stresses in PVD hard coatings, Surface & Coatings Technology, 76-77 (1995) 265-273.

14. Flink, A., Beckers, M., Sjolen, J., Larsson, T., Braun, S., Karlsson, L., Hultman, L., The location and effects of Si in $(Ti_{1-x}Si_x)N_y$ thin films, Journal of Materials Research, 24 (2009) 2483-2498.

15. Suresh, S., Giannakopulos, A.E., A new method for estimating residual stresses by instrumented sharp indentation, Acta Materialia, 46 (1998) 5755-5767.

16. Swadener, J.G., Olivas, E.R., Nanoindentation measurement of surface residual stresses in particle-reinforced metal matrix composites, Scripta Materialia, 54 (2006) 263-268.

17. Lawn, B.R., Indentation of Ceramics with Spheres: A Century after Hertz, Journal of American Ceramic Society, 81 (1998) 1977-1994.

18. Bisrat, Y., Roberts, S.G., Residual stress measurement by Hertzian indentation, Materials Science & Engineering A, 288 (2000) 148-153.

19. Lankford, J., Comparative-study of the temperature-dependence of hardness and compressive strength in ceramics, Journal of Materials Science, 18 (1983) 1666-1674.

20. Oliver, W.C., Pharr, G.M., Measurement of hardness and elastic modulus by instrumented indentation: Advances in understanding and refinements to methodology, Journal of Materials Resources 19 (2004) 3-20.

21. Wo, P.C., Munroe, P.R., Vasiliev, M., Xie, Z.H., Alameh, K., Kotov, V., A novel technique for microstructure characterization of garnet film, Optical Materials, 32 (2009) 315-322.

22. Ungar, T., Microstructural parameters from X-ray diffraction peak broadening, Scripta Materialia 51 (2004) 777–781.

23. Alexander, L., Klug, H.P., Determination of crystallite size with the X-ray spectrometer, Journal of Applied Physics 21 (1950) 137-142.

24. Mayrhofer, P.H., Mitterer, C., Hultman, L., Clemens, H., Microstructural design of hard coatings, Progressive Mater ials Science 51 (2006) 1032-1114.

25. Chen, L., Du, Y., Wang, S.Q., Wang, A.J., Xu, H.H., Mechanical properties and microstructural evolution of TiN coatings alloyed with Al and Si, Materials Science Engineering A 502 (2009) 139-143.

26. Zhang, S., Wang, H.L., Ong, S.E., Sun, D., Bui, X.L., Hard yet tough nanocomposite coatings - Present status and future trends, Plasma Processes Polymers, 4 (2007) 219-228.

27. Zois, D., Lekatou, A., Vardavoulias, M., A microstructure and mechanical property investigation on thermally sprayed nanostructured ceramic coatings before and after a sintering treatment, Surface & Coatings Technology 204 (2009) 15-27.

28. Veprek, S., Jilek, M., Super- and ultrahard nanacomposite coatings: generic concept for their preparation, properties and industrial applications, Vacuum, 67 (2002) 443-449.

29. Veprek, S., Argon, A.S., Mechanical properties of superhard nanocomposites, Surface & Coatings Technology, 146-147 (2001) 175-182.

30. Veprek, S., Argon, A.S., Towards the understanding of mechanical properties of super- and ultrahard nanocomposites, Journal of Vacuum Science Technology B 20 (2002) 650-664.

31. Shen, Y.G., Liu, Z.J., Zhang, H.S., Chan, K.H., Effect of silicon addition on surface morphology and structural properties of Titanium nitride films grown by reactive unbalanced ditrect- current magnetron sputtering, Journal of Materials Research, 19 (2003) 523-534 .

Chapter 3 Control of the damage resistance of nanocomposite TiSiN coatings on steels: roles of residual stress

This chapter was published as an article in the journal of Journal of Thin Solid Films, 2011, Vol 519 pp. 5007–5012. Whilst all efforts were made to retain the original features of this article, minor changes such as the layout, number formats, and font size and style were implemented in order to maintain consistency in the formatting style of the thesis.

3.1 Abstract

Thermal annealing has often been used to reduce residual stress and improve mechanical properties and performance of hard coatings. In this work, nanocomposite TiSiN coatings were engineered onto steel substrates by reactive unbalanced magnetron sputtering. Following deposition, thermal annealing was performed at temperatures up to 900°C. A marked decrease in residual stress was observed in the coatings with the increase of thermal annealing temperature. To ascertain the role of residual stress in the response of the coatings to contact damage, nanoindentation was used to probe the damage resistance of the coatings and Rockwell C – test used to evaluate their adhesion strength, as a function of thermal annealing temperature. A combination of high damage resistance and good adhesion strength was observed for the coating annealed at an intermediate temperature of 600°C.

3.2 Introduction

Brittle failure and delamination of ceramic coatings are major problems that hinder their application as a protection layer for components made from ductile materials [1–4] [5-8] [10-13]. Therefore, a considerable amount of work is devoted to understanding and controlling the damage resistance and adhesion of ceramic coatings on steels. To improve the adhesion strength, thermal annealing has been commonly used to reduce the residual stress [5-7], along with the addition of thin transitional layers at the interface between the substrate and the coating [4, 8]. To enhance the damage resistance, multilayer and/or functionally gradient coatings have been developed [9, 10]. An increase in the damage resistance of ceramic coatings was also observed

with the increase of residual stress [2, 11]. A dilemma arises, that is, a decrease in residual stress, on one hand, improve the adhesion strength of a coating, on the other hand, may adversely affect its damage resistance. An intriguing question thus follows – can a combination of high damage resistance and good adhesion of ceramic coatings on steels be achieved by controlling residual stress in the coatings? To answer this question, it is essential to examine the response to mechanical contact of ceramic coatings with differing residual stresses.

The development of nanocomposite structures has opened up the opportunity to improve the mechanical properties of ceramic coatings [12–14]. Nanocomposite TiSiN coatings represent a new generation of materials being developed for surface protection against contact damage [15,16] [2, 9] [2, 14]. They exhibit extremely high hardness (up to 50 GPa) when a particularly strong interface is formed between nano-sized grains, which effectively suppresses grain boundary sliding [17–19]. In addition to high hardness, these coatings are superior to conventional ceramic coatings in terms of damage resistance [8, 19, 20]. It is suggested that both nano-cracking and grain rotation might contribute to the improved damage resistance of these coatings [17, 21, 22]. Considering these, nanocomposite TiSiN coatings are attractive candidates for applications ranging from cutting tools to biomedical devices.

Thermal annealing has been applied to improve the adhesion strength of nanocomposite coatings by reducing residual stress [5, 7]. However, the effect of residual stress on the damage resistance of these coatings remains unclear, primarily due to the difficulties associated with the subsurface observation of the contact damage in these coatings. To tackle this problem, focused ion beam (FIB) microscopy has been introduced to directly examine the subsurface structure of ceramic coatings on ductile substrates with high precision and good contrast[23,24], enabling the identification of the mechanisms through which ceramic coatings deformed[17,25].

In this work, TiSiN coatings, both as-deposited and thermally annealed, on steel substrates were prepared. FIB was used to characterise the coating microstructure. Nanoindentation was performed to measure the residual stress of the coatings. Rockwell C tests were carried out to assess their adhesion strength. FIB was also used to evaluate the damage resistance of the coatings by probing the interaction of coating microstructure with nanoindentation-induced cracks. In the end, a direct link of the residual stress with the damage resistance and adhesion of nanocomposite coatings on steels was established.

3.3 Experimental procedure:

3.3.1Sample preparation:

Nanocomposite TiSiN coatings with a thickness of ~3 μm were deposited onto AISI M42 tool steel substrates by physical vapour deposition (PVD) technique using are active close-field unbalanced magnetron sputtering system (UDP 650, Teer Coatings Ltd., UK) equipped with three Ti and one Si targets. The substrates were mounted on a turntable between the targets and, the target-to-substrate distance was 17 cm. After pumping the chamber to a high vacuum (2×10^{-6} Torr), high-purity (99.999%) Ar inert gas was introduced as working gas at a pressure of 1.1×10^{-6} Torr, then a high negative bias voltage (-500 V) was applied to the substrate holder to generate a plasma by glow discharge. In this case, the Ar ions from the plasma were accelerated to bombard the sample surface for 30 minutes, removing the oxide layer and other contaminants by the sputtering effect [26, 27]. From the X-ray photo spectroscopy (XPS) measurement (ULVAC-PHI 5802 system, Kanagawa, Japan), this process has completely removed the impurities on the steel surface [28]. During deposition the bias voltage was reduced to –60 V and, Ar/N2 gas was introduced and its pressure was kept at ~1.3 ×10-3 Torr. In order to increase the adhesion strength of the coatings, a Ti buffer layer of ~0.22 μm was deposited on to the steel substrates, followed by a TiN transition layer of ~1 μm. The substrates were rotated at a speed of 10 rpm to obtain homogenous film composition. The surface temperature of the central heater was kept at 550 °C. The composition of the TiSiN coatings was controlled by varying the sputtering power applied to Ti and Si targets. The resultant coatings were composed of ~50 at.% of Ti, ~10 at.% of Si and ~40 at.% of N, determined by XPS. After deposition, the samples were annealed for 3 hours in a Carbolite vacuum tube furnace at 400, 600, 800 and 900 °C with base pressure < 1×10^{-6} Torr, heating rate of 5 degree/min.

3.3.2. Observation of coating microstructure and subsurface deformation

A FIB microscope (FEI xP200, FEI Company, Hillsboro, OR, USA) was used to reveal the microstructure characteristics of the coatings and subsurface damage following indentation. Gallium ion beam was used to mill the specimen surface at a high beam current (6,600 pA) and create a wedge-like trench. The resultant rough cross-section was polished at a medium beam current (1,000 pA) to remove particle deposition and smoothen the surface. Finally, the cross-section was imaged at a low beam current (70 pA).

3.3.3 Rockwell-C adhesion test

The adhesion strength of the coatings was examined by Rockwell-C adhesion test. A standard Rockwell-C hardness tester (DXT-1 hardness tester, Matsuzawa, Japan) was used to induce indentation damage with a maximum load of 150 kgf. Following indentation tests, the failure mode was examined using a field emission scanning electron microscope (FESEM) (FEI Dual Beam XL 820, FEI Inc., Portland, Oregon, USA) and classified, according to a widely adopted adhesion strength quality index [29].

3.3.4 Measurement of the residual stress in the coatings

The residual stress of TiSiN coatings was measured using a nanoindenter with a spherical tip of 5 μm in radius (Ultra-Micro Indentation System 2000, CSIRO, Sydney, Australia), based upon a method developed by Swadener et al [30]. For each specimen five maximum load were used, i.e. 10, 20, 30, 40 and 50 mN. Twenty indentations were performed for each load. The maximum penetration depth was found to be less than 10 % of the TiSiN coating thickness during the tests, which ensured only the coating properties were measured. The key formula used for calculating the residual stress, σ_R, of the coatings is

$$\boldsymbol{\sigma_R = \sigma_Y\left(1 - \frac{1.26}{\pi}\left[\frac{a_0 E_e}{\sigma_Y R}\right]\right)} \quad (1)$$

where σ_Y is the yield stress of the coatings, a_o the contact radius at the onset of yielding of the coating, E_e the effective Young's modulus of the coatings and R the indenter radius.

3.4 Results

Load vs depth curves of samples annealed at different temperatures was given in Fig.1. It shows that thermal annealing exerted an influence on the deformation behaviour of the coatings; with the increase of the thermal annealing temperature, the resistance to penetration decreased.

For the as-deposited sample, the residual stress was measured to be 10 ± 1 GPa. The residual stresses of the annealed samples were found to decrease with increasing annealing temperature (Fig.2). Following thermal annealing at 400°C, the residual stress was found to be 6.7 ± 0.7 GPa. A marked decrease in residual stress occurred after thermal annealing at 900°C, for which the residual stress was measured to be 1 ± 0.2 GPa.

The microstructure of both the as-deposited and samples annealed at 800°C and 900°C was examined using FIB (Fig. 3). For all these coatings, both a TiN transition layer and a thin Ti buffer layer were visible underneath the outer nanostructured TiSiN coating. These two interlayers were introduced to improve the adhesion strength of the TiSiN coating on the steel substrate. No significant change in the microstructure of the TiSiN coating can be seen with increasing the thermal annealing temperature, indicating that the high hardness of the coating may be maintained after thermal annealing treatment.

The adhesion strength of the coatings was assessed (Fig. 4). The damage pattern of these samples was examined and their adhesion strength was subsequently ranked on a scale of HF1- HF6 (good to poor quality). The sample annealed at an intermediate temperature of 600°C was found to have good adhesion strength (HF1); no delamination was observed at the edge of the indent. The central regions within the indent also showed good resistance to contact damage, indicative of good damage resistance. However, the samples annealed at both lower (400°C) and higher (900°C) temperatures showed poor adhesion strength (HF5). For the sample annealed at 900°C, severe damage was also seen in the central region of the indent, suggesting a marked decrease in the damage resistance of the coating. The as-deposited sample showed more severe delamination at the edge of contact (HF6), but limited surface damage within the central region of indentation, compared to the sample annealed at 900°C.

To develop a complete understanding of the damage resistance of nanocomposite TiSiN coatings under the influence of residual stress, subsurface structure of indents created by both Berkovich and spherical indenters was examined with the assistance of FIB (Fig.5). For the as-deposited sample, large cracks were observed in the form of ring and lateral cracks. Ring cracks apparently initiated at the contact edge and propagated into the coating. Moreover, lateral cracks formed at the interface between the TiSiN coating and the TiN interlayer. For the sample annealed at 400°C, ring cracks were reduced in terms of number and magnitude, but the lateral cracks remained. With thermal annealing temperature increasing to 600°C (i.e., a further decrease in residual stress), microcracks became increasingly pervasive relative to the large ring and lateral cracks. For the sample annealed at 900°C, neither ring nor lateral cracks were visible and, microcracks were excessive in the structure, leading to a highly deformed indentation site. A summary of the crack pattern, damage resistance, adhesion strength and residual stress of nanocomposite TiSiN coatings as a function of thermal annealing temperature are given in Table I.

3.5 Discussion

High residual stress is commonly found in ceramic coatings prepared by physical vapour deposition on steel substrates. Limited work has been done so far to provide deep insights into the effect of residual stress on the mechanical behaviour of these coatings [2, 11]. The results showed that residual stress played a crucial role in controlling both the damage resistance and adhesion of the nanocomposite coatings on steels. With the presence of high residual stress, the coating behaved in a rather brittle manner, manifested by the formation of relatively large ring and lateral cracks. By reducing the residual stress, the rotation and/or sliding of nano-sized TiN grains was supposed to be activated in the composite structure [31], demonstrated by the formation of an increasing number of microcracks beneath the indentation. Considerable energy was dissipated and the damage resistance of the coatings was thus improved [10, 32]. However, a further reduction in residual stress may weaken the ability of the nanocomposite structure to arrest the cracks and create widespread microcracks that would adversely affect the damage resistance of the coatings. This helps explain the cause of severe damage observed within the central region of the Rockwell indentation for the sample annealed at 900°C.

The adhesion strength was observed to increase by reducing the residual stress in the coatings. This finding is consistent with reports by others on ceramic coatings on ductile substrates [33, 34]. The observed delamination at the contact edge of Rockwell indentation in the sample annealed at 900°C was supposed to be associated with oxidation on the outer layer of the sample [35]. Driven by the stress concentration, ring cracks initiated at surface defects created by oxidation propagated, resulting in the removal of coatings.

In summary, by using thermal annealing to control the residual stress in the nanocomposite coatings, a combination of high damage resistance and good adhesion strength was achieved in the sample annealed at 600°C.

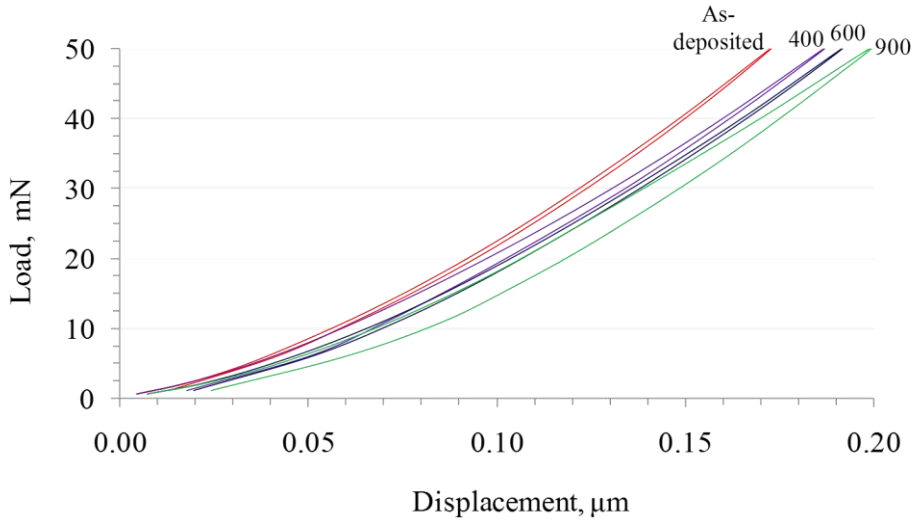

Figure 1: Load vs displacement curves for different TiSiN nanocomposite coated samples.

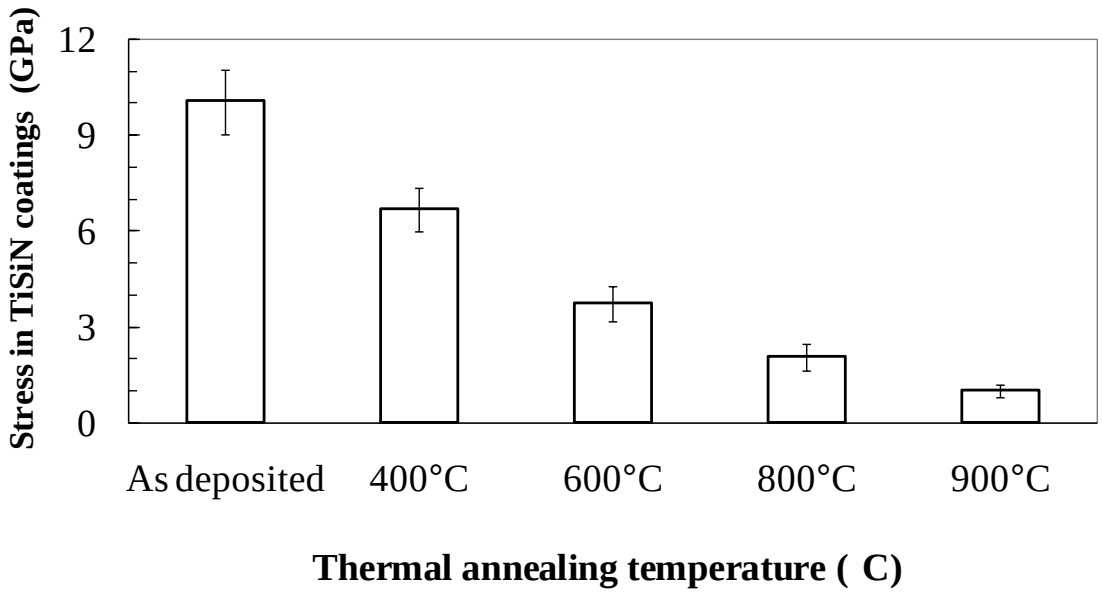

Figure 2: Residual stresses measured in nanocomposite TiSiN coatings as a function of thermal annealing temperature

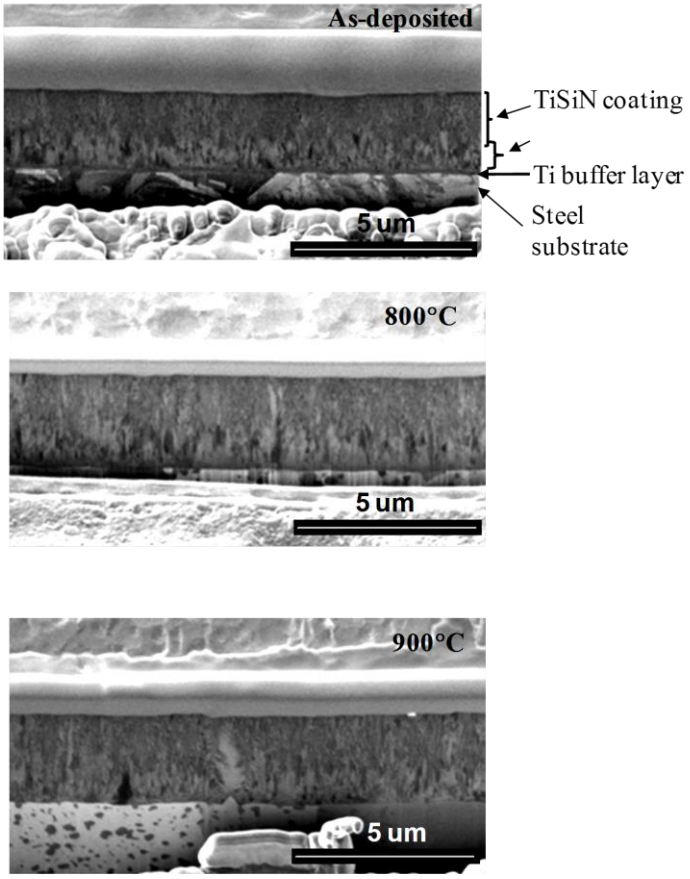

Figure 3: Secondary electron micrographs produced by FIB showing microstructure of nanocomposite coatings. Nanostructured TiSiN coatings are supported by a columnar TiN transition layer, a thin Ti buffer layer in (a) the as-deposited, annealed samples at (b) 800°C and (c) 900°C.

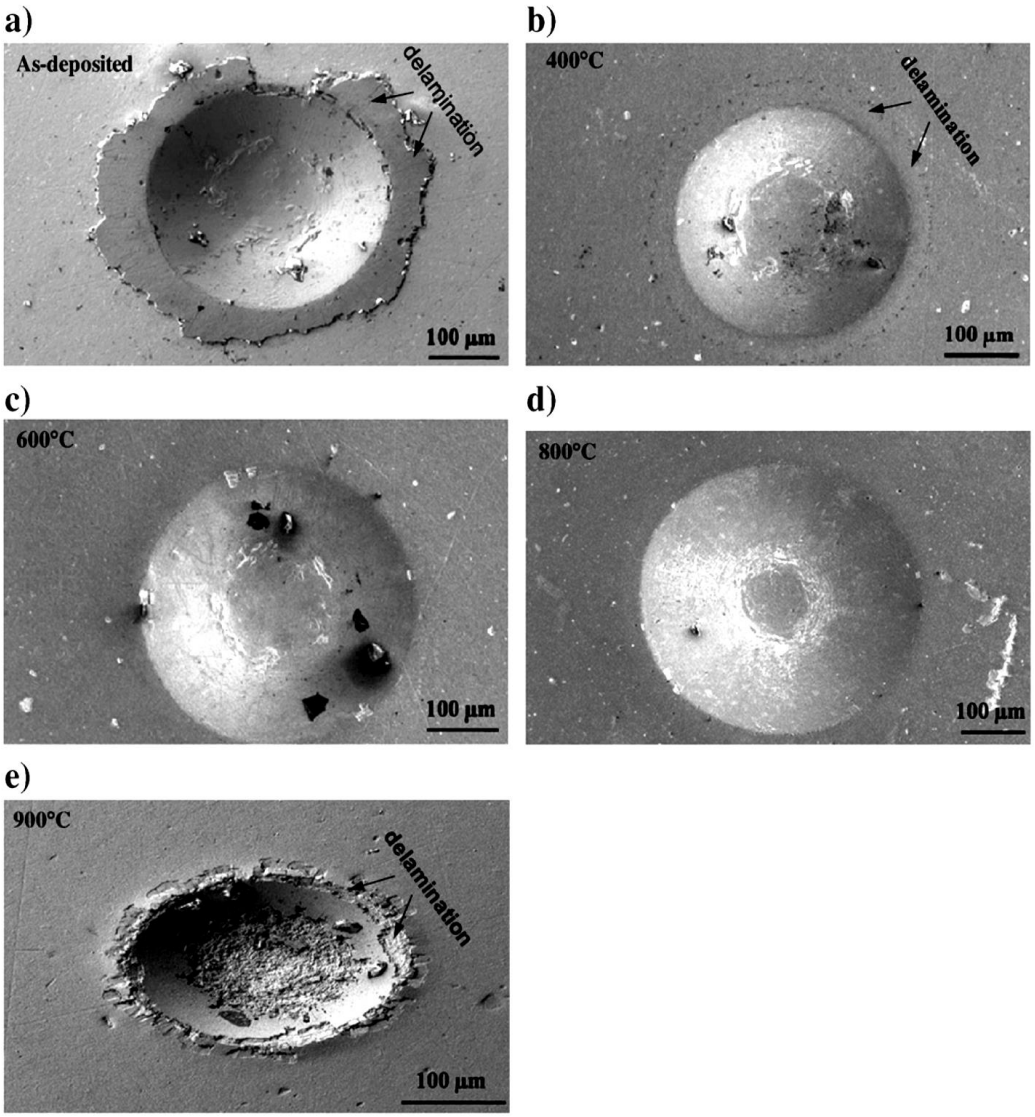

Figure 4: Rockwell-C indentation failure patterns of nanocomposite TiSiN coatings on steel substrates: (a) as-deposited, (b) 400°, (c) 600, (d) 800, (e) 900 °C.

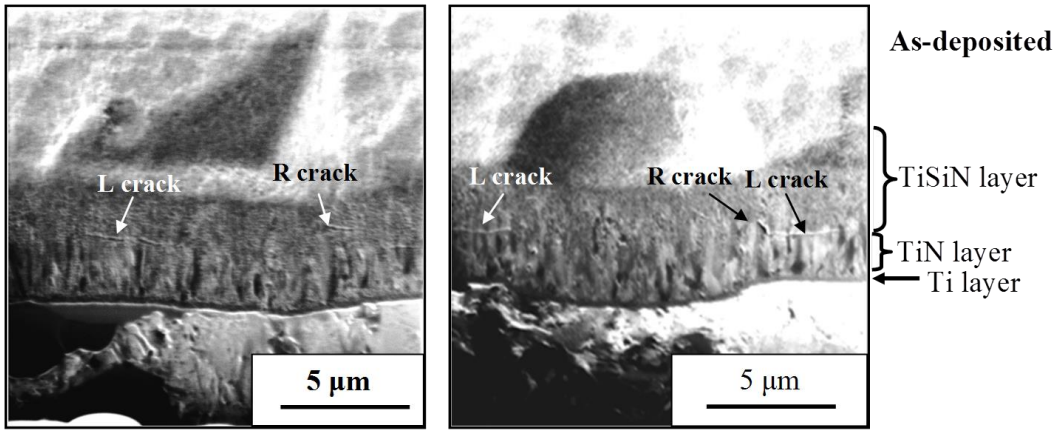
As-deposited
L crack
R crack
L crack
R crack
L crack
TiSiN layer
TiN layer
Ti layer
5 µm
5 µm

(a) (b)

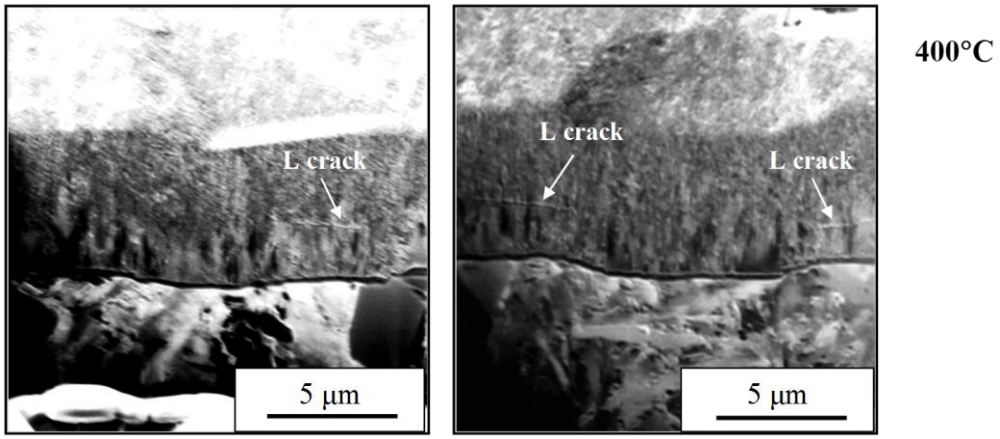
400°C
L crack
L crack
L crack
5 µm
5 µm

(c) (d)

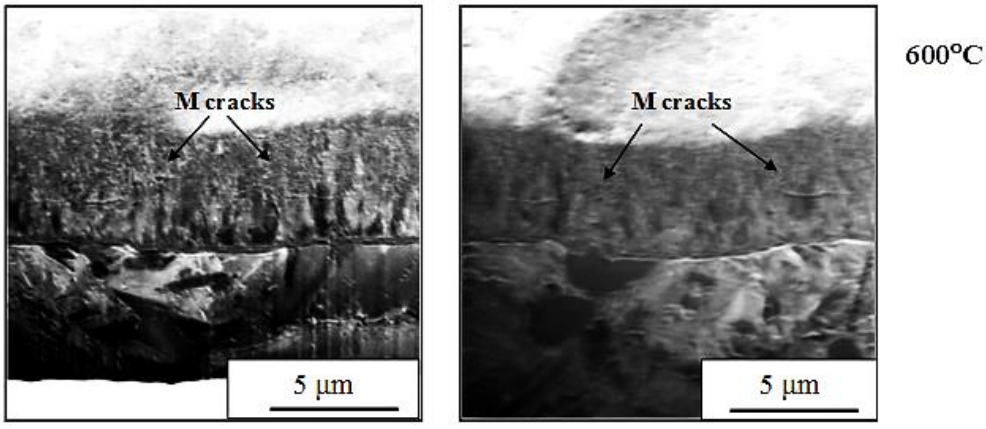
600°C
M cracks
M cracks
5 µm
5 µm

(e) (f)

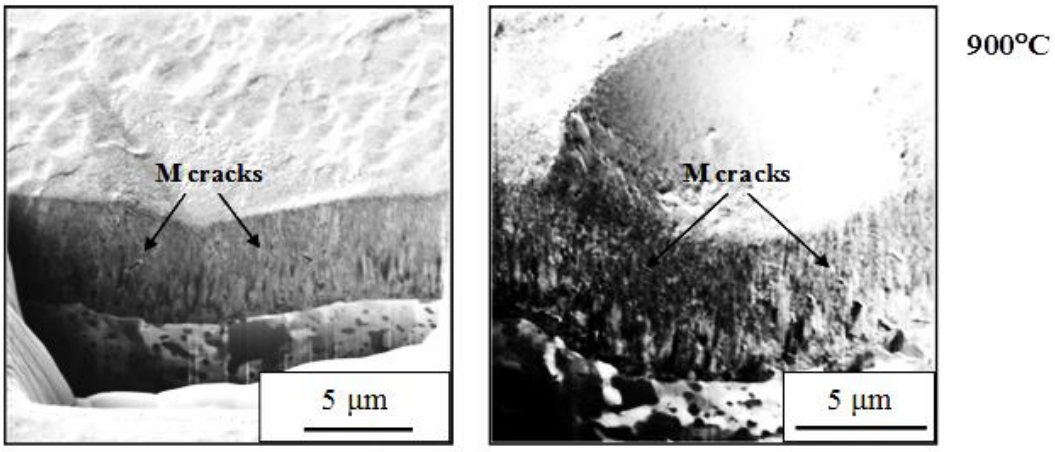

Figure 5: Secondary electron micrographs produced by FIB showing subsurface cracks created by Berkovich (left) and spherical indenter in the as-deposited (a & b), 400 °C (c & d), 600 °C (e & f) and 900 °C (g & h) samples. Note that R = Ring, L = Lateral and M = Micro.

Table I Summary of the crack pattern, damage resistance, adhesion strength and residual stress of different nanocomposite TiSiN coating samples

Sample type	Residual stress (GPa)	Adhesion strengthHF1-HF6 (good to poor quality)	Crack pattern	Damage resistance/Toughness
As deposited	~10.1	HF6	Ring & Lateral cracks	Poor
400°C annealed	~6.7	HF5	Lateral cracks	Poor
600°C annealed	~3.7	HF1	Microcracks	Good
900°C annealed	~1.0	HF5	Extensive Microcracks	Poor

3.7 Conclusion

Enabled by site-specific subsurface observation, this study showed that both the damage resistance and the adhesion strength of nanocomposite TiSiN coatings on steel substrates can be controlled by modulating the residual stress through thermal annealing. The following conclusions can be drawn:

1) The fracture mode of nanocomposite TiSiN coatings changed from brittle to ductile, when compressive residual stress was reduced to a level under which microcracking were activated, replacing relatively large ring and lateral cracks. However, eliminating the residual stress resulted in excessive microcracks that reduced the damage resistance of these coatings.

2) Adhesion strength of the coatings increased with the decrease of residual stress. The observed delamination in the sample annealed at 900°C resulted from the surface oxidation that promoted the growth of ring cracks.

3) A combination of high damage resistance and good adhesion strength was observed for the sample annealed at 600°C.

3.8 References

1. Bhowmick, S., Kale, A.N., Jayaram, V., Biswas, S.K., Contact damage in TiN coatings on steel, Thin Solid Films 436 (2003) 250-258.

2. Bhowmick, S., Jayaram, V., Biswas, S.K., Deconvolution of fracture properties of TiN films on steels from nanoindentation load–displacement curves, Acta Materialia, 53 (2005) 2459-2467.

3. Simunkova, S., Blahova, O., Stepanek, I., Mechanical properties of thin film-substrate systems, Journal of Materials Processing Technology, 133 (2003) 189-194.

4. Chang, C.L., Hsieh, T.J., Effect of C_2H_2 gas flow rate on synthesis and characteristics of Ti-Si-C-N coating by cathodic arc plasma evaporation, Journal of Materials Processing Technology, 209 (2009) 5521-5526.

5. Chang, H.W., Huang, P.K., Yeh, J.W., Davison, A., Tsau, C.H., Yang, C.C., Influence of substrate bias, deposition temperature and post-deposition annealing on the structure and properties of multi-principal-component (AlCrMoSiTi)N coatings, Surface & Coatings Technology, 202 (2008) 3360-3366.

6. Mayrhofer, P.H., Mitterer, C., Hultman, L., Clemens, H., Microstructural design of hard coatings, Progressive Materials Science, 51 (2006) 1032-1114.

7. Chen, L., Dua, Y., Wang, S.Q., Wang, A.J., Xu, H.H., Mechanical properties and microstructural evolution of TiN coatings alloyed with Al and Si. Materials Science and Engineering A, 502 (2009) 139-143.

8. Zhang, C.H., Lu, X.C., Wang, H., Luo, J.B., Shen, Y.G., Li, K.Y., Microstructure, mechanical properties, and oxidation resistance of nanocomposite Ti-Si-N coatings, Applied Surface Science, 252 (2006) 6141-6153.

9. D¨uck, A., Gamer, N., Gesatzke, W., Griepentrog, M., Osterle, W., Sahre, M., Urban, I., Ti/TiN multilayer coatings: deposition technique, characterization and mechanical properties, Surface & Coatings Technology, 142-144 (2001) 579-584.

10. Xie, Z.H., Hoffman, M., Munroe, P., Bendavid, A., Martin, P.J., Deformation mechanisms of TiN multilayer coatings alternated by ductile or stiff interlayers, Acta Materialia, 56 (2008) 852-861.

11. Suresha, S.J., Gunda, R., Jayaram, V., Biswas, S.K., Effect of residual stress on the fracture strength of columnar TiN films, Journal of Materials Research, 22 (2007) 3501-3506.

12. Veprek, S., Argon, A.S., Towards the understanding of mechanical properties of super- and ultrahard nanocomposites, Journal of Vacuum Science Technology B, 20 (2002) 650-664 .

13. Musil, J., Kun, F., Zeman, H., Pola´kova, H., Relationships between hardness, Young's modulus and elastic recovery in hard nanocomposite coatings, Surface & Coatings Technology, 154 (2002) 304-313.

14. Teixeira, V., Soares, P., Martins, A.J., Carneiro, J., Cerqueira, F., Nanocomposite Metal Amorphous-Carbon Thin Films Deposited by Hybrid PVD and PECVD Technique, Journal of Nanoscience and Nanotechnology, 9 (2009) 4061-4066.

15. Barshilia, H.C., Deepthi, B., Prabhu, A.S.A., Rajam, K.S., Superhard nanocomposite coatings of TiN/Si_3N_4 prepared by reactive direct current unbalanced magnetron sputtering, Surface & Coatings Technology, 201 (2006) 329-337.

16. Cheng, Y.H., Browne, T., Heckerman, B., Meletis, E.I., Mechanical and tribological properties of nanocomposite TiSiN coatings, Surface & Coatings Technology, 204 (2010) 2123-2129.

17. Cairney, J.M., Hoffman, M.J., Munroe, P.R., Martin, P.J., Bendavid, A., Deformation and fracture of Ti-Si-N nanocomposite films, Thin Solid Films, 479 (2005) 193-200.

18. Ma, S., Prochazka, J., Karvankova, P., Ma, Q., Niu, X., Wang, X., Ma, D., Xu, K., Veprek, S, Comparative study of the tribological behaviour of superhard nanocomposite coatings nc-TiN/a-Si_3N_4 with TiN, Surface & Coatings Technology, 194 (2005) 143-148.

19. Zhang, S., Wang, H.L., Ong, S.E., Sun, D., Bui, X.L., Hard yet tough nanocomposite coatings - Present status and future trends, Plasma Processes and Polymers, 4 (2007) 219-228.

20. Veprek, S., Argon, A.S., Zhang, R.F., Origin of the hardness enhancement in superhard nc-TiN/a-Si_3N_4 and ultrahard nc-TiN/a-Si_3N_4/$TiSi_2$ nanocomposites, Philosophical Magazine Letters, 87 (2007) 955-966.

21. Veprek, S., Argon, A.S., Mechanical properties of superhard nanocomposites, Surface & Coatings Technology, 146-147 (2001) 175-182.
22. Martina, P.J, Bendavid, A., Cairney, J.M., Nanocomposite Ti–Si–N, Zr–Si–N, Ti–Al–Si–N, Ti–Al–V–Si–N thin film coatings deposited by vacuum arc deposition, Surface & Coatings Technology, 200 (2004) 2228-2235.
23. Cairney, J.M., Munroe, P.R., Hoffman, M., The application of focused ion beam technology to the characterization of coatings, Surface & Coatings Technology, 198 (2005) 165-168.
24. Xie, Z.H., Munroe, P.R., Moon, R.J., Hoffman, M., Characterization of surface contact-induced fracture in ceramics using a focused ion beam miller, Wear, 255 (2003) 651-656.
25. Xie, Z. H., Hoffman, M., Moon, R.J., Munroe, P.R., Deformation of a hard coating on ductile substrate system during nanoindentation: Role of the coating microstructure, Journal of Materials Research, 21 (2006) 437-447.
26. Bull, S.J., Techniques for improving thin-film adhesion, Vacuum. 43 (1992) 517-520.
27. Jiang, N., Shen, Y.G., Zhang, H.J., Bao, S.N., Hou, X.Y., Superhard nanocomposite Ti-Al-Si-N films deposited by reactive unbalanced magnetron sputtering, Materials Science and Engineering B, 135 (2006) 1-9.
28. Mandrino, D., Godec, M., Torkar, M., Jenko, M., Study of oxide protective layers on stainless steel by AES, EDS and XPS, Surface Interface Analysis 40 (2008) 285-289.
29. Heinke, W., Leyland, A., Matthews, A., Berg, G., Friedrich, C., Broszeit, E., Evaluation of PVD nitride coatings, using impact, scratch and Rockwell-C adhesion tests, Thin Solid Films, 270 (1995) 431-438.
30. Swadener, J.G., Olivas, E.R., Nanoindentation measurement of surface residual stresses in particle-reinforced metal matrix composites, Scripta Materialia, 54 (2006) 263-268.
31. Valiev, R.., Nanostructuring of metals by severe plastic deformation for advanced properties, Nature Materials, 3 (2004) 511-516.
32. Peterlik, H., Roschger, P., Klaushofer, K., Fratzl, P., From brittle to ductile fracture of bone, Nature Materials, 5 (2006) 52-55.
33. Chang, C.L., Lin, C.T., Tsai, P.C., Ho, W.Y., Liu, W.J., Wang, D.Y., Mechanical and corrosion properties of (Ti,Si)N coating synthesized by cathodic arc plasma evaporation, Surface & Coatings Technology, 202 (2008) 5516-5520.
34. Teixeira, V., Soares, P., Martins, A.J., Carneiro, J., Cerqueira, F.J., Nanocomposite Metal Amorphous-Carbon Thin Films Deposited by Hybrid PVD and PECVD Technique, Journal of Nanoscience and Nanotechnology, 9 (2009) 4061-4066.
35. Flink, A., Beckers, M., Sjolen, J., Larsson, T., Braun, S., Karlsson, L., Hultman, L., The location and effects of Si in $(Ti_{1-x}Si_x)N_y$ thin films, Journal of Materials Research, 24 (2009) 2483-2498.

Chapter 4 Corrosion behaviour of nanocomposite TiSiN coatings on steel substrates

This chapter was published as an article in the journal of Journal of Corrosion Science, 2011, Vol. 53, pp. 3678-3687. Whilst all efforts were made to retain the original features of this article, minor changes such as the layout, number formats, and font size and style were implemented in order to maintain consistency in the formatting style of the thesis.

4.1 Abstract

Nanocomposite TiSiN coatings deposited on tool steels. Detailed mechanisms that govern the corrosion of these coated steels were revealed, following immersion tests in 70% nitric acid solution. Pitting originated preferentially from coating defect sites and expanded with increasing immersion time. Both Young's modulus and hardness measured by nanoindentation decreased as the corrosion damage intensified. A thin oxide layer formed from the thermal annealing of the as-deposited samples at 900°C was found to be effective against corrosive attack. In addition, compressive residual stress was noted to suppress the propagation of corrosion-induced cracks. Role of residual stress in controlling the corrosion resistance of these ceramic-coated steels is clarified by finite element analysis.

4.2 Introduction

Nanocomposite ceramic coatings have been investigated intensively in recent years for applications in machining tools and medical devices, owing to their high hardness and good wear resistance [1–4]. Among them, TiSiN is commonly applied. Pitting corrosion has been frequently observed in ceramic coatings deposited on steel substrates, originating from surface defect sites [5, 6]. Electron microscopy, surface X-ray diffraction (XRD) and X-ray photoelectron spectroscopic techniques have been used to probe the mechanisms under which these ceramic coated steels corroded [7–9]. However, a detailed understanding of initiation and propagation of corrosion in surface-treated steels is lacking and, consequently, the factors that control the expansion of pitting remains unclear. Though mechanical properties of ceramic coatings are anticipated to deteriorate during corrosion, no data are available to date to

substantiate such a hypothesis, making it difficult to predict the service life of ceramic coated steels in corrosive environments.

High compressive residual stress is known to exist in ceramic coatings prepared by PVD [10, 11]. Although, stress corrosion cracking has often been observed in metals subjected to tensile stresses [12], little effort has been made so far to clarify the effect of compressive residual stress on the corrosion behaviour of ceramic-coated steels. On the other hand, in previous studies on corrosion of ceramic-coated steels, corrosion mechanism was mainly identified from the surface observation [13–15] and direct subsurface observation was rare. Focused ion beam (FIB) microscopy is a powerful tool in the preparation and observation of local cross-sections in a material surface [16, 17]. It has recently been used for subsurface characterization of ceramic coatings following mechanical testing [18, 19].

In this study, FIB, along with XRD, X-ray photoelectron spectroscopy (XPS) and nanoindentation testing, were used to characterise the microstructural evolution in both surface and subsurface after corrosion tests and determine key factors that control the corrosion process. The change of mechanical properties of the coatings under the influence of corrosion was also quantified. Moreover, the effect of residual stress on the corrosion progression was clarified by finite element analysis (FEA).

4.3 Experimental procedure

4.3.1 Sample preparation

Nanocomposite TiSiN coatings were deposited onto AISI M42 tool steel substrates (C: 1.05-1.15, Si: 0.15-0.65, Mn: 0.15-0.4, Cr: 3.5-4.25, V: 0.9-1.35, Mo: 9.0-10.0, W: 1.15-1.85, Co: 7.75-8.75 in wt%; West Yorkshire Steel Co. Ltd, Leeds, UK) by physical vapour deposition (PVD) using a reactive close-field unbalanced magnetron sputtering system (UDP650, Teer Coatings Ltd., Droitwich, Worcestershire, UK). The details of the deposition procedure are given elsewhere [20] and can be summarised as follows: prior to deposition, the surface of the steel substrates was bombarded by Ar ions to remove the oxide layer and other contaminants. During deposition a Ti buffer layer of ~0.2 μm was first deposited, followed by a TiN transition layer of ~1 μm. The thickness of the outer TiSiN coating was ~3 μm and it was composed of ~50 at.% of Ti, ~10 at.% of Si and ~40 at.% of N, as determined by XPS. After deposition, some of the samples were annealed for 3 hours in a Carbolite vacuum tube furnace at 900 °C with a base pressure < 1×10^{-6} Torr and a heating rate of 5°C/min. Compressive residual stress in

as-deposited TiSiN coatings was found to decrease from ~10 GPa to ~1 GPa after the thermal annealing treatment [21]. However, the microstructural features of the annealed samples remained identical to that of the as-deposited specimens, as shown in Figure 1. The size of TiN grains was measured to be ~10 nm for the sample annealed at 900 °C in a recent study [21].

4.3.2 Corrosion tests

Before immersion tests, the samples were coated with an acrylic protective layer (without metallic flakes) to expose only the coated area. The tests were performed in 70% HNO_3 solution at 25°C. The immersion period was set as 2 and 8 days.

4.3.3 Surface structure characterisation

The coating crystal structure of all the samples was characterised by grazing incidence XRD (GI-XRD) at the powder diffraction beam line of the Australian Synchrotron. The energy of the synchrotron radiation was 9.0 keV, which corresponds to a wavelength of 0.13 nm at an incidence angle of 1°. The patterns were collected over the 2θ range of 20° to 80°. The depth of the incidence SR beam was 0.5 μm, according to a formula described elsewhere [22].

The surface bonding structure of both reference and corroded TiSiN coatings were probed by XPS (Kratos Axis Ultra XPS spectrometer, Manchester, UK) with Mg Kα radiation (hν = 1,253.6 eV). The sample was mounted horizontally normal to the entrance of electrostatic lens. The base pressure of the analyser chamber was maintained at ~10^{-9} Torr. The voltage and emission current of X-ray source were kept at 12 kV and 12 mA, respectively. The pass energy were selected at 80 eV for survey scan and 10 eV for the features of interests (i.e., N1s, Ti2p, Si2p) to ensure high resolution and good sensitivity. XPS spectra energy scale was calibrated using Cu2p (932.67 eV), Ag3d (368.27 eV), C1s (284.6 eV) and Au4f (83.98 eV). The electrostatic lens mode and analyser entrance were selected Hybrid and Slot mode (Iris = 0.6 and Aperture = 49), respectively. A charge neutraliser was employed during the XPS measurements.

4.3.4 Surface and subsurface observations

Sectioning and imaging of the surface defects of reference and annealed samples were conducted on a Neon 40EsB focussed ion beam scanning electron microscope (FIB-SEM) (Carl Zeiss NTS GmbH, Oberkochen, Germany). Imaging of the subsurface was achieved using the

FIB to expose a cross-section of the sample. Images were collected using an in-lens secondary electron detector. The surface of both reference and corroded samples was examined using a FEI field emission scanning electron microscope (FESEM) (Model FEI Nova 230, EI Company, Hillsboro, OR, USA). Sectioning and subsurface imaging of samples was also carried out using a FEI xP200 focused ion beam (FIB) workstation. The procedure has been described elsewhere [23]. First, a high gallium ion beam current (7,000 pA) was used to mill through the surface area of interest and to create a wedge-like trench. The resultant rough cross-section was then polished at medium currents (1,000–3,000 pA) to remove particle deposition and smooth the surface. Finally, the cross section was imaged at lower beam currents.

4.3.5 Nanoindentation testing

A nanoindentation system (Ultra-Micro Indentation System 2000, CSIRO, Sydney, Australia), equipped with a Berkovich indenter, was used to measure the mechanical properties of the TiSiN coatings before and after corrosion tests, according to a method proposed by Oliver and Pharr [24]. Prior to nanoindentation testing, the area function of the indenter tip was calibrated using a fused silica specimen. Nanoindentation tests were carried out under load control with a maximum load of 50 mN. For each test, 20 incremental and 20 decremental steps were used. The maximum penetration depth during the tests was found to be less than 10 % of the TiSiN coating thickness, which ensured only the coating properties were measured.

4.3.6 Finite element analysis of residual stress distribution

An axisymmetric model (Comsol Multiphysics software, Version 3.5a, Burlington, MA 01803, USA) was constructed to create a direct link between the residual stress and corrosion resistance. The model that contains the cross section of a cone-shaped cavity, resulting from localised corrosion damage, is shown in Fig. 2(a). The geometry and size of the corrosion damage site described in the model are directly from the subsurface observations enabled by the FIB microscopy in this work. Boundary conditions are given as follows: the left hand side is the axisymmetric axis. The bottom and the right and side are fixed along the z and r directions, respectively, but free to move in the other directions. The overall dimension of the model is much larger than both the thickness of the coating layers, and the edge effect due to boundary constrains is thus negligible. The meshes were generated in an interactive way to ensure that they were sufficiently dense around the edge, which defines the inner wall of the corrosion cavity. Planar compressive residual stresses were assigned to the TiN and TiSiN layers. For the

as-deposited samples, the residual stresses were set to be 3 GPa for the TiN layer [25] and 10 GPa for the TiSiN layer [21]. For the annealed samples, the residual stresses were set to be 0.3 GPa and 1 GPa for the TiN and TiSiN layers, respectively [21]. Under the influence of the residual stress, the percent reduction in the cavity area sectioned along the horizontal direction at a distance of x from the cavity tip can be calculated by $\delta A/A = (r_0^2(x) - r^2(x)) / r_0^2(x)$, where $r(x)$ and $r_0(x)$ are the radii of the cavity area under stress and stress-free conditions, respectively (Fig. 2(b)). Structural and physical parameters of both the substrate and coating materials are given in Table I.

4.4 Results and Discussion

4.4.1 Characterisation of surface crystal structure

The surface crystal structure of the as-deposited and annealed samples were analysed by GI-XRD before and after corrosion tests. Four diffraction peaks identified at the diffraction angles of 32.5°, 39.9°, 64° and 72° corresponded to (1 1 1), (2 0 0), (2 2 0) and (3 1 1) crystal planes of cubic B1 NaCl-type TiN, respectively (Fig.3(a) & (b)). Notably, significantly intensified and sharpened (200) peak appeared in the annealed sample, probably due to the reduction in the number of structural defects and residual stresses induced by thermal annealing at 900 °C. With the increase of immersion test time, the TiN (1 1 1) peak was intensified, indicative of a continuing removal of the outer nanostructured TiSiN layer and the exposure of the columnar-grained TiN transitional layer having a preferred (1 1 1) orientation [26]. In addition, the peaks of molybdenum carbide (Mo_2C) (200) and martensite phase (M) (200) of M42 steel substrate appeared in both types of reference samples, suggesting that surface defects such as pinholes exist in the samples. The peaks of these steel phases were intensified with increasing immersion time, most likely due to the removal of the coatings under acid attack. No diffraction peaks related to Si and its compounds were identified. By comparing the peak intensity of both Mo_2C and M phases in samples before and after immersion tests, the as-deposited samples seemed to be more susceptible to corrosion attack than the annealed ones, though both types of samples exhibited a similar trend in the evolution of peak intensity.

4.4.2 Analysis of the surface chemistry of the coatings

The change in surface chemical bonding states of both as-deposited and annealed samples with the development of corrosion progress were characterised by XPS. From N 1s

spectra, the two peaks at ~396 eV and ~397 eV arise from Ti-O-N and TiN phases, respectively, where as the other peak at 400 eV represents Si_3N_4 (Fig. 4(a) & (b)). Considering that no crystalline Si_3N_4 phase was detected in the samples during GI-XRD analysis (Fig. 3), Si_3N_4 was thought to exist in an amorphous state in TiSiN coatings [27]. The peak of Ti–O–N might be attributed to surface contamination caused by oxygen [28, 29]. By increasing the immersion period to eight days, the intensities of these peaks decreased significantly, presumably due to aggressive attack of the nitric acid on the samples. According to the Ti 2p spectra, two pairs of peaks from Ti 2p3/2 and Ti 2p1/2 were identified before and after the immersion tests, corresponding to TiN and TiO_x phases in the surface of both as-deposited and annealed samples (Fig. 4(c) & (d)). Prior to the corrosion tests, TiO_x prevailed in the annealed sample (Fig. 4(d)), while TiN phase was dominant in the as-deposited sample (Fig. 4(c)), indicating that an oxide layer formed during the thermal treatment at 900°C. Following two days immersion tests, TiO_x remained dominant in the annealed sample. However, surface passivation seemed to occur in the as-deposited sample, making TiO_x the dominant phase. With increasing immersion time up to eight days, the intensities of these peaks decreased for both phases, indicating corrosion progression in the acid solution. Analysis of the binding energy peaks associated to Si 2p spectra shows only one peak at 102.7 eV corresponding to Si_3N_4 phase in both as-deposited and annealed samples (Fig. 4(e) & (f)), whose intensities also decreased with the increase of immersion time in the acid solution. The binding energies of surface phases identified by XPS in the samples before and after corrosion tests are given in Table II.

4.4.3 Nanoindentation tests

Young's modulus and hardness of the as-deposited sample were found to be higher than the annealed sample by ~25% and ~47%, respectively, before immersion tests (Fig. 5). A slight decrease of mechanical properties was observed for both types after two days immersion tests. By immersing the samples in 70% HNO_3 solution for eight days, the as-deposited sample showed a marked decrease in mechanical properties compared to the annealed: for Young's modulus, the as-deposited sample decreased by ~33% and the annealed sample by ~10% (Fig. 5(a)); for hardness, the as-deposited sample decreased by ~ 62% and the annealed samples by ~21% (Fig. 5(b)).

From the XPS analysis, an oxide layer was detected on the surface of the annealed samples (Fig. 4(c) and (d)), which acted as a physical barrier to restrict lateral expansion and merging of localised corrosion. It may explain why the annealed samples showed greater Young's modulus and hardness than the as-deposited after eight days corrosion tests.

4.4.4 Surface and subsurface observations

Both as-deposited and annealed coatings consisted of three sublayers, namely, a nanocomposite TiSiN outer layer, a columnar-grained TiN transitional layer and a thin metallic Ti wetting layer. All these three layers, while fulfilling their mechanical functions, also acted as physical barriers against potential corrosion attack on the steel substrates. The surface of the coatings was examined before corrosion tests. Surface defects, such as micron-sized pinholes and embedded particles, were observed in both samples (Fig. 6(a) &(b)). Elemental maps, recorded using EDS, over a surface pinhole in Fig. 6(b) were also acquired. The colour pixels in these images represent the presence of the elements of interest. Notably, a high concentration of iron was detected within the pinhole, indicating that the steel substrate may be locally exposed and more likely to corrode in subsequent immersion tests. To probe the depth of a surface pinhole, a cross-section was produced across the pinhole (Fig. 6(c)). The pinhole was observed to have a depth to the thickness of the TiSiN coating. Within the pinhole, micron-sized particles can also be seen, apparently arising from the deposition process.

The sample surface was examined following two- and eight-days immersion tests (Fig. 7). For samples subjected to two days corrosion tests, the initiation of localised corrosion was observed at surface defect sites. By increasing the immersion time to eight days, pitting was observed to expand in both types of coated specimens – moving downward and corroding the less-noble steel substrate, and at the same time propagating laterally along the interface between the outer TiSiN coating and the TiN underlayer. More often, pits extended to join their neighbours and created widespread damage in the as-deposited sample, compared to a relatively isolated pitting damage in the annealed sample. Elemental maps over two pits in the annealed sample were also given after 8 days immersion tests; the steel substrate was more evident inside the pits than in the reference samples.

To clarify the effect of compressive residual stress in the coatings on the corrosion behaviour of the coated seels, the cross-sections of the coating samples were prepared after corrosion tests and the interaction between the coating microstructure and corrosion progression was examined (Fig.8). For two days immersion tests, the lateral expansion of the pits along the TiSiN/TiN interface was observed in both types of TiSiN coatings, since the TiN layer within the pits acted as a physical barrier against downward progression of corrosion. Even so, corrosion penetration through the less-densely packed boundaries between vertically aligned columnar TiN grains was evident in the annealed coating. Following eight days immersion tests, an appreciable thinning of the TiN layer was observed at the pitting sites in the as-deposited sample, presumably caused by prolonged acid attack. Neither subsurface cracks nor

delamination were noted. In contrast, the exposed TiN layer was removed in bulk at the pitting sites in the annealed sample (Fig. 9). Moreover, delamination was detected at the interface between the top TiSiN and TiN as well as the boundary between the TiN and steel substrate around these pitting sites.

4.4.5 Effect of residual stress on the corrosion resistance

Open corrosion cavities were observed in the coatings, which acted as pathways for nitric acid to penetrate through the coatings and attack the steel substrate. A FEA model was thus constructed o quantify the role of compressive residual stress in resisting the opening of the cavities in the samples. The percent reduction of lateral section area of a cavity was observed to increase rapidly with the opening (i.e. the size of end diameters, r = 50, 150 and 300 nm) of the cavity (Fig. 10). For a through-TiN coating cavity the maximum area reduction was ~3% (Fig. 10(a)), while the reduction was larger for a shallow cavity, i.e., ~ 8% (Fig. 10(b)), meaning that the residual stress was more effective in resisting the infiltration of corrosive agents at the early stage of corrosion development. Moreover, the maximum percent area reduction was noted to occur near the cavity tip, in particular for the shallow cavities, indicating the residual stress played a critical role in resisting the corrosion advance.

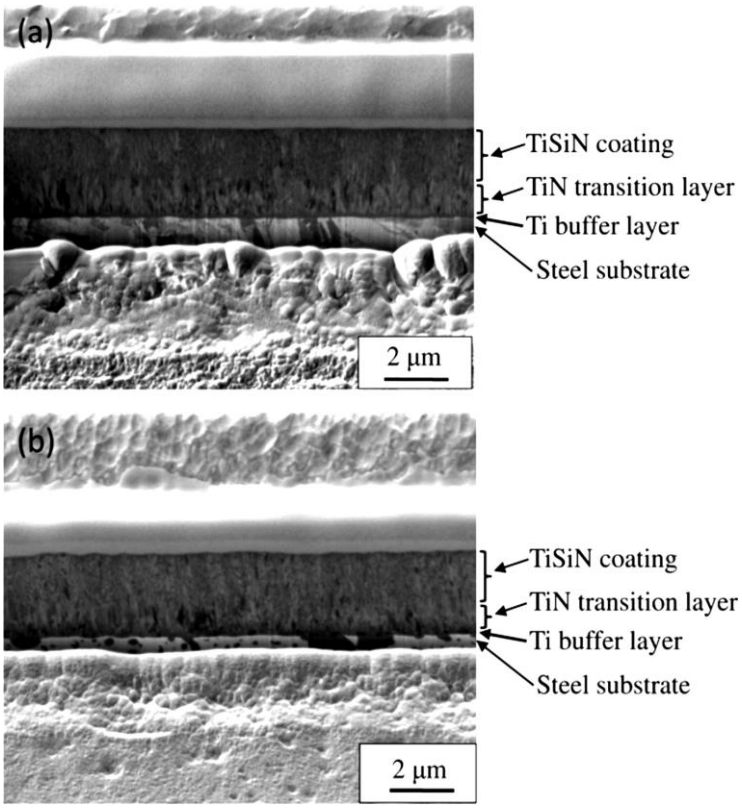

Figure 1: Secondary electron micrographs showing the microstructure of (a) as-deposited and (b) annealed TiSiN coatings on steel substrates.

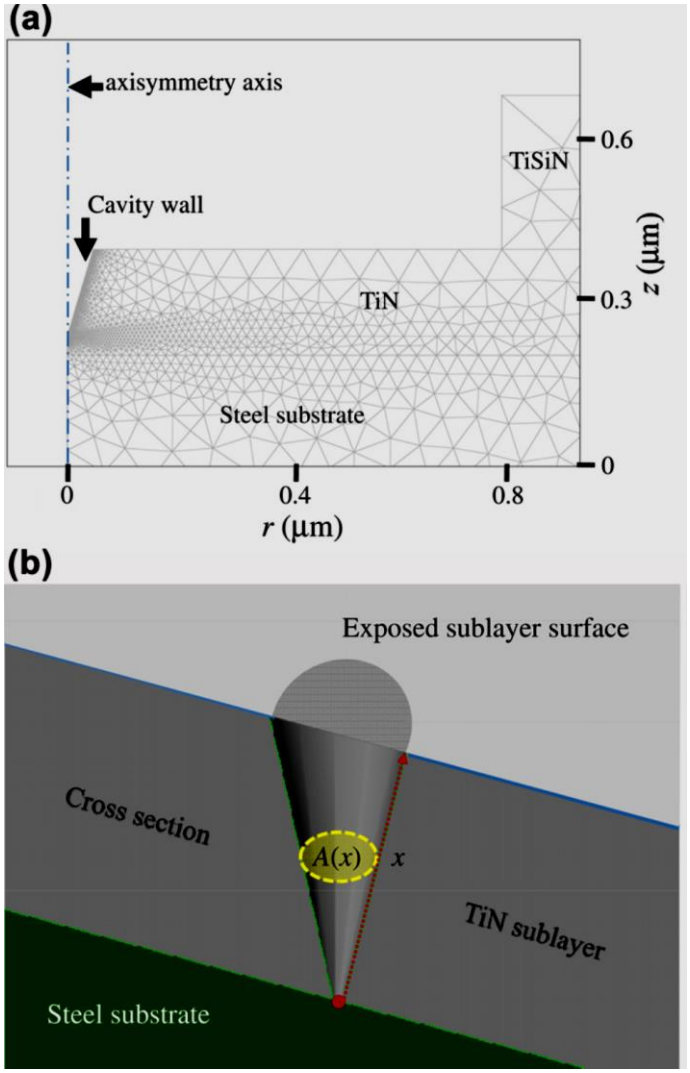

Figure 2: Role of residual stress in resisting the growth of localised corrosion in the coatings. (a) Finite element model showing a cone-shaped cavity through the thickness of the TiN sublayer. The left-hand side is the axisymmetric axis. (b) 3D cross-sectional view of the model, in which x represents the distance from the coating/substrate interface along the centreline of the cavity, and $A(x)$ is the sectional area of the cavity at the distance x.

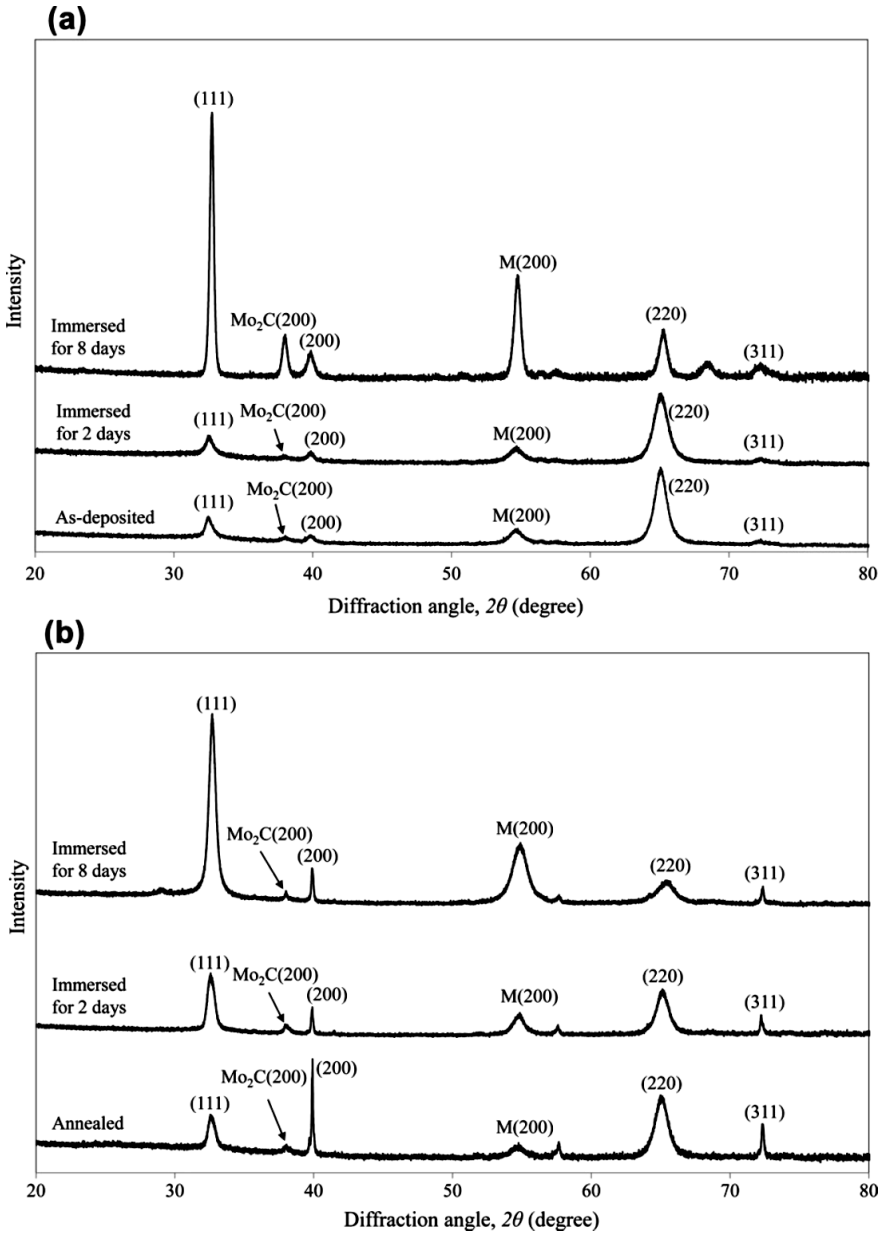

Figure 3: Grazing incidence X-ray diffraction patterns of (a) as-deposited and (b) annealed coating samples before and after immersion tests. Patterns have been offset for ease of viewing. Note that "M" represents martensite phase.

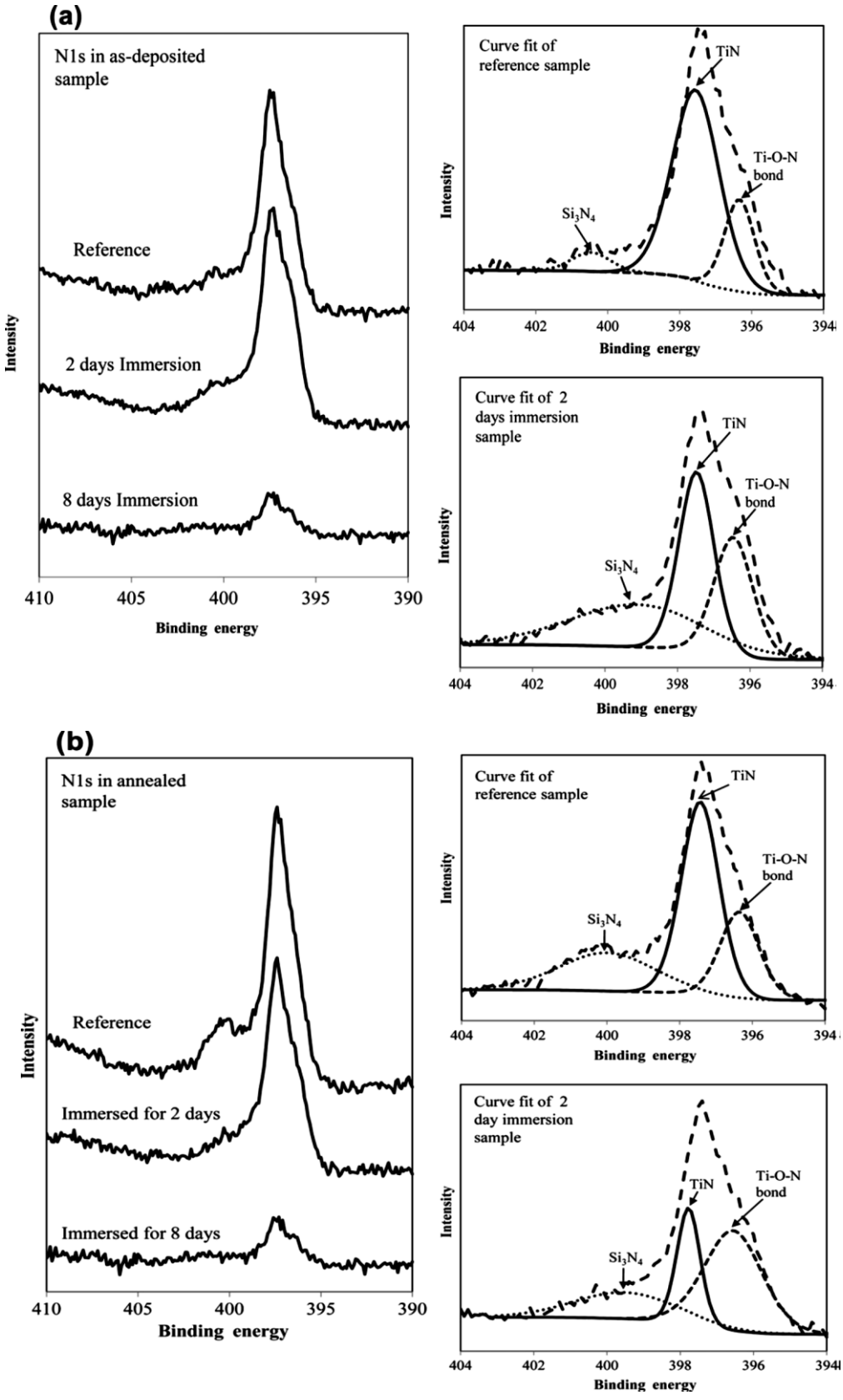
(a)
N1s in as-deposited sample
Reference
2 days Immersion
8 days Immersion
Intensity
410
405
400
395
390
Binding energy
Curve fit of reference sample
TiN
Ti-O-N bond
Si3N4
Intensity
404
402
400
398
396
Binding energy
Curve fit of 2 days immersion sample
TiN
Ti-O-N bond
Si3N4
Intensity
404
402
400
398
396
Binding energy
(b)
N1s in annealed sample
Reference
Immersed for 2 days
Immersed for 8 days
Intensity
410
405
400
395
390
Binding energy
Curve fit of reference sample
TiN
Ti-O-N bond
Si3N4
Intensity
404
402
400
398
396
Binding energy
Curve fit of 2 day immersion sample
TiN
Ti-O-N bond
Si3N4
Intensity
404
402
400
398
396
Binding energy

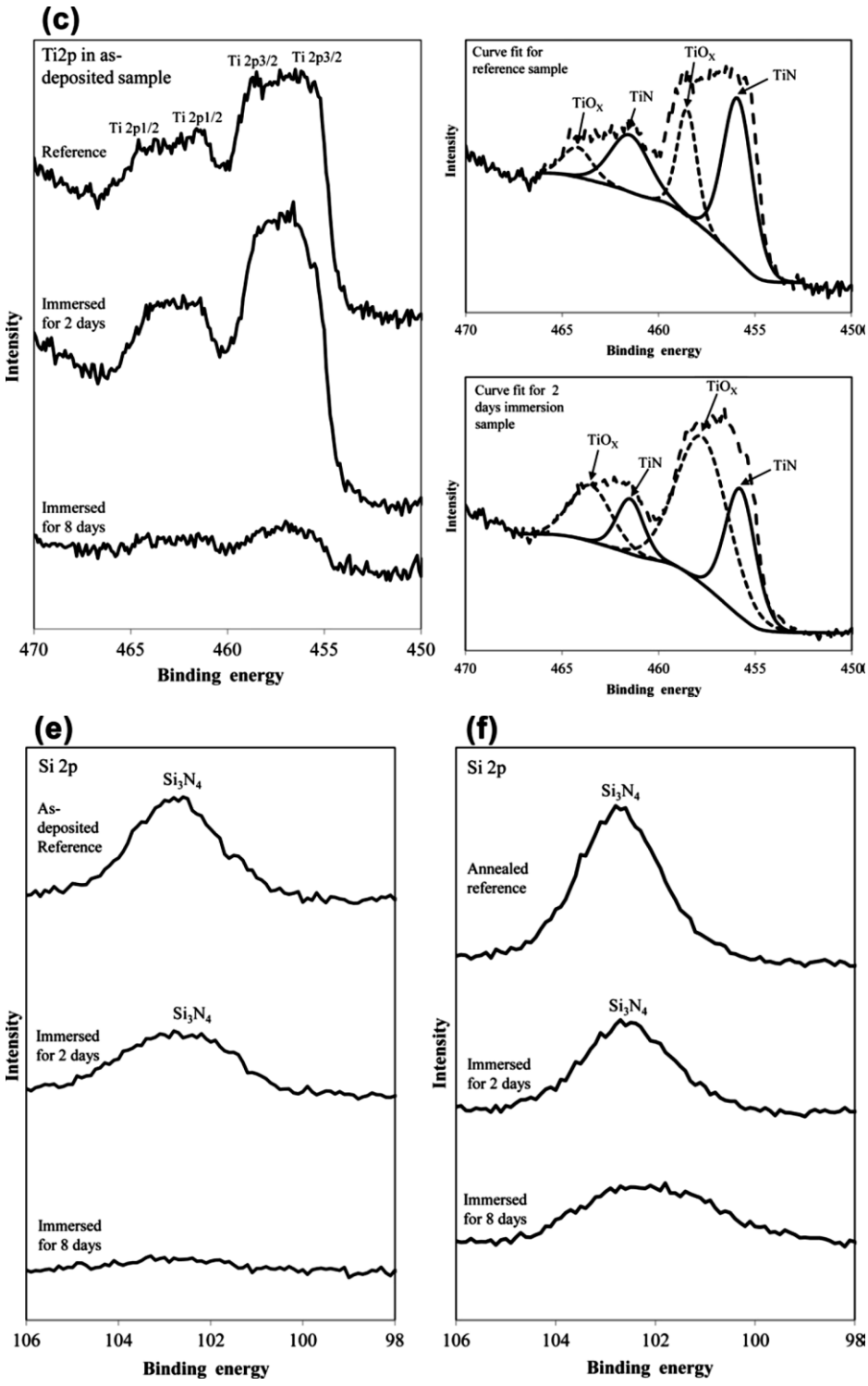

Figure 4: Surface X-ray photoelectron spectroscopy spectra for both as-deposited and annealed sample before and after immersion tests: the chemical bonding states of N 1s in (a) as-deposited and (b) annealed samples; the chemical bonding states of Ti 2p in (c) as-deposited and (d) annealed samples; the chemical bonding states of Si 2p in (e) as-deposited and (f) annealed samples.

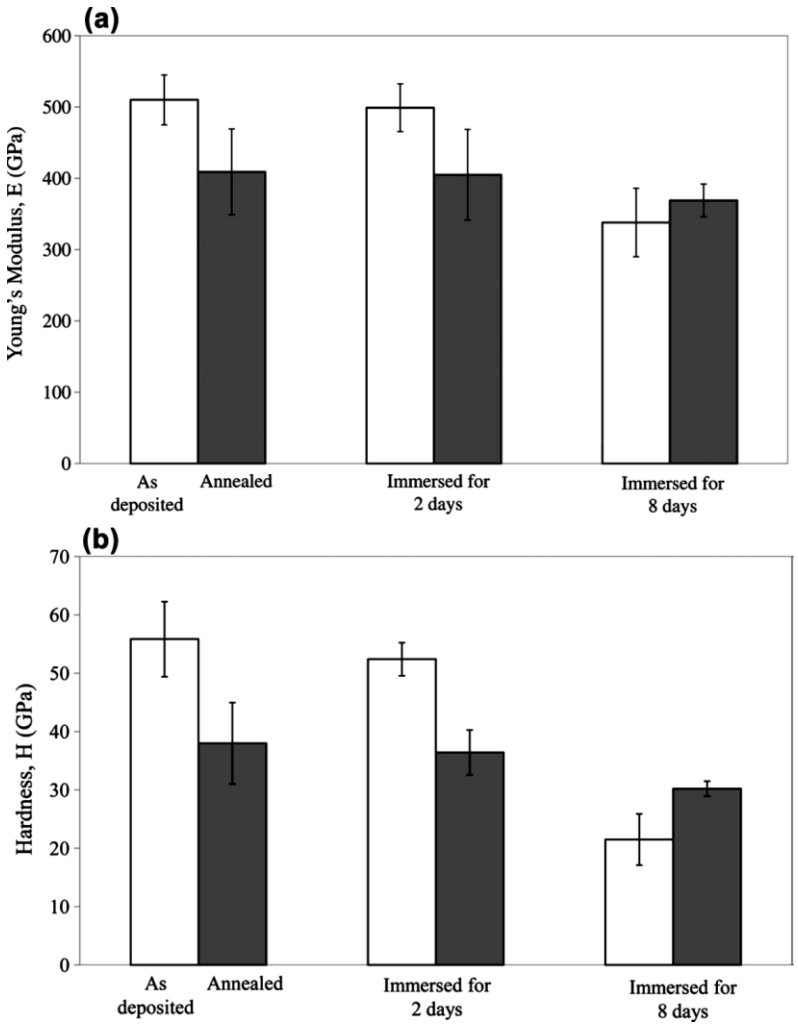

Figure 5: Variation of (a) Young's modulus and (b) hardness of both as-deposited and annealed TiSiN coatings with immersion test time.

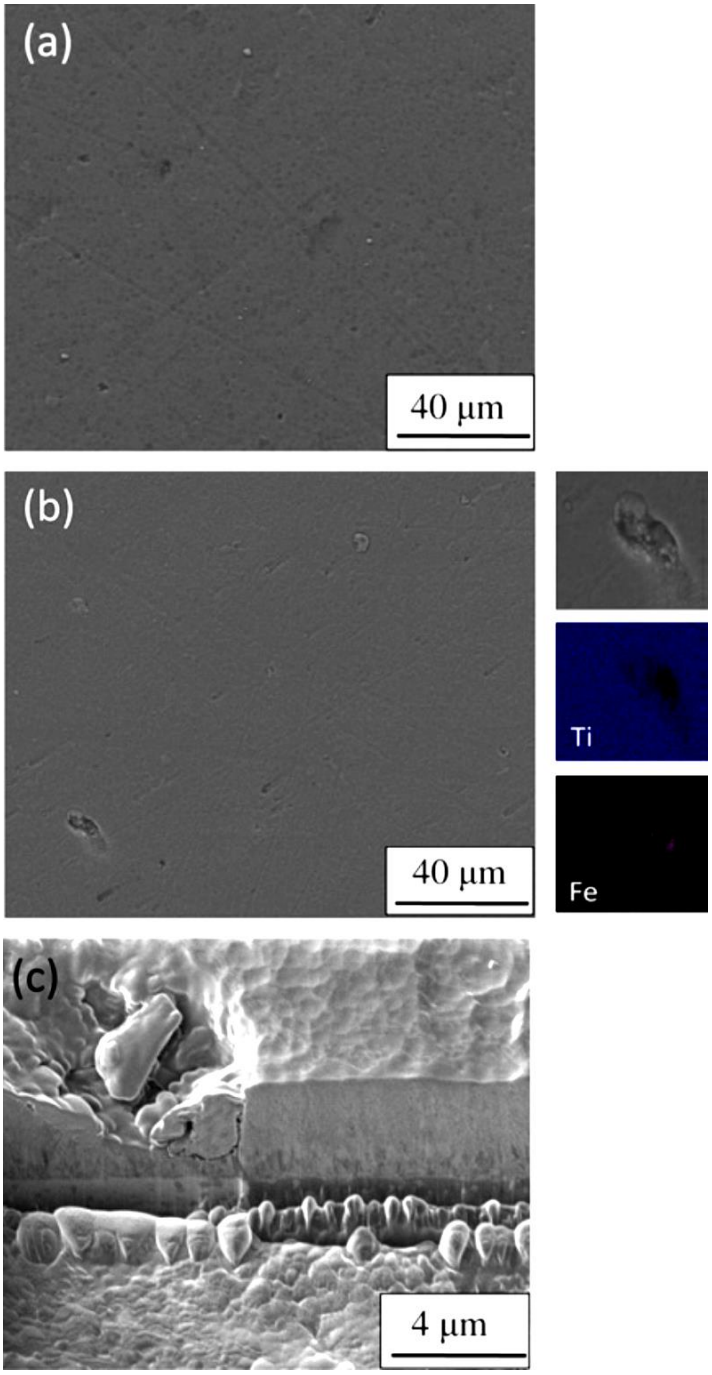

Figure 6: Scanning electron micrographs showing the surface morphology of (a) the as-deposited and (b) annealed TiSiN coatings on steel substrates before corrosion tests, and a gallium ion-induced secondary electron micrograph showing (c) the cross section of a surface defect (i.e., pinhole) in the annealed coating sample before immersion tests. Next to the surface image in (b) is an enlarged view of a surface pit and corresponding Ti and Fe elemental maps.

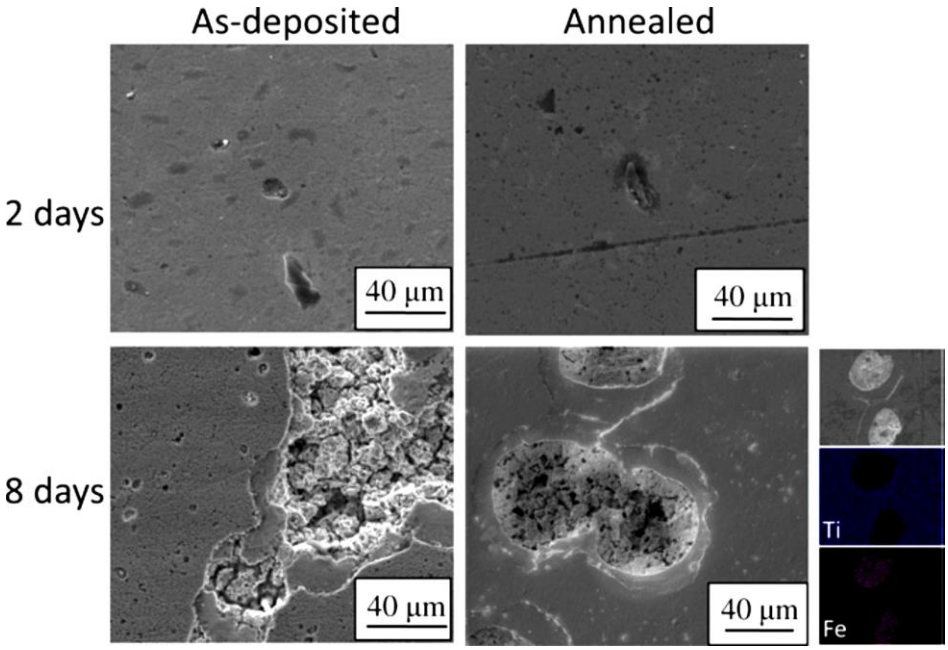

Figure 7: Scanning electron micrographs showing the surface of both as-deposited and annealed TiSiN coatings on steel substrates after corrosion tests. Next to the surface image of the annealed sample subjected to 8 days immersion test are a separate view of two separate surface pits and corresponding Ti and Fe elemental maps.

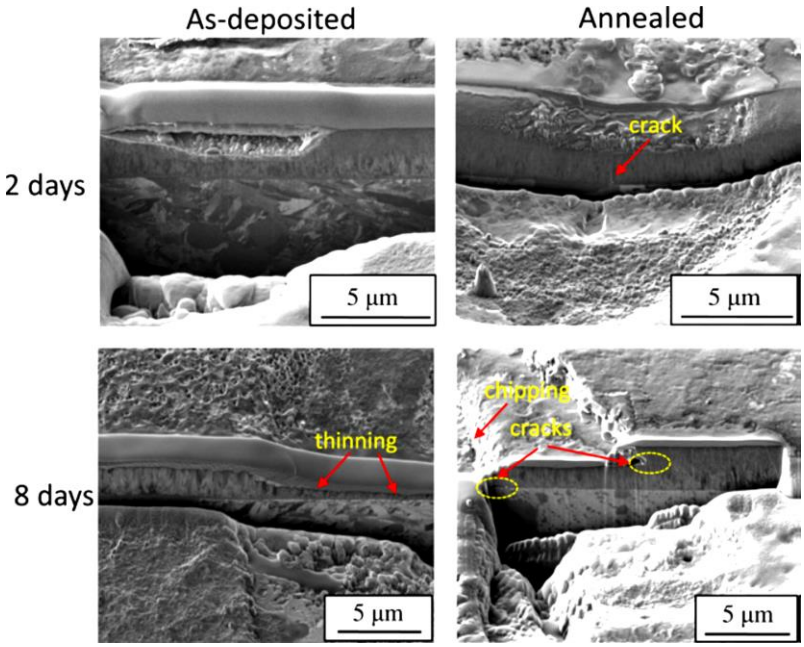

Figure 8: Secondary electron micrographs showing the progression of the corrosion in as-deposited and annealed TiSiN coatings on steel substrates. Note corrosion-induced crack propagation can be seen in the annealed samples.

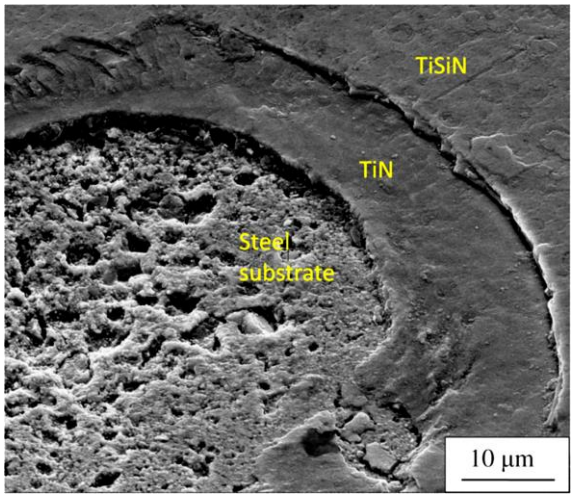

Figure 9: Scanning electron micrograph showing typical damage pattern of corrosion pitting in the annealed sample subjected to eight days immersion test. Note TiN layer in the central region is removed and the delamination of the top TiSiN layer occurs, presumably caused by corrosion cracking along the weak TiSiN/TiN interface.

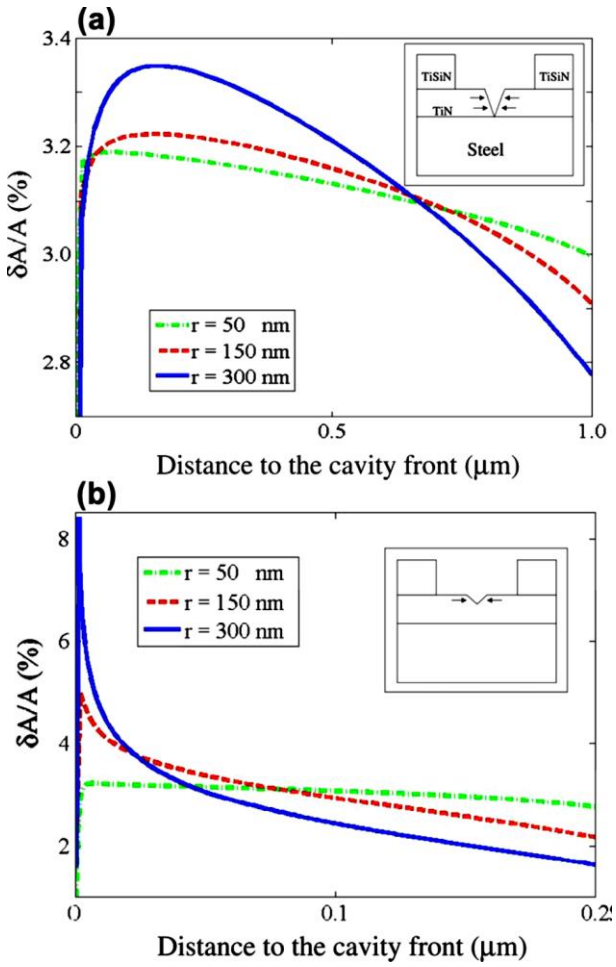

Figure 10: Percent reduction of the section area of cone-shaped cavities having different end radius (r = 50, 150, 300 nm) developed in the TiN layer of the as-deposited samples as a function of the distance to the cavity front. Inserts showing the profiles of the cavities. (a) A cavity of 1 µm depth and (b) a shallow cavity of 200 nm depth.

Table I Materials properties of substrate and coating components used in FEA simulations.

	Substrate	TiSiN	TiN	Ti
Young's modulus (GPa)	200†	510[21]	590‡	104†
Poisson's ratio	0.30†	0.20	0.25	0.34†
Residual stress, as-deposited (GPa)	-	10	3	-
Residual stress, annealed (GPa)	-	1	0.3	-
Thickness (μm)	-	1.78	1.00	0.22

†http://www.efunda.com/materials/alloys/

‡http://www.ceramics.nist.gov/srd/scd/Z00220.htm

Table II Binding energy peaks of N 1s, Ti 2p and Si 2p and corresponding phases identified by surface XPS analysis in both as-deposited and annealed samples before and after 2 days immersion tests

Sample type		Binding Energy (eV) of N 1s	Phases	Binding Energy (eV) of Ti 2p3/2	Phases	Binding Energy (eV) of Ti 2p1/2	Phases	Binding Energy (eV) of Si 2p	Phase
As-deposited	Reference	396.3 397.7 400.5	Ti-O-N TiN Si_3N_4	456 458.5	TiN TiO_x	460.8 464.3	TiN TiO_x	102.6	Si_3N_4
	2 days immersion	396.4 397.5 399.5	Ti-O-N TiN Si_3N_4	456 458	TiN TiO_x	461.2 463.8	TiN TiO_x	102.8	Si_3N_4
Annealed	Reference	396.4 397.4 400	Ti-O-N TiN Si_3N_4	455.8 458	TiN TiOx	461.5 463.8	TiN TiO_x	102.3	Si_3N_4
	2 days immersion	396.6 397.8 399.7	Ti-O-N TiN Si_3N_4	455.6 457.6	TiN TiO_x	461.3 463.5	TiN TiO_x	102.2	Si_3N_4

4.5 Conclusions

Direct subsurface observation, in combination with surface characterisation and modelling techniques, was performed to probe the corrosion evolution of TiSiN coated steels in 70% nitric acid, with a focus on the roles of surface oxide layer and compressive residual stress in controlling the development of localised corrosion. The following conclusions can be drawn:

1) Corrosion pitting was observed to be dominant in TiSiN coatings on steel substrates, which originated from surface defects such as pinholes.
2) Thin oxide layer, formed during post-deposition annealing treatment, inhibited the penetration of acidic solution through the surface of the annealed coating and provided an overall protection of the coated steels.
3) Compressive residual stress suppressed the propagation of corrosion-induced cracks through the sublayer interface and the boundaries of columnar TiN grains and caused the shrinkage of open corrosion cavities in the coatings.

Accordingly, surface oxidation treatment may be applied in conjunction with the control of compressive residual stress to provide an effective protection against localised corrosion in PVD-prepared ceramic coatings on steels.

4.6 References

1. Martínez, D.M., C.L. Cartes, C.L., Fernández, A., Sánchez-López, J.C., Influence of the microstructure on the mechanical and tribological behaviour of TiC/a-C nanocomposite coatings, Thin Solid Films, 517 (2009) 1662-1671.

2. Cheng, Y.H., Browne, T., Heckerman, B., Meletis, E.I., Mechanical and tribological properties of nanocomposite TiSiN coatings, Surface & Coatings Technolology 204 (2010) 2123-2129.

3. Zeng, Z., Zhou, Y., Zhang, B., Sun, Y.L., Zhang, J., Designed fabrication of hard Cr-Cr_2O_3-Cr_7C_3 nanocomposite coatings for anti-wear application, Acta Mater. 57 (2009) 5342-5347.

4. Lin, J., Moore, J.J., Mishra, B., Pinkas, M., Sproul, W.D., The structure and mechanical and tribological properties of TiBCN nanocomposite coatings, Acta Materialia 58 (2010) 1554-1564.

5. Ding, X.Z., Tan, A.L.K., Zeng, X.T., Wang, C., Yue, T., Sun, C.Q., Corrosion resistance of CrAlN and TiAlN coatings deposited by lateral rotating cathode arc, Thin Solid Films, 516 (2008) 5716-5720.

6. Chang, C.L., Lin, C.T., Tsai, P.C., Ho, W.Y., Liu, W.J., Wang, D.Y., Mechanical and corrosion properties of (Ti,Si)N coating synthesized by cathodic arc plasma evaporation, Surface & Coatings Technology 202 (2008) 5516-5520.

7. Li, Y.Y., Wu, F.B., Microstructure and corrosion characteristics of CrN/NiP sputtering thin films, Thin Solid Films, 518 (2010) 7527-7531.

8. Wang, Y., Tian, W., Zhang, T., Yang, Y., Microstructure, spallation and corrosion of plasma sprayed Al_2O_3-13%TiO_2 coatings, Corrosion Science 51 (2009) 2924-2931.

9. Wang, L., Northwood, D.O., Nie, X., Housden, J., Spain, E., Leyland, A., Matthews, A., Corrosion properties and contact resistance of TiN, TiAlN and CrN coatings in simulated proton exchange membrane fuel cell environments, Journal of Power Sources 195 (2010) 3814-3821.

10. Suresha, S.J., Gunda, R., Jayaram, V., Biswas, S.K., Effect of residual stress on the fracture strength of columnar TiN films, Journal of Materials Resource 22 (2007) 3501-3506.

11. Liu, Z.J., Jiang, N., Shen, Y.G., Li, X., Stress-induced surface damages in Ti–Si–N films grown by magnetron sputtering, Thin Solid Films, 516 (2008) 7609-7614.

12. T. Allen, T., J. Busby, J., M. Meyer, M., D. Pett, D., Materials challenges for nuclear systems, Materials Today, 13 (2010) 14-23.

13. Chang, C.L., Chen, W.C., Tsai, P.C., Ho, W.Y., Wang, D.Y., Characteristics and performance of TiSiN/TiAlN multilayers coating synthesized by cathodic arc plasma evaporation, Surface & Coatings Technology 202 (2007) 987-992.

14. Ying, L., Qu, L., Wang, F., The electrochemical corrosion behavior of TiN and (Ti,Al)N coatings in acid and salt solution, Corrosion Science, 45 (2003) 1367-1381.

15. Yang, Q., Cai, F., Zhao, L.R., Huang, X., Improving corrosion resistance of CrTiAlN coating by post-deposition treatments, Surface & Coatings Technolology, 203 (2008) 606–609.

16. Xie, Z. Hoffman, M., Moon, R.J., Munroe, P., Cheng, Y., Subsurface Indentation Damage and Mechanical Characterization of α-Sialon Ceramics, Journal of American Ceramic Society, 87 (2004) 2114-2124.

17. Xie, Z., Moon, R., Hoffman, M., Munroe, P., Cheng, Y., Microstructural Effect on Grinding and Polishing of α-Sialon Ceramics, Journal of European Ceramic Society 23 (2003) 2351-2360.

18. Xie, Z., Hoffman, M., Moon, R.J., Munroe, P., Deformation of a hard coating on ductile substrate system during nanoindentation: Role of the coating microstructure, Journal of Materials Resources, 21 (2006) 437-447.

19. Wo, P.C., Munroe, P., Zhou, Z., Li, K.Y., Xie, Z., Effects of TiN sublayers on the response of TiSiN nanocomposite coatings to nanoindentation and scratching contacts, Materials Science Engineering A 527 (2010) 4447-4457.

20. Ahmed, M.S., Zhou, Z., Munroe, P., Li, K.Y., Xie, Z., Control of the damage resistance of nanocomposite TiSiN coatings on steels: roles of residual stress, Thin Solid Films, 519 (2011) 5007-5012.

21. Ahmed, M.S., Zhou, Z., Munroe, P., Li, K.Y., Xie, Z., Tan, N.C., Effect of thermal annealing upon residual stress and mechanical properties of nanostructured TiSiN coatings on steel substrates, Journal of American Ceramic Society, 94 (2011) 1546-1551.

22. Pang, W.K., Low, I.M., O'Connor, B.H., Sun, Z.M., Prince, K.E., Oxidation characteristics of Ti_3AlC_2 over the temperature range 500–900° C, Materials Chemistry & Physics, 117 (2009) 384-389.

23. Wo, P.C., Munroe, P., Vasiliev, M., Xie, Z., Alameh, K., Kotov, V., A novel technique for microstructure characterization of garnet films, Optical Materials, 32 (2009) 315-322.

24. Oliver, W.C., Pharr, G.M., Measurement of hardness and elastic modulus by instrumented indentation: Advances in understanding and refinements to methodology, Journal of Materials Research, 19 (2004) 3-20.

25. Paleau, Y., Generation and evolution of residual stresses in physical vapour-deposited thin films, Vacuum, 61 (2001) 175-181.

26. Iordanova, I., Kelly, P.J., Mirchev, R., Antonov, V., Crystallography of magnetron sputtered TiN coatings on steel substrates, Vacuum, 81 (2007) 830-842.

27. Zhang, R.F., Veprek, S., On the spinodal nature of the phase segregation and formation of stable nanostructure in the Ti–Si–N system, Materials Science Engineering A, 424 (2006) 128-137.

28. Jiang, N., Shen, Y.G., Mai, Y.W., Chan, T., Tung, S.C., Nanocomposite Ti–Si–N films deposited by reactive unbalanced magnetron sputtering at room temperature, Materials Science Engineering B, 106 (2004) 163-171.

29. Flink, A., Beckers, M., Sjolen, J., Larsson, T., Braun, S., Karlsson, L., Hultman, L., The location and effects of Si in $(Ti_{1-x}Si_x)N_y$ thin films, Journal of Materials Research, 24 (2009) 2483-2498.

Chapter 5 Corrosion and Damage Resistant Nitride Coatings for Steel

This chapter was published as an article in the journal of American Ceramic Society, 2012, Vol. 95, pp.2997-3004. Whilst all efforts were made to retain the original features of this article, minor changes such as the layout, number formats, and font size and style were implemented in order to maintain consistency in the formatting style of the thesis.

5.1 Abstract

Ceramic coatings of distinct microstructures, namely, TiSiN and CrN, were deposited onto tool steels. The corrosion resistance of the coated steels was measured. Following nanoindentation, immersion tests were conducted in 70% HNO_3 solution for 96 hours. Deformed CrN, where deformation occurred through shear sliding of columnar grains, were insensitive to corrosion attack. In contrast, open cracks formed in the indented TiSiN coating, serving as pathway for reactive agents to penetrate through the coatings. Finite element analysis was applied to evaluate the damage tolerance of the coatings and its impact on the corrosion resistance of the coated steels.

5.2 Introduction

The corrosion of steel-based components costs ~3% of the annual world GDP [1].To combat the corrosion, ceramic coatings, among which CrN is the most common type, are often engineered, for example, onto machining tools and medical devices [2-3]. CrN coatings typically exhibit a columnar-grained structure [4-6]. The shearing of these elongated grains controlled deformation during mechanical loading [7], which prevents the formation of open, unstable cracks and averts catastrophic failure. More recently, nanocomposite TiSiN coatings have attracted considerable interest, owing to their extremely high hardness [8-10]. These coatings form a unique microstructure that consists of TiN nanocrystallites surrounded by amorphous SiN_x matrix phase [10, 11].However, brittle failure can occur in these TiSiN coatings, manifested by the formation and propagation of open cracks [12].

Structural defects, such as pores and micro-particles, are often observed in ceramic coatings. Corrosive agents may penetrate into the coatings through these defects and attack the metal substrates. Passive oxide layer was reported to form on the surface of both CrN and TiSiN coating [13, 14]. The integrity of the oxide layer is critical to amend the structural defects and restore the ability of the coated metals against corrosion. However, the nature of the oxide layer formed on both types of coatings and its role in corrosion prevention remain unclear. In addition, although damage is often seen in these coated metal parts during mechanical contact, little work has been done to clarify the effect of mechanical damage upon the corrosion resistance of the coated metal parts. Such knowledge is essential to controlling the corrosion damage of the treated metal parts and thus extending their service life.

To address these challenging issues, CrN and TiSiN coatings were engineered onto steel substrates. The surface bonding structure of the coatings was probed by X-ray photoelectron spectroscopy (XPS). Potentiodynamic polarisation measurements were conducted to determine the corrosion resistance of the coated steels. The surface morphology before and after polarisation measurements was examined by electron microscopy to allow investigation of the roles of surface oxide layers in controlling the corrosion resistance of the coatings. Furthermore, nanoindentation was conducted, in combination with immersion tests and subsurface observations, to clarify how prior mechanical damage regulated the corrosion resistance of the coated steels. Finite element analysis was also used to gain a deeper understanding of the stress distribution and damage tolerance in both coatings, and help establish a clear link between the structural integrity and the corrosion resistance of the coated steels.

5.2 Experimental procedure

5.2.1 Synthesis of TiSiN and CrN coatings on steel substrates

A TiSiN coating was deposited onto a AISI M42 tool steel substrate (HRC 65) using a close-field unbalanced magnetron sputtering system (UDP650, Teer Coatings Ltd., UK) that contains three Ti and one Si targets. The polished steel substrate (surface roughness, Ra ~30nm) was mounted on a turntable holder between the targets, and the target-to-substrate distance was 17 cm. The chamber was evacuated to a background pressure lower than 2×10^{-6}torrprior to deposition. A bias voltage of -500 V was applied to bombard the substrate for 30 minutes and remove oxides or impurities on the substrate surface. The bias voltage was then reduced to -60V and Ar/N_2 mixed gas was introduced and kept at 1.3×10^{-3}torr. A thin (~0.2μm)Ti wetting layer

was first deposited, followed by a TiN transition layer (~1 μm in thickness). The composition and microstructure of the outer TiSiN coating can be controlled by adjusting the sputtering power applied to each target. During the deposition, the substrate was rotated at a speed of 10 rpm to obtain homogenous composition through the coating. The surface temperature of the central heater (5 kW) was kept at 550 °C. The substrate temperature was measured to be~ 400 °C by infrared thermometer, since it was heated by radiation of the heater. The resultant TiSiN coatings were ~2μm in thickness and composed of ~40 at.% Ti, ~10 at.% Si and ~50 at.% N [15].

The CrN coating was also engineered onto an AISI M42 tool steel substrate using the same magnetron sputtering system. Two Cr targets having a purity of 99.5 at.% were used in the coating preparation. The substrate was rotated at a speed of 10 rpm and was biased with pulse DC at a frequency of 250 kHz. The DC current applied to the two Cr targets was set to be 4.0 A, while the nitrogen content in the coating was set at 60%, controlled by a closed-loop optical emission monitor (OEM) that regulated the flow of N_2 reactive gas via a fast-responding piezoelectric valve. The substrate temperature was measured and found to be 200°C during deposition. The processing of the CrN coating comprised of three steps: plasma ion cleaning, deposition of a Cr wetting layer (~0.2 μm), and then deposition of a CrN outer layer (~1.8 μm). The bias voltage was set to be-80 V during the deposition process.

5.2.2 Potentiodynamic polarisation measurements

A three-electrode cell was used; it included copper reference electrode, platinum auxilliary electrode and tool steel sample as the working electrode. Potentiodynamic tests were performed in both 3.5% NaCl and 0.2M HNO_3 solutions at room temperature using a bio-potentiostat module attached to an atomic force microscope (NT-MDT Integra, Moscow, Russia). The sample was partially covered by paraffin leaving the measured area exposed to the solutions. Prior to the polarization, the specimens were kept in the solution for 1 hr to establish the free corrosion potential (E_{corr}). Potentiodynamic polarization tests were conducted at a scan rate of1 mV/sec and the cycle potential range was chosen to generate the cycle current up to +5 μA. At least 30 cycles were run for each sample and recorded until significant changes were detected in the voltage vs current loop, representing the breakdown potential [16] and the onset of corrosion damage on the surface. Following the electrochemical measurements a Tafel plot was generated for each type of sample. The corrosion potential (E_{corr}) and corrosion current density (i_{corr}) were then deduced from the Tafel plot (i.e., log i versus E plot). The corrosion current density was determined according to the Stern–Geary equation [17]:

$$\boldsymbol{i_{corr}} = [\frac{\boldsymbol{b_a b_c}}{\boldsymbol{2.303(b_a + b_c)}} \frac{\boldsymbol{1}}{\boldsymbol{R_P}}] \quad 1)$$

where b_a and b_c are the anodic and cathodic Tafel slopes measured from the log i versus E plots (not shown here), respectively, expressed in V/decade (V/dec) and R_p is the polarization resistance expressed in kΩ-cm^2. The polarization resistance was calculated using the following equation [18]:

$$\boldsymbol{R_P} = (\frac{\boldsymbol{\Delta E}}{\boldsymbol{\Delta i}})|\boldsymbol{\Delta E \rightarrow 0} \quad 2)$$

where ΔE and Δi is the polarization potential and the polarization current, respectively. In addition, both the reference and tested samples were examined by field emission scanning electron microscopy (FESEM) to investigate corrosion mechanism.

5.2.3 Immersion tests

The steel and coated samples were covered by acrylic nail polish (without metallic flakes), leaving an exposed area of~30 mm^{2}ineach sample for immersion tests. The test was performed in 70% HNO_3 solution at 25°C. The immersion period was set to be 96 hrs. In order to observe the effect of mechanical damage on the corrosion behaviour of the coated steels, a nanoindentation workstation (Ultra-Micro Indentation System 2000, CSIRO, Australia) was used, equipped with a spherical indenter of 5 μm in radius, to induce damage into the coating at a maximum load of 500 mN. Immersion tests of the indented samples were then carried out on the indented samples according to the procedure described above.

5.2.4 Surface chemistry of the coatings

The surface chemical bonding structure of both the reference and corroded samples from the immersion tests were identified by X-ray photoelectron spectroscopy (Kratos Axis Ultra XPS spectrometer, Manchester, UK) with MgKα radiation (hv = 1253.6 eV). The sample was mounted horizontally on holder and normal to the entrance of electrostatic lens. The base pressure of the analyser chamber was less than ~10^{-9}Torr. The voltage and emission current of X-ray source were kept at 12 kV and 12 mA, respectively. The pass energy was set to be 80 eV for the survey scan and 10 eV for the features of interests (i.e., N1s, Ti2p, Si2p, O1s and Cr2p) to ensure high resolution and good sensitivity. The energy scale of XPS spectrometer was calibrated using Cu2p (932.67 eV), Ag3d (368.27 eV), C1s of hydrocarbon (284.6 eV) and

Au4f (83.98 eV). The electrostatic lens and analyser entrance were set to Hybrid and Slot mode (Iris = 0.6 and Aperture = 49), respectively. A charge neutraliser was used during the XPS analysis.

5.2.5 Surface and subsurface observation

The indented surfaces of both the reference samples and corroded samples from the immersion tests were examined using a field emission scanning electron microscope (FESEM) (Model Fei Nova 230, FEI Company, USA). Cross-sectioning and subsurface imaging of samples was carried out using a focused ion beam (FIB) microscope (FEI xP200 FEI Company, USA). The procedure was described in detail elsewhere [19]. First, gallium ion beams were used at high current (7,000 pA) to mill through the surface area of interest and create a wedge-like trench. The resultant rough cross-section was then polished at medium currents (1,000–3,000 pA) to remove particle deposition and smooth the section. Finally, the cross-section was imaged at lower beam currents.

A cross-sectional transmission electron microscope (TEM) specimen was also prepared from the as-deposited CrN coating using the same FIB system. The process can be described as follows: a layer of platinum (1 μm thick) was deposited onto the surface area to protect the surface from milling processes. A "rough" mill was conducted with a beam current of 10,000 pA to obtain a section of~3 μm in thickness. A number of" fine" mills were then performed at reduced currents (5,000 to1,000 pA) to thin the section to ~1 μm. Final mills were carried out at further reduced currents (300 to100 pA), reducing the thickness of already thinned section down to ~100 nm. A field emission gun transmission electron microscope was used to examine the specimen (Philips CM200, Eindhoven, The Netherlands).

5.2.6 Finite element analysis

A two-dimensional axisymmetric model, with the axial coordinate being the loading direction (Fig.1), was constructed using COMSOL software (v3.5a, Comsol AB, USA). To simplify the analysis, only TiSiN and CrN coatings each 2 μm in thickness were modelled, which allowed the focus to be the effect of microstructure on the stress distribution in the coatings. The model consisted of a rectangle having dimensions of 50 × 50 μm (Fig. 1), loaded by a spherical indenter with a radius of 5 μm. The rectangle comprised a coating of 2 μm in thickness and a steel substrate of 48 μm in thickness. A refined mesh was applied within an area

of 10 × 10 μm directly beneath the indenter for high accuracy around the indenter sample contact (Insert in Fig. 1). The total number of elements was 29755, beyond which improvement in precision was insignificant. Time-dependent behaviour, such as creep, as well as surface roughness and contamination were not considered in the simulations. The contact between the indenter and the sample was assumed to be frictionless. The coating was assumed to be bonded perfectly to the elastic-plastic substrate. The TiSiN coating was treated as an isotropic elastic material. In comparison, the CrN coating exhibited a columnar-grained microstructure, in which inter-columnar shear sliding can occur under mechanical loading. As such, the CrN coating was modelled as an anisotropic elastic-plastic material with vertical shear strength defined to enable the shear sliding in this coating. The mechanical properties of the coatings, the substrate and the indenter are listed in Table I.

The boundary conditions are also illustrated in Fig. 1.The bottom (z = 50 μm) was fixed in the z direction while the right edge of the block (x = 50 μm) was not allowed to move in the x direction. For the 3D modelling, the axisymmetric axis was positioned along the left edge of the simulation block (x = 0). The tip of the indenter was positioned at z = 0 μm before the simulation. Indentation was simulated as a downward displacement to a maximum depth of 0.5 μm at an interval of 0.1 μm.

5.3 Results and discussion

5.3.1 Microstructural observation

The cross-sectional microstructure of both TiSiN and CrN coatings were revealed by FIB (Fig.2). For the TiSiN coating, both a TiN transition layer of ~1 μm in thickness and a thin Ti wetting layer of ~0.2 μm in thickness were visible beneath the TiSiN coating [15]. These interlayers were introduced to improve the adhesion of the TiSiN coatings on the steel substrate. TiSiN containing around 10% Si consisted of nanometer-sized TiN grains embedded in Si_3N_4 matrix [12].For the CrN coating, a densely packed columnar grain structure was observed. Figure 3 shows that the grains in the CrN layer are typically 100-200 nm in length and 10-20 nm in width, presumably resulting from the enhanced ion transfer during deposition [20]. This is similar to observations by Ehiasarian [21] and Olaya [6]. A Cr wetting layer can be seen underneath the CrN coating.

5.3.2 X-Ray photoelectron spectroscopy analysis

The surface bonding states of the reference samples were identified by XPS. The N1s spectra of the TiSiN sample contained two peaks at ~396.4eV and ~397.7eVcorresponding to SiN_x and TiN, respectively [10, 11]; the smaller peak at ~400 eV represented Ti-O-N phase (Fig. 4(a)). Similarly, the N 1s spectra of CrN consisted of two peaks at ~397.5 eV and ~400.2 eV originating from the CrN and Cr-O-N phases, respectively (Fig. 4(b)). The appearance of both Ti–O–N and Cr-O-N phases in these coatings might be attributed to surface oxidation [22, 23]. From the Ti2p spectra of the TiSiN sample, two pairs of peaks of Ti2p3/2 and Ti2p1/2were identified, corresponding to TiN and TiO_x phases, respectively (Fig. 4(c)). It was noted that the peak intensity of TiN was stronger than that of TiOx in the surface region, suggesting that the passive TiOx film may not cover the surface completely. From the Cr 2p spectra of the CrN sample, two pairs of peaks of Cr 2p3/2 and Cr 2p1/2, respectively, were identified, representing CrN and Cr_2O_3 phases in of the CrN sample (Fig.4(d)).Notably,Cr_2O_3 was the dominant phase, compared to CrN.

5.3.3 Electrochemical measurements

The corrosion current density, potential and polarization resistance of the tool steels with, and without, TiSiN and CrN coatings were derived from the polarisation measurements for both 3.5 wt% NaCl and 0.2M HNO_3 solutions (Table II).The potentiodynamic polarization curves for uncoated and coated (CrN and TiSiN) tool steel samples in 3.5% NaCl and 0.2M HNO_3 solutions are shown in Fig 5a and Fig 5b, respectively. Experiments showed that the corrosion resistance of the tool steels was greatly enhanced by the coatings. For the uncoated steel the corrosion current density was 527 and 597 $\mu A/cm^2$ in 3.5% NaCl and 0.2M HNO_3 solutions, respectively, which decreased down to about 220.8and 223.5$\mu A/cm^2$ for CrN coating in the same solutions. The corrosion potential, $\boldsymbol{E_{corr}}$ of the coated samples, when compared to the steel sample, shifted towards higher values (−0.1 vs copper to −0.038 V vs copper for CrN, for example), indicating a marked increase in the corrosion resistance of the CrN coated steel. Moreover, the CrN coated steel exhibited a greater polarization resistance, R_p in both salt and acidic media (higher), compared with the steel protected by TiSiN, presumably due to the fact that CrN has the ability to form amore uniform passive oxide layer over the surface [18].

For the uncoated steel sample, widespread intergranular corrosion was observed after electrochemical testing in both solutions (Fig. 6(a-c).According to XPS analysis (Fig. 4(c) &(d)), Cr_2O_3 was dominant on the CrN coating surface, and can effectively seal corrosion pathways

(i.e., structural defects) and thus imparting to the coating a greater corrosion resistance. According to the observation of structural defects in the coatings [24] and XPS data, a model was proposed to elucidate the role of the oxide layer in amending surface defects and restoring the structural integrity (Fig.7). This helps explain the difference in electrochemical measurements between TiSiN- and CrN-coated steels.

5.3.4 Effect of mechanical damage on corrosion resistance

The surface and subsurface structures of the indents was investigated with assistance of a FIB microscope to generate localised cross-sections for both the reference and corroded samples before (Fig. 8) and after immersion tests (Fig.9). For the reference TiSiN sample, intensive cracks were observed in the form of ring and lateral cracks (Fig. 8(a)&(b)). Ring cracks apparently initiated near the surface and propagated into the coating. Following the immersion test severe surface and subsurface corrosion damage was observed, presumably caused by the penetration of corrosive agents through the open crack networks in the TiSiN coating into the substrate (Fig. 8(c)&(d)). By comparison for the CrN sample, the shear sliding occurred between the vertically aligned columnar grains in the coatings under indentation loading (Fig. 9(a) and (b)). No open cracks appeared and the structural integrity was maintained. Consequently, no corrosion damage occurred at the indented sites in the CrN coated steel (Fig. 9(c) and (d)).

The experimental results demonstrated that both the presence of a surface oxide layer and the deformation mode played significant roles in controlling the corrosion damage of ceramic coatings on steels. Structural defects, such as pinholes and micro-sized particles, are often found at the surface of ceramic coatings prepared by magnetron sputtering technique [25, 26]. These defects tend to serve as the pathway for corrosive agents to penetrate through the coatings and attack the less noble substrates. The oxide layer formed on the surface of CrN coatings effectively isolated such defects from the corrosive agents, enabling a greater resistance to corrosion. On the other hand, mechanical contact induced deformation commonly occurs at the surface of coated components such as cutting tools and bio-implants during operation. The ability to maintain structural integrity of the coatings is therefore critical to the corrosion resistance of coated parts under mechanical loading. Through the shear sliding of columnar grains, the open cracks were avoided in the CrN coatings, preventing the steel substrates from corrosion damage (Fig. 10(a)). In contrast, open cracks occurred extensively in the TiSiN coatings. These cracks formed a passage for corrosive agents to move through the coatings, leading to severe corrosion damage in the substrates (Fig. 10(b)).

5.3.5 Finite element analysis

From the experimental observations, the structural integrity of the coatings is not only essential to their damage tolerance, but also underpins their corrosion resistance in harsh environments where mechanical loading is also present. To develop a better understanding of the effect of microstructure upon the damage pattern (i.e., potential corrosion pathway) in the coatings, finite element analysis was carried out to visualise the stress fields developed in the coatings during indentation and correlate the observed cracks in both TiSiN and CrN coatings with stress concentrations in them,

The in-plane shear stress distribution in the TiSiN coating changes with increasing indentation depth (Fig. 11(a)-(d)). The maximum the shear stress was located in the coating directly below the indenter at the lower indentation depths. With the increase of the indentation depth the maximum stress was 'pushed' outwards. Notably, at the indentation depth of 0.2 μm the shear stress exceeded the critical value (i.e., 8.4 GPa), which is equal to $\sigma_y/2$, where σ_y is the critical tensile stress estimated as one third of the coating hardness [25]. In comparison, the maximum tensile stress occurred at the contact edge of the coating but was lower than the critical tensile stress. Hence, the shear stress concentration was assumed to be the major cause of crack formation. Interestingly, the region where the maximum shear stress appeared (Fig. 11(d))correlated with the cracks observed at the upper part of the coating (Fig. 8(b)), indicating that the shear stress concentration was indeed responsible for the origin of the crack. When the indentation depth further increased to 0.5 μm, the aforementioned trends continued (Fig. 12(a)). Moreover, the direction of the principal stresses was identified, which tended to open up the cracks initiated by the shear stress. In contrast, under the same loading condition the in-plane shear stress within the CrN coating was substantially lower (Fig.12(b)) due to the shear deformation. As such, the probability of the initiation and propagation of open cracks would be lower, which helps maintain the structural integrity, making the deformed CrN coating insensitive to the corrosion attack.

While the evidence supports the modeling analysis that the formation of damage tolerant structure are critical to the corrosion resistance of the CrN coating, some means of comparison to corrosion in realistic environments for many years is still needed to claim its insensitivity to long-term corrosion attack.

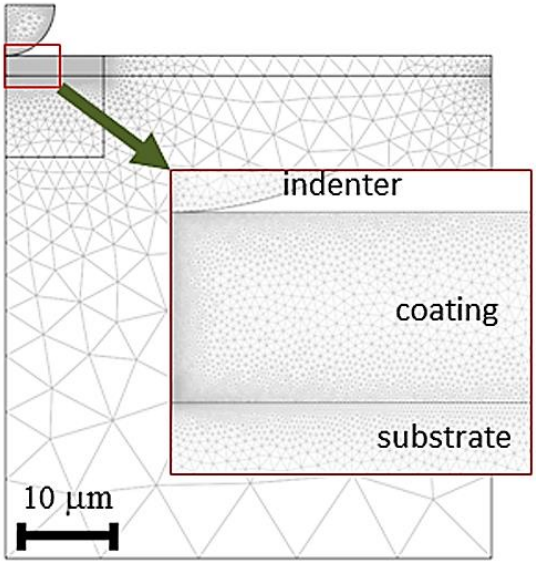

Figure 1: FEA model showing a spherical indenter (5 μm in radius) in contact with a ceramic coating (2 μm in thickness) on a steel substrate. Triangle mesh elements are used and refined around the contact region for high accuracy in stress visualisation.

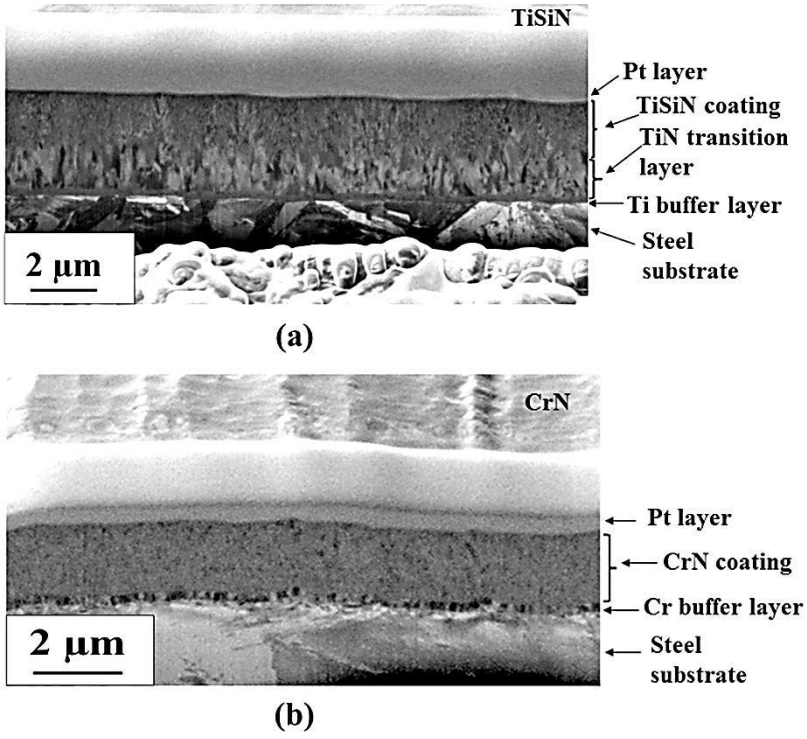

Figure 2: Cross-sectional FIB images of a) the TiSiN coating and b) the CrN coating.

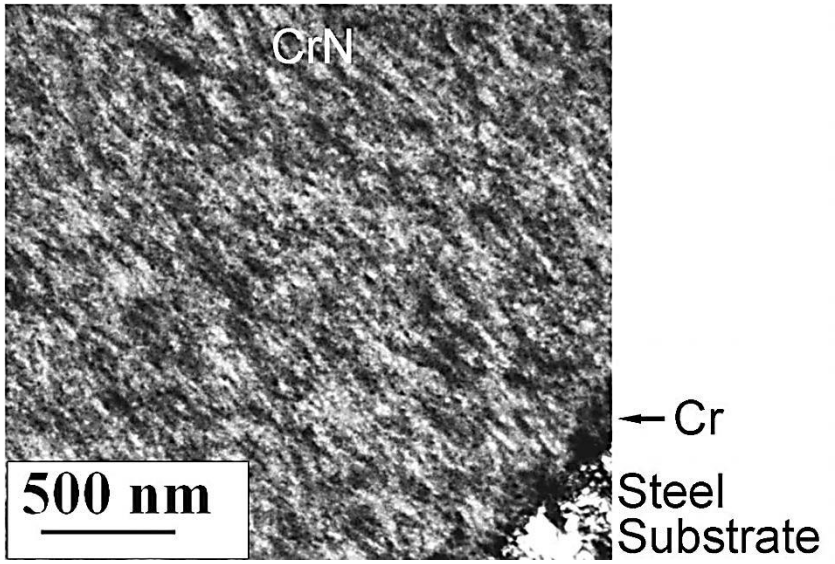

Figure 3: Bright field cross-sectional transmission electron microscope image of the CrN coating.

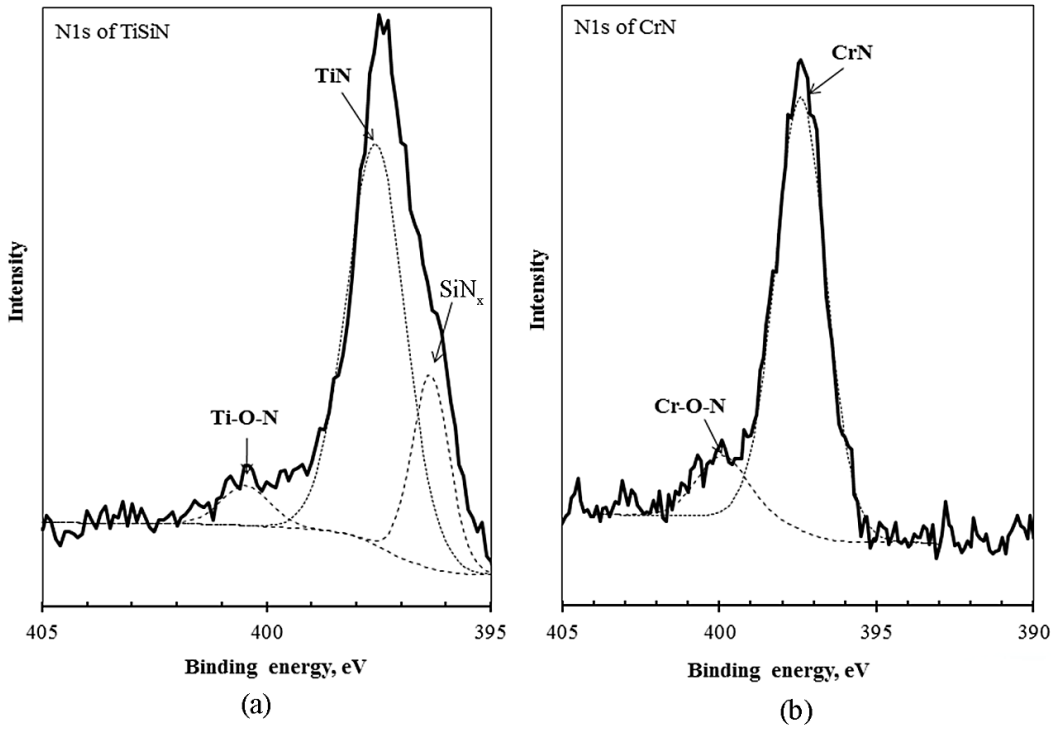

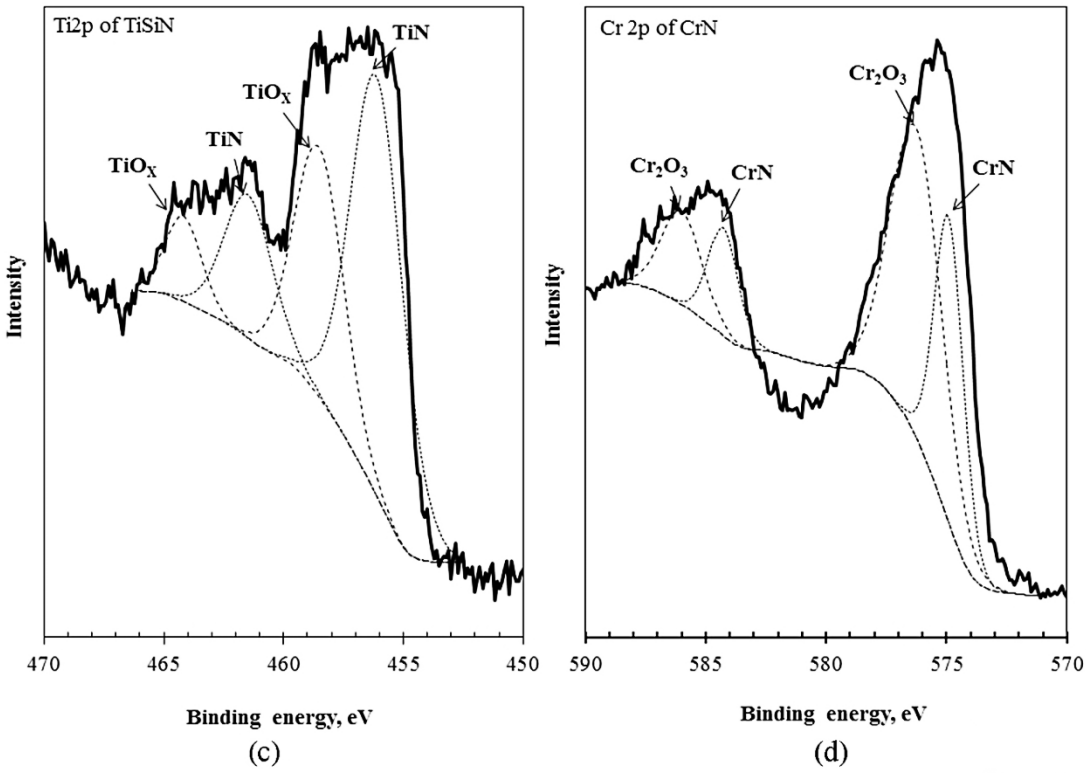

Figure 4: Surface X-ray photoelectron spectroscopy spectra for both as-deposited TiSiN and CrN sample before the immersion test: the chemical bonding states of N 1s in (a) TiSiN and (b) CrN samples; the chemical bonding states of Ti 2p in (c) TiSiNand Cr 2p and (d) CrN samples.

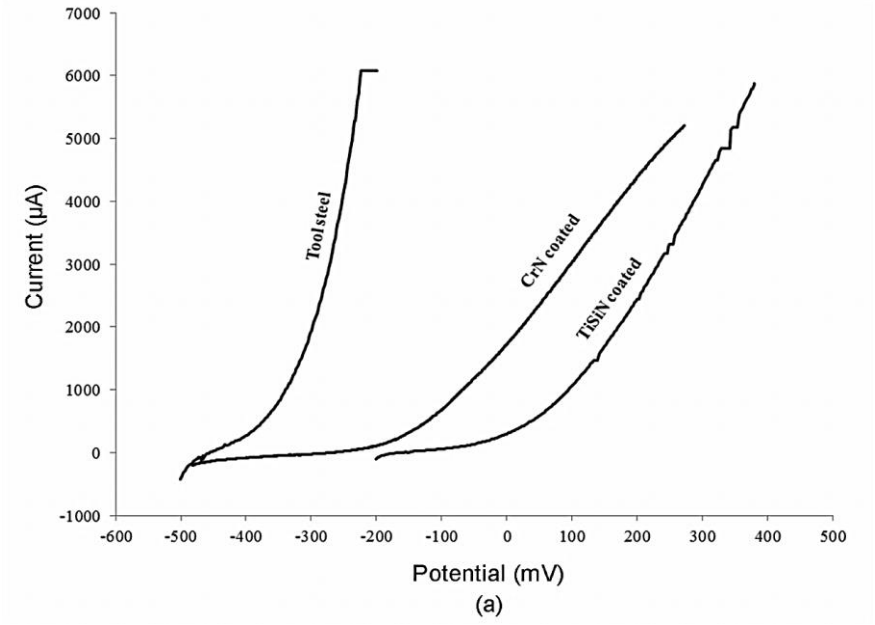

Figure 5(a): Potentiodynamic polarization curves for tool steel, TiSiN coated and CrN coated samples in 3.5 wt % NaCl solution.

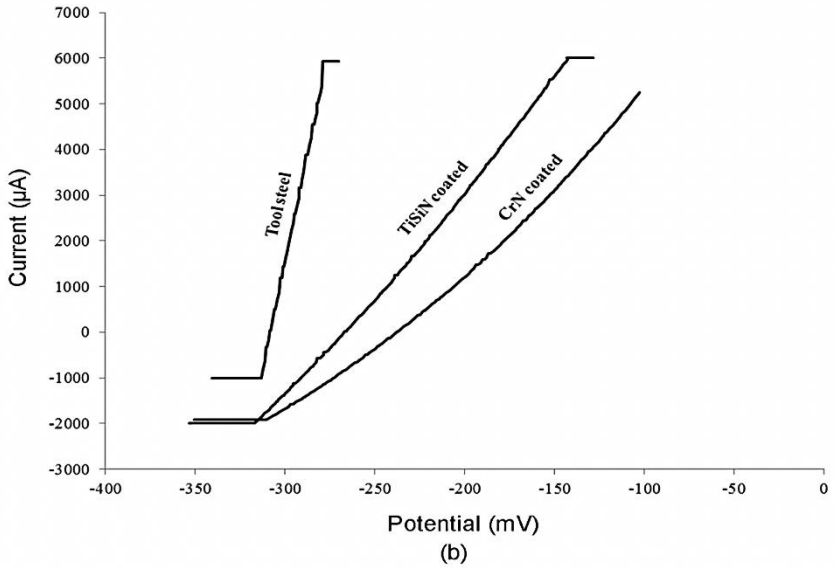

Figure 5(b): Potentiodynamic polarization curves for tool steel, TiSiN coated and CrN coated samples in 0.2M HNO_3 acid solution.

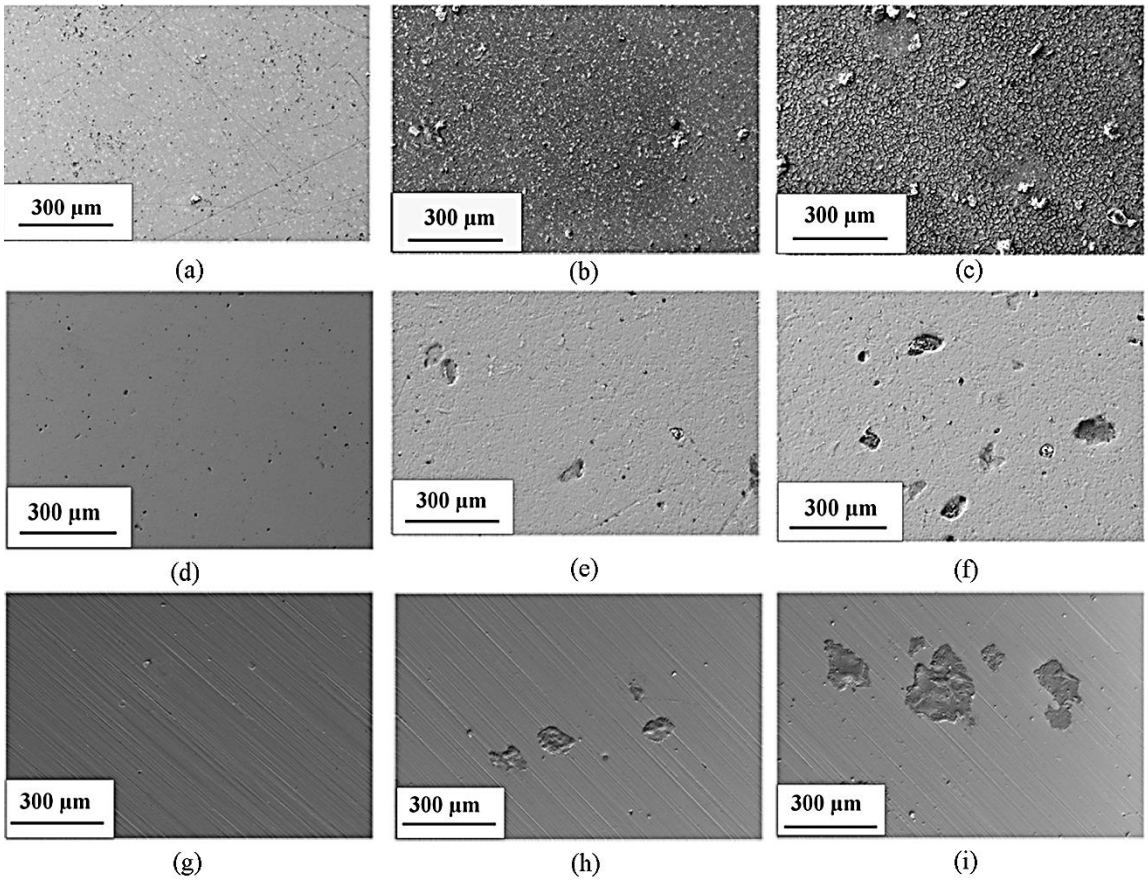

Figure 6: SEM images of (a) the tool steel reference sample, (b) the tool steel sample immersed in 3.5 wt% NaCl electrolyte, (c) the tool steel sample immersed in 0.2M HNO_3 electrolyte; (d) the TiSiN coating reference sample, (e) the TiSiN coating sample immersed in 3.5 wt% NaCl electrolyte, (f) the TiSiN coating sample immersed in 0.2M HNO_3 electrolyte; (g) the CrN coating reference sample, (h) the CrN coating sample immersed in 3.5 wt% NaCl electrolyte and (i) the CrN coating sample immersed in 0.2M HNO_3 electrolyte.

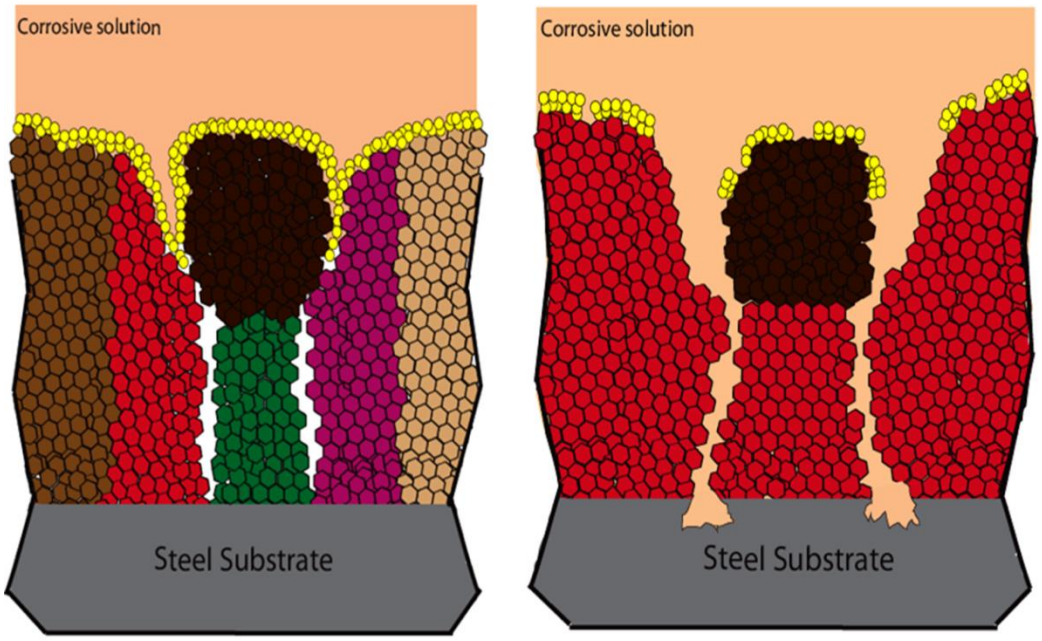

Figure 7: Schematic illustrations of micro-sized pores (structural defects) in (a) CrN and (b) TiSiN coated steels immersed in a corrosive solution. Micro-sized particles also exist in both types of coatings, in this case, sitting in the middle of pore regions. The oxide layer dominant on the surface of CrN coating shows a greater integrity than that of TiSiN, preventing the corrosive agents from penetrating through the coating.

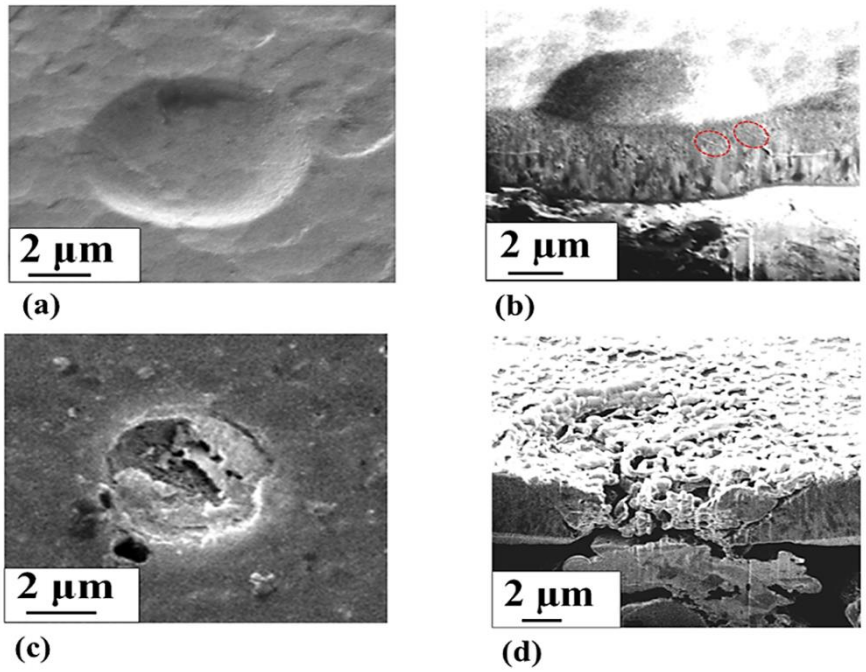

Figure 8: FIB induced secondary electron images of the indented surface and sub-surface of the TiSiN coated steel a) and b) before and c) and d) after the immersion test.

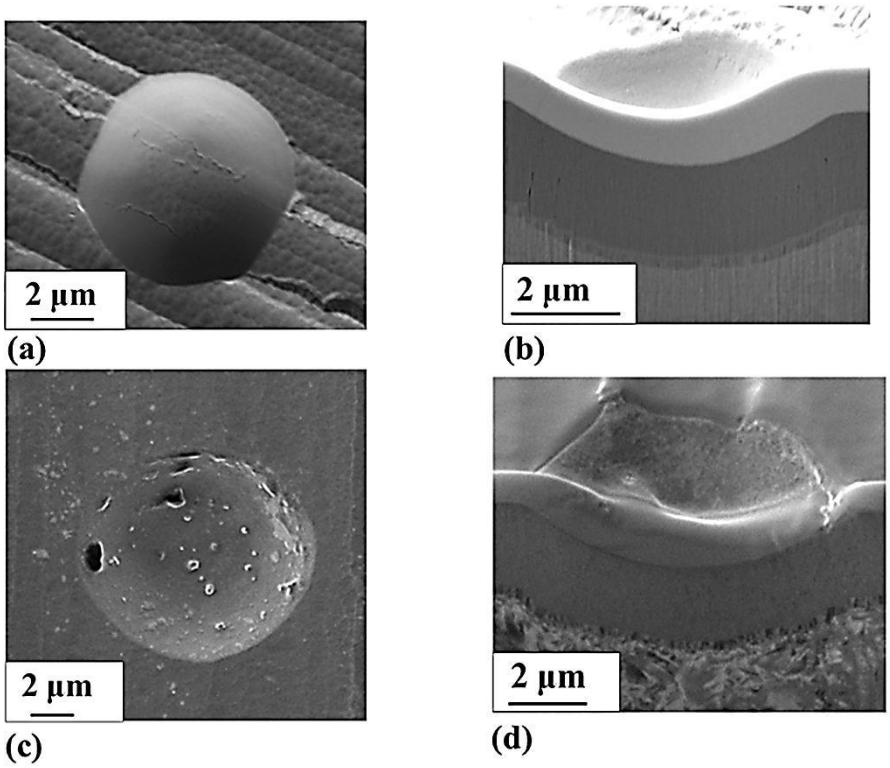

Figure 9: FIB induced secondary electron images of the indented surface and sub-surface of the CrN coated steel a) and b) before and c) and d) after the immersion test.

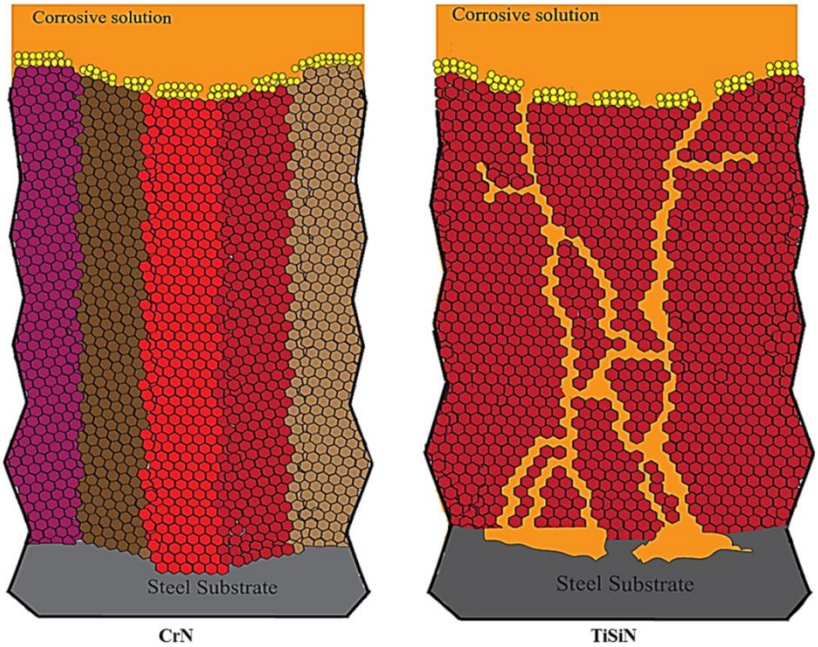

(a) (b)

Figure 10: Schematic representation of (a) deformed CrN and (b) damaged TiSiN coatings on steels immersed in corrosive solutions.

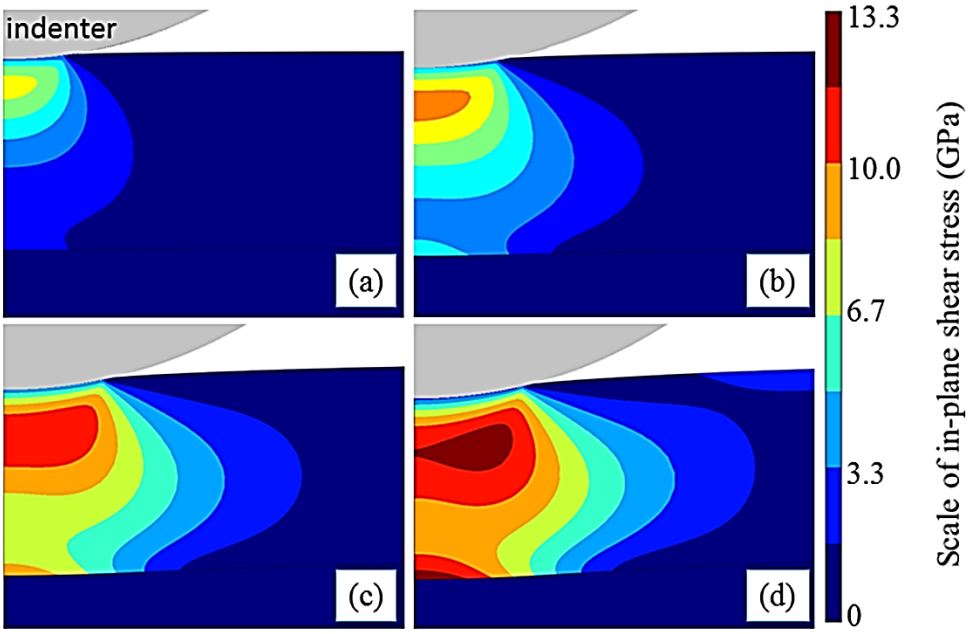

Figure 11: The distribution of in-plane shear stress within the TiSiN coating of 2 μm in thickness induced by a spherical indenter having a radius of 5 μm at (a) 0.1 μm depth, (b) 0.2 μm depth, (c) 0.3 μm depth, and (d) 0.4 μm depth

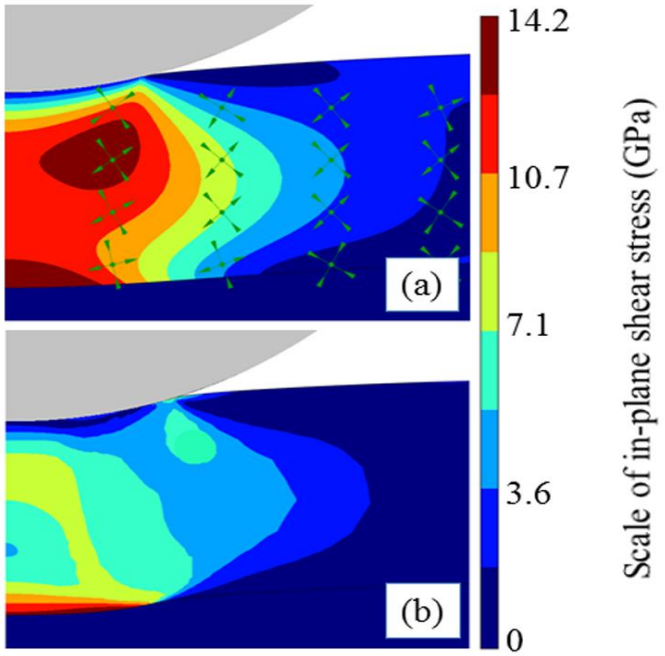

Figure 12: The distribution of in-plane shear stress caused by indentation at a depth of 0.5 μm in (a) the TiSiN coating and (b) the columnar-grained CrN coating. The arrows in (a) indicate the direction of principal stresses, which help open up the shear-induced cracks in the coating. In contrast, the level of in-plane shear stress was significantly reduced in (b) primarily due to the shear-sliding deformation.

Table I. Material properties of the steel substrate and coatings used in the FEM simulation

	Substrate	TiSiN	CrN
Young's modulus (GPa)	200†	510*	344.8
Poisson's ratio	0.30†	0.20	0.28
Thickness (μm)	-	2.00	2.00
Critical strength [GPa]	0.675 (yield)**	-	5 (shear)**

Data sources: †http://www.efunda.com/materials/alloys/

‡http://www.ceramics.nist.gov/srd/scd/Z00220.htm

* [15]

** [28]

Table II. Potentiodynamic polarization data of tool steels with, and without, CrN and TiSiN coatings measured in 3.5% NaCl and 0.2M HNO_3 solutions

Sample	**i_{corr} ($\mu A/cm^2$)**	**i_{corr} ($\mu A/cm^2$)**	**E_{corr} (V)**	**E_{corr} (V)**	**R_p (kΩ-cm^2)**	**R_p(kΩ-cm^2)**
	3.5 wt% NaCl	**0.2M HNO_3**	**3.5 wt% NaCl**	**0.2M HNO_3**	**3.5 wt% NaCl**	**0.2M HNO_3**
CrN on Tool steel	220.8	223.5	-0.038	-0.0058	0.178	0.029
TiSiN on tool steel	254.7	272.6	-0.049	-0.074	0.085	0.022
Tool steel	527	597	-0.100	-0.0230	0.027	0.005

5.4 Conclusions

Ceramic coatings with distinct microstructures were deposited onto steel substrates. The effect of coating surface chemistry and microstructure on the corrosion resistance of the coated steels was clarified, assisted by the XPS, FIB and FEA. The following conclusions can be drawn:

1) Chromium oxide was dominant on the surface of the CrN coatings, which helped prevent reactive agents from penetrating through the surface defects. Pitting in the coated steels was suppressed.

2)The shear deformation, enabled by the columnar structure in the CrN coatings, reduced the stress concentration and averted the formation of open cracks during mechanical loading, imparting to the coated steels a greater corrosion resistance.

3) Open cracks resulted from shear stress concentration in the TiSiN coatings during mechanical contact. These cracks acted as the pathway of corrosive agents, causing severe damage in the steel substrates.

5.5 References

1. Stierle, A., Tracking corrosion cracking, Science, 321 (2008) 349-350.

2. Cheng, Y.H., Browne, T., Heckerman, B., Meletis, E.I., Mechanical and tribological properties of nanocomposite TiSiN coatings, Surface & Coatings Technology, 204 (2010) 2123-2129.

3. Serro, A.P., Completo, C., Colaço, R., Santos, F.D., Silva, C.L.D., Cabral, J.M.S., Araujo, H., Pires, E., Saramago, B., A comparative study of titanium nitrides, TiN, TiNbN and TiCN, as coatings for biomedical applications, Surface & Coatings Technology 203 (2009) 3701–3707.

4. Greczynski, G., Jensen, J., Böhlmark, J., Hultman, L., Microstructure control of CrNx films during high power impulse magnetron sputtering, Surface & Coatings Technology, 205 (2010) 118–130.

5. Lin, J., Moore, J.J., Sproul, W.D., Mishra, B., Wu, Z., Wang, J., The structure and properties of chromium nitride coatings deposited using dc, pulsed dc and modulated pulse power magnetron sputtering, Surface & Coatings Technology, 204 (2010) 2230–2239.

6. Olaya, J.J., Rodil, S.E., Muhl, S., Sanchez, E., Comparative study of chromium nitride coatings deposited by unbalanced and balanced magnetron sputtering, Thin Solid Films, 474 (2005) 119-126.

7. Malyska, K.R., Wojtan, M.P., Wasmer, K., Hejduk, K., Michler, J., In-situ SEM indentation studies of the deformation mechanisms in TiN, CrN and TiN/CrN, Micron, 40 (2009) 22–27.

8. Chawla, V., Jayaganthan, R., Chandra, R., A study of structural and mechanical properties of sputter deposited nanocomposite Ti–Si–N thin films, Surface & Coatings Technology, 204 (2010) 1582–1589.

9. Bendavid, A., Martin, P.J., Preston, E.W., Cairney, J., Xie, Z., Hoffman, M., Deposition of nanocomposite thin films by a hybrid cathodic arc and chemical vapour technique, Surface & Coatings Technology, 201 (2006) 4139–4144 .

10. Zhang, R.F., Veprek, S., On the spinodal nature of the phase segregation and formation of stable nanostructure in the Ti-Si-N system, Materials Science Engineering A, 424 (2006) 128-137.

11. Veprek, S., Heijman, MG.J.V., Zhang, R., Chemistry, physics and fracture mechanics in search for superhard materials, and the origin of superhardness in nc-TiN/a-Si_3N_4 and related nanocomposites, Journal of Physics and Chemistry of Solids, 68 (2007) 1161–1168.

12. J.M. Cairney, J.M., M.J. Hoffman, P.R. Munroe, P., P.J. Martin, P.J., A. Bendavid, A., Deformation and fracture of Ti–Si–N nanocomposite films, Thin Solid Films, 479 (2005) 193-200.

13. Liu, C., Bi, Q., Leyland, A., Matthews, A., An electrochemical impedance spectroscopy study of the corrosion behaviour of PVD coated steels in 0.5 N NaCl aqueous solution: Part II, EIS interpretation of corrosion behaviour, Corrosion Science, 45 (2003) 1257–1273.

14. N. Jiang, N., Y.G. Shen, Y.G., Y.W. Mai, Y.W., T. Chan, T., S.C. Tung, S.C., Nanocomposite Ti–Si–N films deposited by reactive unbalanced magnetron sputtering at room temperature, Materials Science Engineering B, 106 (2004) 163–171.

15. Ahmed, M.S., Zhou, Z., Munroe, P., Li, K.Y., Xie, Z., Tan, N.C., Effect of thermal annealing upon residual stress and mechanical properties of nanostructured TiSiN coatings on steel substrates, Journal of American Ceramic Society, 94 (2011) 1546–1551.

16. Liu, X.M., Wu, S.L., Chu, P.K., Chung, C.Y., Chu, C.L., Chan, Y.L., Yeung, K.W.K., Lub, W.W., Cheung, K.M.C., Luk, K.D.K., In vitro corrosion behavior of TiN layer produced on orthopedic nickel– titanium shape memory alloy by nitrogen plasma immersion ion implantation using different frequencies, Surface & Coatings Technology, 202 (2208) 2463–2466.

17. Scully, J.R., Polarization Resistance Method for Determination of Instantaneous Corrosion Rates, Corrosion, 56 (2000) 199-218.

18. Grips, V,K,W., Barshilia, H.C., Selvi, V.E., Kalavati, Rajam, K.S., Electrochemical behavior of single layer CrN, TiN, TiAlN coatings and nanolayered TiAlN/CrN multilayer coatings prepared by reactive direct current magnetron sputtering, Thin Solid Films, 514 (2006) 204-211.

19. Wo, P.C., Munroe, P.R., Vasiliev, M., Xie, Z.H., Alameh, K., Kotov, V., A novel technique for microstructure characterization of garnet film, Optical Materials, 32 (2009) 315-322.

20. Fornies, E., Galindo, R.E., Sanchez, O., Albella, J.M., Growth of CrN_x films by DC reactive magnetron sputtering at constant N_2/Ar gas flow, Surface & Coatings Technology, 200 (2006) 6047-6053.

21. Ehiasarian, A.P., Munz, W.D., Hultman, L., Helmersson, U., Petrov, I., High power pulsed magnetron sputtered CrN_x films, Surface & Coatings Technology, 163-164 (2003) 267–272.

22. Flink, A., Beckers, M., Sjolen, J., Larsson, T., Braun, S., Karlsson, L., Hultman, L., The location and effects of Si in $(Ti_{1-x}Si_x)N_y$ thin films, Journal of Materials Research, 24 (2009) 2483-2498.

23. Ehiasarian, A.P., Hovsepian, P.E., Hultman, L., Helmersson, U., Comparison of microstructure and mechanical properties of chromium nitride-based coatings deposited by high power impulse magnetron sputtering and by the combined steered cathodic arc/unbalanced magnetron technique', Thin Solid Films. 457 (2004) 270-277.

24. Ahmed, M.S., Munroe, P., Jiang, Z.T., Zhao, X., Rickard, W., Zhou, Z.F., Li, K.Y., Xie, Z., Corrosion behaviour of nanocomposite TiSiN coatings on steel substrates, Corrosion Science 53 (2011) 3678-3687.

25. Panjan, P., Merl, D.K., Zupanic, F., Cekada, M., Panjan, M., SEM study of defects in PVD hard coatings using focused ion beam milling, Surface & Coatings Technology, 202 (2008) 2302-2305.

26. Yang, Q., Cai, F., Zhao, L.R., Huang, X., Improving corrosion resistance of CrTiAlN coating by post-deposition treatments, Surface & Coatings Technology, 203 (2008) 606–609.

27. Lankford, J., Comparative study of the temperature dependence of hardness and compressive strength in ceramics, Journal of Materials Science 18 (1983) 1666-1674.

28. Tilbrook, M.T., Paton, D.J., Xie, Z., Hoffman, M., Microstructural effects on indentation failure mechanisms in TiN coatings: Finite element simulations, Acta Materialia 55 (2007) 2489-2501.

Chapter 6 Effect of Carbon ion implantation on nanocomposite Ti-Si-N coatings by metal vapour vacuum arc process

This chapter was submitted as an article in the journal of American Ceramic Society. Whilst all efforts were made to retain the original features of this article, minor changes such as the layout, number formats, and font size and style were implemented in order to maintain consistency in the formatting style of the thesis.

6.1 Abstract

Due to the combination of super hardness, good thermal stability and oxidation resistance, Ti–Si–N nanocomposite coatings have become an excellent candidate for use as high speed machining and cutting tools. Nowadays ion implantation has been employed to alter the near-surface structure and properties of semiconductors, metals and metal alloys without the loss of bulk properties. The present research investigated the effect of carbon ion implantation on the structural, mechanical and tribological properties of the Ti–Si–N coatings prepared by reactive unbalanced magnetron sputtering. Carbon implantation was carried out by metal vapour vacuum arc ion source (MEVVA) with different carbon ion doses. After implantation, the samples were characterized systematically by means of the cross-sectional transmission electron microscopy (TEM), X-ray diffraction (XRD), FIB/SEM, energy dispersive spectrometry (EDS), X-ray photo-electron spectroscopy (XPS), residual stress and nanoscratching measurement and also Rockwell C adhesion strength measurement etc. The results showed that the implantation depth, chemical composition, microstructure, residual stress and friction co-efficient depended strongly on the implanted carbon doses. In addition, a great improvement on the tribological performance was observed with the post-treatment process of carbon ion implantation.

6.2 Introduction

Dry and high speed machining tools manufacturing by economic way are attracting continuing scientific attention. In recent years designing and fabrication of effective cutting,

drilling and drawing tools by physical or chemical vapour deposition (PVD or CVD) techniques have been widely experimented and adopted [1, 2]. In the past decades, TiN coatings have been shown to be particularly promising for use in machining industry owing to their high hardness (20–30 GPa). The recent coating development has turned towards the design of the nanocomposite or nanostructured coatings aiming to further increase the fracture toughness and hardness [3, 4]. Among the new coatings, TiSiN is expected to be an excellent candidate for use in high speed machining conditions, due to its high hardness (<50 GPa), thermal stability, oxidation [5-7] and corrosion resistance [8, 9].

However, the friction coefficient of all these nanoceramic coatings is still high (~0.4 to 0.6) for dry machining, forming and biomedical tools [10-12]. Ion implantation [13, 14] has been found to be an alternative and efficient method to modify surface properties without affecting the originally excellent properties (e.g. high hardness) of in-depth layers. Studies have been carried out on the effect of the implantation of noble-gas ions (Ar+, Kr+, Xe+) [15-18], metal ions [19, 20], carbon [21-23] and nitrogen [24, 25] ions into various substrates for improving adhesion, mechanical and tribological properties in the field of mechanical manufacturing.

The post-treatment of carbon ion implantation has been shown to be of great interest recently for improving the tribological behaviour of hard ceramic coatings with reduced residual stress [26], increased yielding strength, wear resistance and life time of the tools [27, 28]. The application of carbon implantation may modify the structure and chemistry of the surface layer of the ceramic coatings, and impart the coatings self-lubricating ability. However, detailed research about the effect of post-treatment, such as carbon implantation process, on the nanocomposite coatings on steel substrate is still limited. This work has focused on the microstructural, mechanical, adhesion strength and tribological properties of the Ti–Si–N coatings post-treated by carbon ion implantation. This will help to design and fabricate the effective and unique cutting, forming and drilling tools with lower friction and perfect mechanical properties for application.

6.3 Experimental procedure

6.3.1 Deposition details

Nanocomposite TiSiN coatings were deposited onto steel substrate by physical vapour deposition (PVD) using a reactive close-field unbalanced magnetron sputtering system (UDP650, Teer Coatings Ltd., Droit-wich, Worcestershire, UK). The details of the deposition

procedure are given elsewhere [29], and are summarised as follows: prior to deposition, the surface of the steel substrates was bombarded by Ar ions to remove the oxide layer and other contaminants. During deposition a Ti buffer layer, ~0.2 μm in thickness, was first deposited, followed by a TiN transition layer, ~1 μm in thickness. The thickness of the outer TiSiN coating was 2 μm and it was composed of ~50 at.% of Ti, ~10 at.% of Si and ~ 40 at.% of N, as determined by XPS.

6.3.2 Carbon implantation by metal vapour vacuum arc process

The deposited nanocomposite TiSiN hard coatings were post-treated by carbon ion implantation in order to modify their surface properties. The implantation was carried out by using metal vapor vacuum arc (MEVVA) ion source with a solid graphite cathode. Current density during implantation was kept below 20μA/cm^2. The ion energy was fixed at 50 keV, and the dose was varied in the range of 10^{17}-10^{18} ions/ cm^2. All the implantations were carried out at a normal incidence of ions under a vacuum level of 5×10^{-7} Torr. The sample temperature rise during implantation was kept below 200 °C.

6.3.3 Microstructural characterization by TEM

Cross-sectional transmission electron microscopy (TEM) specimens of lowest and highest dosing samples were prepared for clear observation of carbon layer microstructure using FIB system. The fully computerized process is described below: a layer of platinum (~1 μm thick) was deposited onto the surface area to protect the surface from ion-beam damage during the milling processes. A “rough” mill was performed with a beam current of 10,000 pA, in which trenches were cut on both sides of the platinum protective layer to obtain a section of ~3 μm thickness. A number of “fine” mills were performed at reduced currents (5000 to 1000 pA) and the section thinned to ~1 μm. Final mills were carried out at further reduced currents (300 to 100 pA), reducing the thickness of already thinned section down to ~100 nm with electron transparency. The specimen was examined using a field emission gun transmission electron microscope (Philips CM200, Eindhoven, The Netherlands).

6.3.4 Surface structure characterisation

The coating crystal structure of the carbon implanted samples was characterised by grazing incidence XRD (GI-XRD) at the powder diffraction beam line of the Australian Synchrotron. The energy of the synchrotron radiation was 9.0 keV, which corresponds to a wavelength of 0.13 nm at an incidence angle of 1°. The patterns were collected over the 2θ range of 20–80°. The depth of the incidence SR beam was 0.5 μm, according to a formula described elsewhere [30].

Chemical bonding and compositions of all coatings were investigated by XPS. Before analysis, the samples were ultrasonically cleaned in acetone, alcohol and then distilled water, respectively, at room temperature. XPS analysis was then performed on the as-deposited samples with a Kratos-Axis Ultra spectrometer using Mg Kα x-ray radiation (hυ = 1253.6 eV). The accelerating voltage and the emission current of x-ray source were maintained at 12 kV and 12 mA, respectively. The background pressure of analysis chamber was better than 10^{-9} Torr. Samples were mounted using copper tape, with the coating surface normal to the entrance of the hybrid-mode electrostatic lens through a slot (Iris = 0.6 and Aperture = 49). A charge neutraliser was used for data acquisition. XPS spectrum energy scale was calibrated against the copper Cu 2p3/2 (932.67 eV), Ag 3d5/2 (368.27 eV), C1s (hydrocarbon; 284.5 eV) and Au 4f7/2 (83.98 eV). In each sample, a survey scan spectrum was first acquired using pass energy of 80 eV, with a step size of 1 eV. High resolution core level XPS spectra associated with elements Ti, N, C, and Si were then obtained from each sample using pass energy of 10 eV, and a finer step size of 0.1 eV for detail analysis on the bonding states of these elements. After subtracting the background signal of survey spectra by using Shirley base-line method, quantitative analysis of composition of each coating was carried out. Peak identification was performed by referencing to the NIST (V4.0) XPS database.

6.3.5 Rockwell-C adhesion test

The adhesion strength of the coatings was examined by Rockwell-C adhesion test. A standard Rockwell-C hardness tester (DXT-1 hardness tester, Matsuzawa, Japan) was used to induce indentation damage with a maximum load of 150 kgf. Following indentation tests, the failure mode was examined using a field emission scanning electron microscope (FESEM) (FEI Dual Beam XL 820, FEI Inc., Portland, Oregon, USA) and classified according to a widely adopted adhesion strength quality index [31].

6.3.6 Mechanical properties and residual stress measurement

A nanoindentation system (Ultra-Micro Indentation System2000, CSIRO, Sydney, Australia), equipped with a Berkovich indenter, was used to measure the mechanical properties of all the carbon implanted coated samples, according to a method proposed by Oliver and Pharr [32]. Prior to nanoindentation testing, the area function of the indenter tip was calibrated using a fused silica specimen. Nanoindentation tests were carried out under load control with a maximum load of 50 mN. For each test, 20 incremental and 20 decremental steps were used. The maximum penetration depth during the tests was found to be less than 10% of the total coating thickness, which ensured that only the coating properties were measured.

The residual stress of TiSiN coatings was measured using a nanoindenter with a spherical tip of 5 μm in radius (Ultra-Micro Indentation System 2000, CSIRO, Sydney, Australia), based upon a method developed by Swadener et al. [33]. For each specimen five maximum load were used, i.e. 10, 20, 30, 40 and 50 mN. Twenty indentations were performed for each load. The maximum penetration depth was found to be less than 10% of the TiSiN coating thickness during the tests. The key formula used for calculating the residual stress, σR, of the coatings is

$$\boldsymbol{\sigma_R} = \boldsymbol{\sigma_Y}\left(\mathbf{1} - \frac{\mathbf{1.26}}{\boldsymbol{\pi}}\left[\frac{\boldsymbol{a_0}}{\boldsymbol{\sigma_Y}}\frac{\boldsymbol{E_e}}{\boldsymbol{R}}\right]\right) \qquad 1)$$

where σ_Y is the yield stress of the coatings, a_0 the contact radius at the onset of yielding of the coating, E_e the effective Young's modulus of the coatings, and R the indenter radius.

6.3.7 Nanoindentation and observation of sub-surface deformation by FIB-SEM

A FIB microscope (FEI xP200, FEI Company, Hillsboro, OR, USA) was used to reveal the subsurface damage of the coatings by nanoindentation. The procedure has been described elsewhere [34]. First, gallium ion beam was used to mill the specimen surface at a high beam current (6,600 pA) and create a wedge-like trench. The resultant rough cross-section was polished at a medium beam current (1,000 pA) to remove particle deposition and smooth the surface. Finally, the cross-section was imaged at a low beam current (70 pA). Spherical and Berkovich indenter with 500 mN load were used to produce the significant deformation on the coating surface.

6.3.8 Nanoscratching and observation of sub-surface deformation by FIB-SEM

Scratch testing was carried out using a conical indenter of 5 µm tip radius (R) over a load range of 0 – 300 mN at a loading speed of 5 mN/s and sliding speed of 10 µm/s (Ultra-Micro Indentation System 2000, CSIRO, Sydney, Australia). Five scratch tests were performed on each sample. The scratch length was about 300 µm. All tests were run in an air-conditioned laboratory environment at a room temperature of 25°C.The Coefficient of Friction can be found by dividing the Friction Force (i.e. the Lateral Force) by the Normal Force (i.e. the indenter load). The maximum depth of the scratch was calculated from the relative depth difference attained between that at the zero and maximum load.

The scratched surfaces of unimplanted and implanted samples were examined using a field emission scanning electron microscope (FESEM) (Model Fei Nova 230, EI Company, USA). Sectioning and subsurface imaging of samples was carried out using a focused ion beam (FIB) workstation (FEI xP200 focused ion beam microscope, FEI Company, USA).

6.4 Result and Discussion

Fig. 1 & 2 show the cross-section TEM images of the carbon-implanted surface layer of the TiSiN coatings for ion dose of 1017and 1018 ions/cm2 with mapping of the elements respectively. These images can be divided into two regions based on the image contrast – the TiSiN layer and the implantation layer. The thickness of the lowest dose implanted layer was approximately 152 nm, and for the highest dose implanted layer this was approximately 320 nm. The implanted layer was increased with the increase of carbon dosing. Notably, the shape and microstructure of grain growth have changed. Unimplanted TiSiN possesses a nanocomposite structure, which was distorted, however, in the implanted layer, due to high-energy ion bombardment. In the mapping, Cr element was dictated from the tool steel in both samples.

Fig. 3 shows the glancing angle XRD patterns of the samples performed at an incidence angle of 1°. The XRD results of unimplanted TiSiN peak revealed f.c.c. B1 NaCl structure of TiN phase with multiple crystal planes of (111), (200), (220) and (311). There was no peak associated with Si3N4 as it exists as amorphous phase. The intensity of TiN (111) and (220) peaks were decreased with the increase of the dose of carbon ion implantation. On the other hand, the (220) peak was significantly intensified and sharpened (220) in the highest carbon

dosed sample, probably due to the reduction in the number of structural defects and residual stress [35]. The ion implantation deposits thermal energy into the coating, which may activate the relaxation of structure faults [36]. The fact that the TiN (220) reflection is dominant indicates that a strong fiber-like stress free lattice texture may create due to the ion bombardment. Little or no peak shift was recognized with the increase of carbon implantation dose. In addition, the peak of martensite phase (M) (200) of M42 steel substrate appeared in all the samples.

The chemical bonding information of the implanted carbon atoms is important in order to have a correct understanding of the aforementioned results. The XPS spectrum of Ti 2p was obtained only from the unimplanted TiSiN coated sample (Fig.4a) and it disappeared in the 10^{17} ions/cm^2 carbon layer formation. In the Ti 2p spectra, two pairs of peaks raised from Ti 2p3/2 and Ti 2p1/2 were identified, corresponding to the TiN and TiOx phases at the surface of the unimplanted and the lowest dose implanted samples. TiOx has been formed on these two samples, due to surface confirmation by oxygen. The N 1s XPS of implanted TiSiN sample differs in pattern from the unimplanted samples [37]. The two peaks at ~ 397.5 eV and ~ 398.2 eV raised from C-O-N and TiN respectively and the other peak at ~ 401.5 eV from the Si_3N_4 phase was observed in implanted samples (Fig.4b). For all the four samples, the C1s XPS spectra were similar. After deconvoluting the C 1s core level spectra by a curve-fitting method, two peaks were found at ~284.2 eV and ~285.8 eV, which were from C-C and C-N bond, respectively. The other peak at ~288.4 eV came from C-O bond (Fig. 4c). No carbon peak was found in the unimplanted sample.

The mechanical properties of the unimplanted and implanted TiSiN samples, including elastic modulus, hardness, residual stress, and friction coefficient, were obtained from nanoindentation and given in Table 1. The friction coefficient and all other parameters of the unimplanted TiSiN sample were the highest among all the samples. A decrease of these parameters was observed with the increase of carbon dosing on TiSiN. The properties of the nanocomposite TiSiN coating were affected due to the thin softer carbon amorphous layer formation on the surface.

The hardness and elastic modulus were significantly influenced by the carbon implantation. On the other hand, the compressive residual stress remained unchanged up to $3x10^{17}$ ions/cm2 dosed sample, then decreased slightly within the medium carbon dosing, and finally dropped quickly for sample C5 to only ~20% of that in the unimplanted sample. This change of residual stress could be the result of the removal of structural defects within the carbon layer formation [38].

The friction curves of all the samples, obtained from the nanoscratch experiment, are given in Fig. 5. The friction coefficient of the unimplanted TiSiN sample was measured to be ~0.32 at low normal load, which decreased to a minimum of ~0.25 at around the normal load of

50 mN, then increased with the increasing normal load, reaching 0.34 at the normal load of 300 mN. With the implantation of carbon, the friction coefficients demonstrated a continuous decrease with the increase of carbon dosing, while showing normal loading dependence curves which are similar to that of the unimplanted sample. For example, at 300 mN normal load the friction coefficient decreased with the increase of carbon dosing, reaching 0.15 for the sample C5, i.e. a reduction over 50% at the highest carbon implanted sample. The lubrication effect was significantly improved due to the amorphous carbon layer formation over the surface which imparts the coating surface with self-lubrication properties. It is interesting to note that, by increasing the implantation dose from $1xe^{17}$ to $1xe^{18}$, the friction coefficient improved only at low load and high load, but is remain about the same between 90-140 mN. This might happen because of the accumulation of the critical load to create significant tensile stress for cracking occur at the sides of the scratch track.

Fig. 6 shows the results of the Rockwell-C adhesion test. The damage pattern of these samples was examined and their adhesion strength was subsequently ranked on a scale of HF1-HF6 (good to poor quality) (HF1-HF6 should be labelled in each of image (a-f)). In the unimplanted TiSiN sample, severe damage was seen in the central region of the indent along with delamination at the edge in TiSiN, suggesting a marked decrease in the damage resistance and adhesion of the coating. It has been reported that the adhesion strength depends significantly on the compressive residual stress of the structure [39], a low compressive stress favours good adhesion However, with the soft amorphous carbon layer the impact on the highest ion implanted sample generated surrounding cracks with delamination, which consequently counteracted the effect of residual stress. The best adhesion was observed in the middle carbon dosed sample of 5x1017ions/cm2.

To develop a better understanding of the damage resistance of carbon implanted nanocomposite TiSiN coatings under the influence of residual stress, indentation results were examined with the assistance of FIB, as showed in Fig.7 (spherical indentation) and Fig.8, (Berkovich indentation). The mode of damage pattern was similar for the two indenters. For the as-deposited sample, large damages were observed in the form of both ring cracks and lateral cracks. Ring cracks apparently initiated at the contact edge and propagated into the coating. On the other hand, lateral cracks formed at the interface between the TiSiN coating and the TiN interlayer (Fig. 7(a) &8(a)). For the lowest dosed sample, there were fewer ring cracks, and they were smaller in size. However, both the number and the size of the lateral cracks were similar to those in the as-deposited sample (Fig. 7(b)). With carbon dosing increasing to medium (i.e., a decrease in residual stress), microcracks became dominant, and there were fewer large ring cracks and lateral cracks. For the highest implanted sample, neither ring crack nor lateral crack was visible, and microcracks exist in the structure, leading to a highly deformed indentation site. The lowest compressive residual stress has failed to hold the structural integrity of the coating in

this case. The pre-existing compressive residual stress in the plane of a film increases the resistance to the propagation of shear cracks through the inter-columnar boundaries resulting in an increase in shear fracture strength or toughness of the coating[40].

As mentioned before, scratch testing revealed a decrease of friction coefficient with the increased carbon dosing, which would be influenced by the detailed deformation and cracking mechanism within the coating and the substrate. To reveal the subsurface crack patterns, two different cross-sections were prepared using FIB. The first one is parallel to the scratch direction, at the profile of the maximum scratch depth. The second one is perpendicular to the scratch direction, having a profile with the maximum scratch depth at the centre (Fig. 9). These subsurface images showed that ring cracks, starting at the trailing edge of the indenter, were dominant at the parallel subsurface of the scratch track. In addition, lateral cracks followed by ring cracks were observed at the normal direction of the scratch track. No delamination was observed at the coating/substrate interface. A ring crack was observed to initiate on the coating surface, propagating into the coating away from the sliding direction at an acute angle to the surface. Lateral cracks in the middle of the coating were always responsible for final coating failure (spallation) during scratching [41]. The initiation and propagation of this ring crack can be explained by a 3D model [42], in which the maximum tensile stress is generated at the trailing edge of the indenter, resulting in ring cracks. Similar to the nanoindentation and adhesion damage results, the cracks formed by nanoscratching followed the same trends for the middle dosed carbon implantation, i.e., in sample C3 the minimum damage was observed. This is possibly because that, lower friction will result in a reduction of the loading induced stress, which helps maintaining the integrity of the coating. However, with further increase of implantation dosage the structure damage within the coating layer will be resulted in reduced adhesion strength.

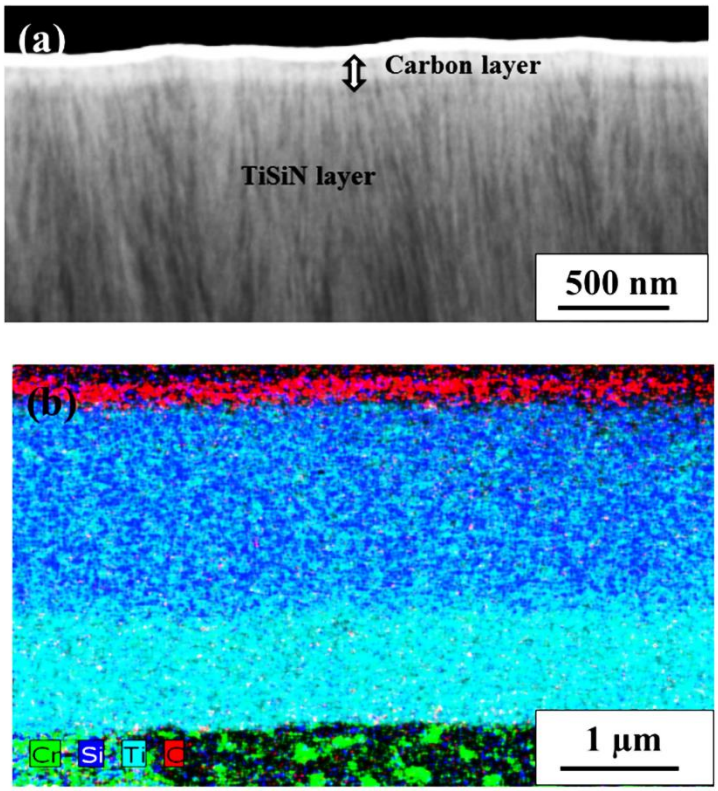

Figure 1: (a-b) Cross-sectional bright field transmission electron micrograph (X-TEM) of carbon implanted (lowest dosing) TiSiN coating on steel with mapping of elements

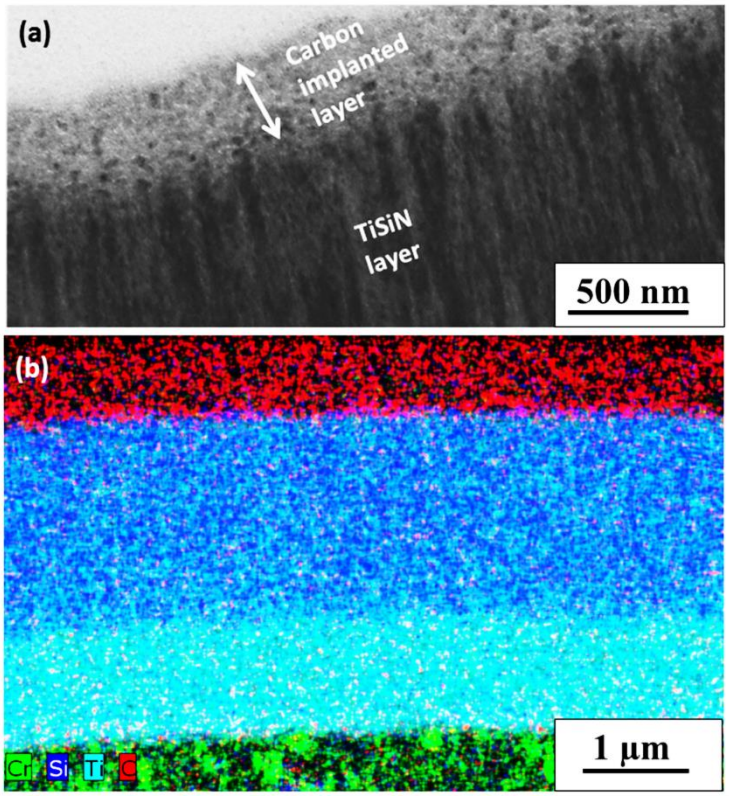

Figure 2(a-b): Cross-sectional bright field transmission electron micrograph (X-TEM) of carbon implanted (highest dosing) TiSiN coating on steel on steel with mapping of elements.

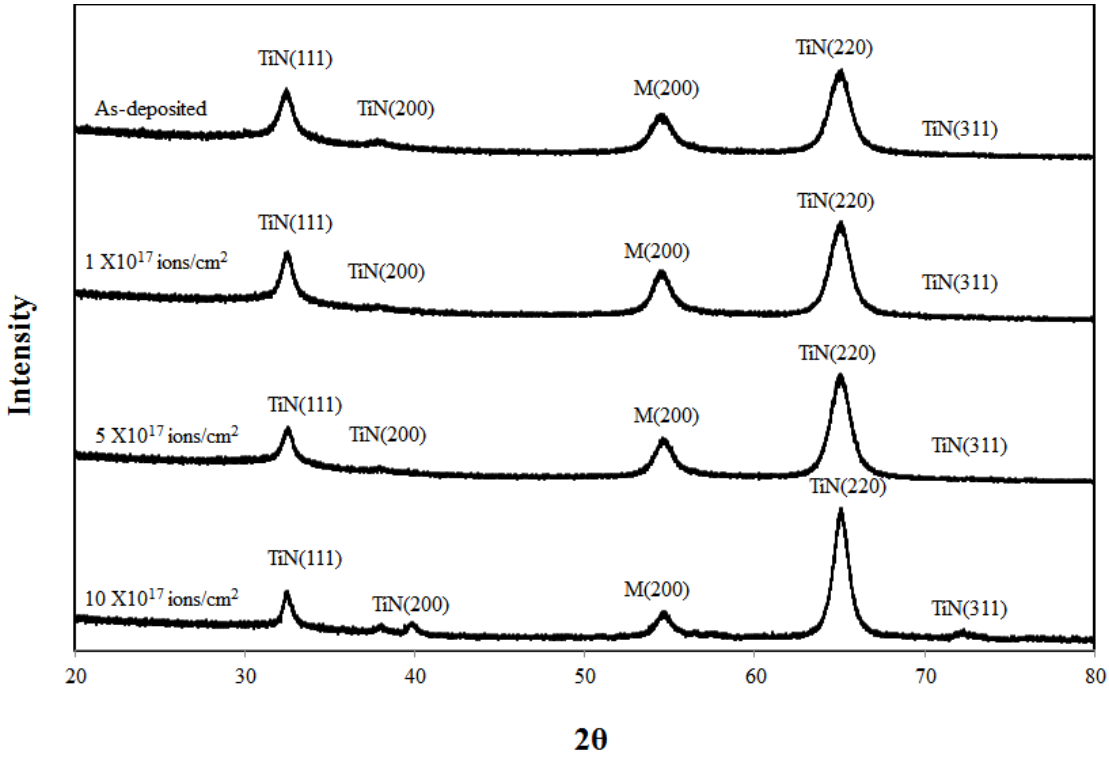

Figure 3: Grazing incidence X-ray diffraction patterns of unimplanted and implanted TiSiN coatings with variation of carbon dosing.Note "M" stands for martensite phase of AISI M42 steel.

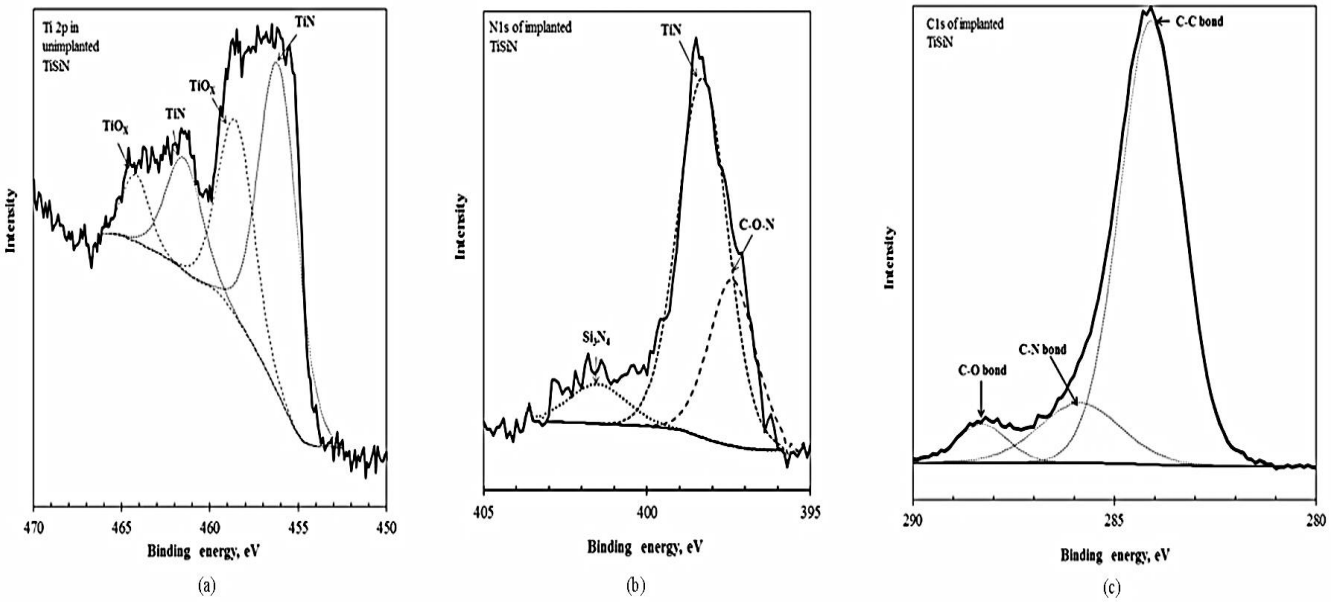

Figure 4: Surface X-ray photoelectron spectroscopy spectra for Unimplanted and implanted TiSiN coated samples: (a) the chemical bonding states of Ti 2p in unimplanted TiSiN samples; (b) the chemical bonding states of N 1s in implanted TiSiN samples; (c) the chemical bonding states of C1s in implanted TiSiN samples.

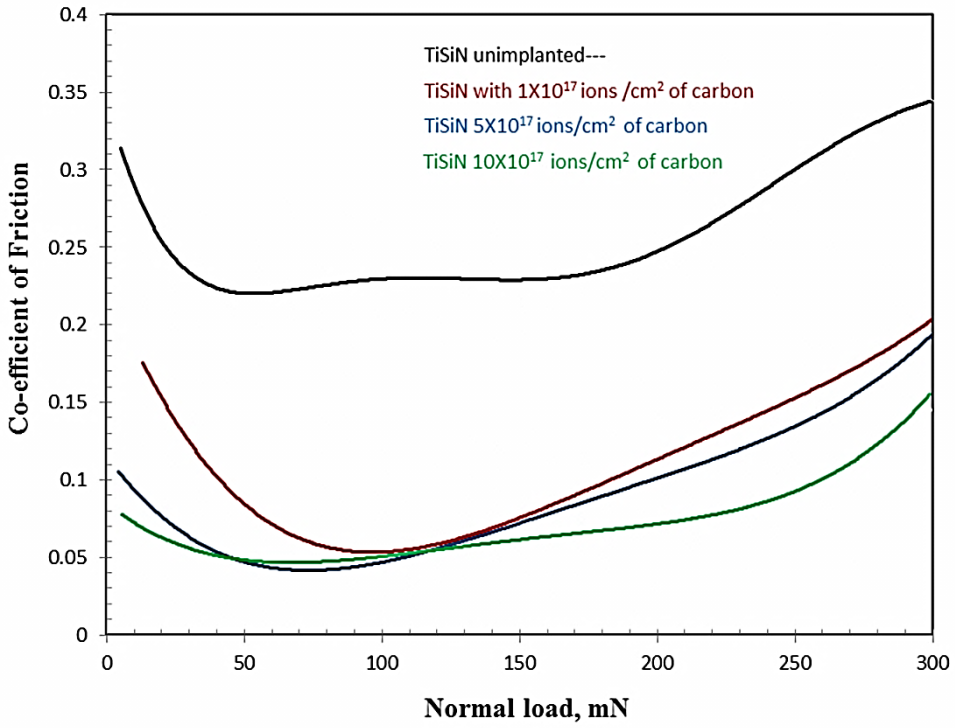

Figure 5: Coefficient of friction .as a function of sliding distance and normal load during nanoscratch testing on the unimplanted and implanted TiSiN coated system. Indenter tip radius: 5µm.

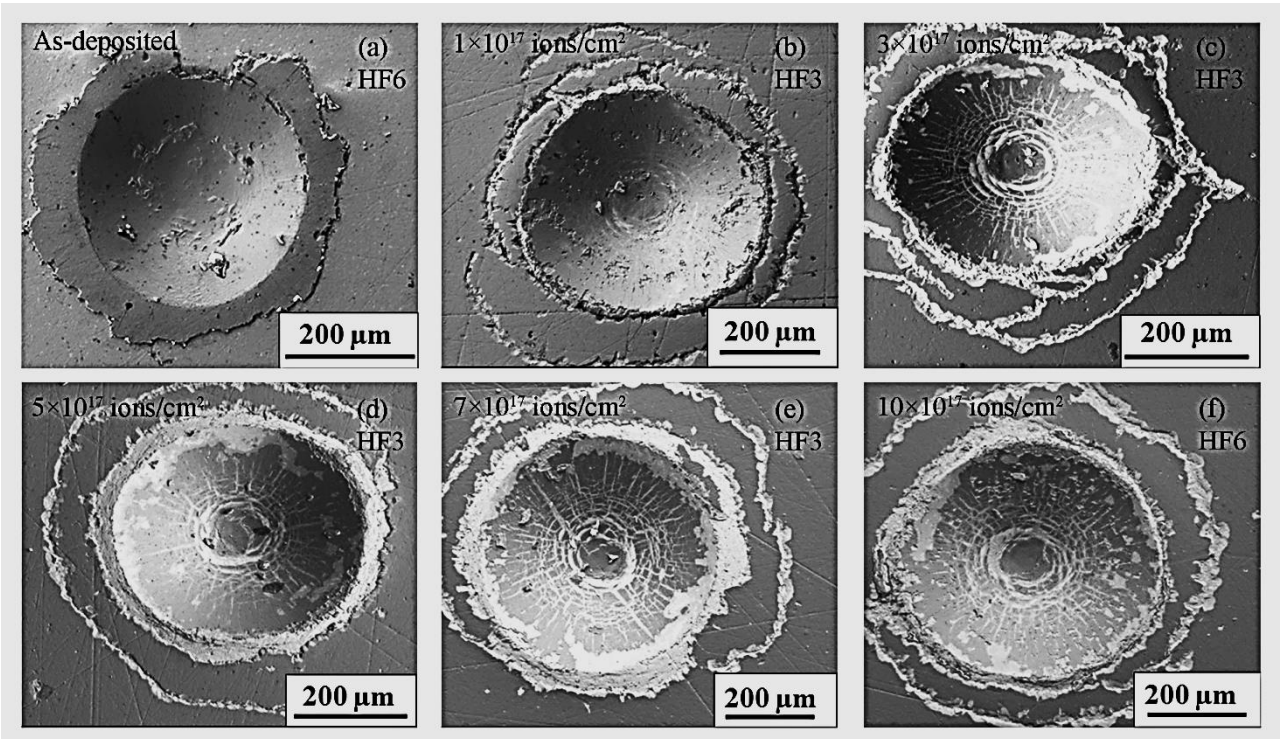

Figure 6: (a-f) Rockwell-C indentation failure patterns of unimplanted and implanted TiSiN coatings on AISIM42 steel substrates.

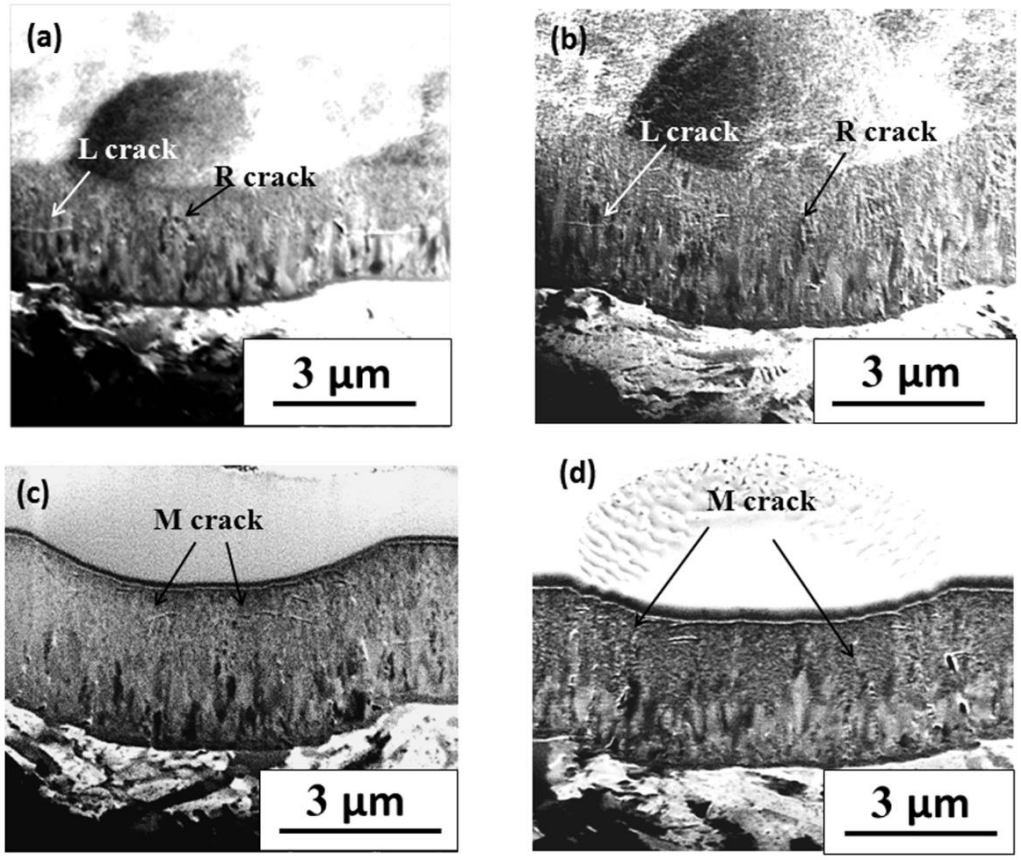

Figure 7: FIB cross-sectional micrographs of spherical indents in the (a) unimplanted sample, (b) C1, (c) C3 and (d) C5. R, L and M stand for ring crack, lateral crack, and microcrack, respectively.

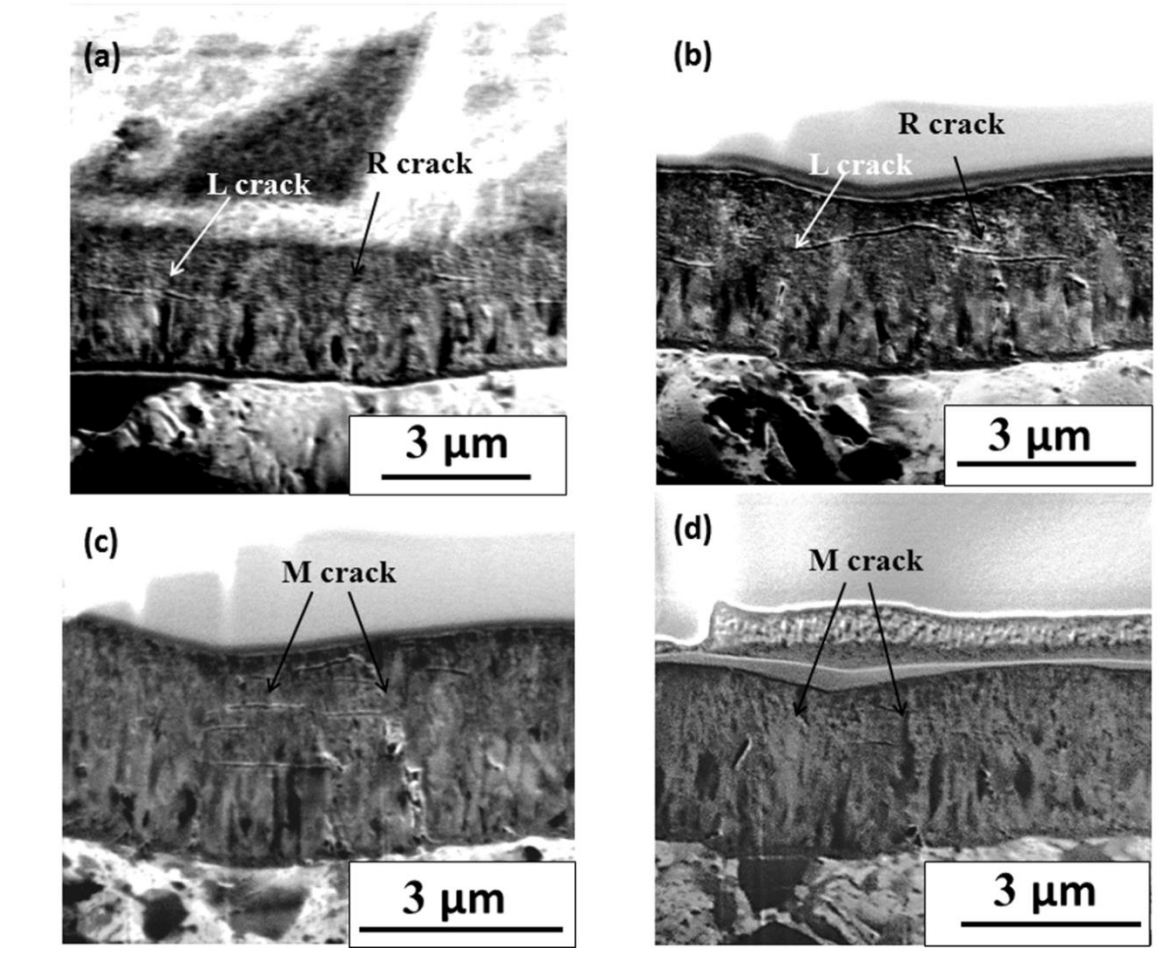

Figure 8: FIB cross-sectional micrographs of Berkovitch indents in the (a) unimplanted sample, (b) C1, (c) C3 and (d) C5. R, L and M stand for ring crack, lateral crack, and microcrack, respectively.

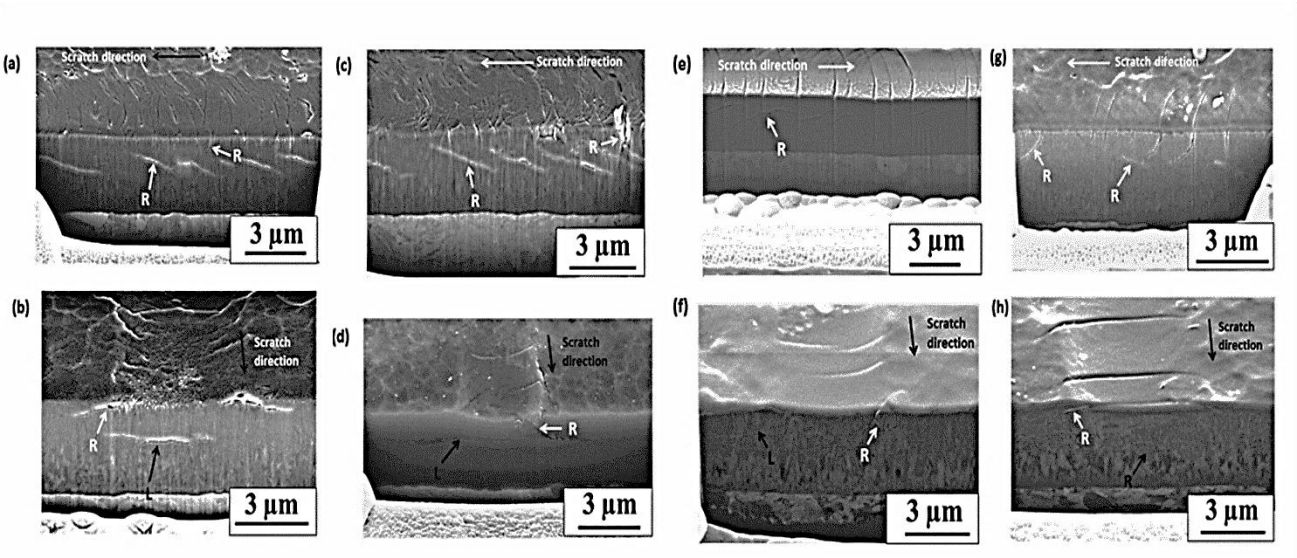

Figure 9: FIB cross-sectional micrographs of nanoscratch damage in the (a-b) unimplanted TiSiN coated sample, (c-d) C1, (e-f) C3 and (g-h)C5 ; the cross section being parallel (upper) and normal (lower) to the direction of the scratch. R and L stand for ring crack and lateral cracks, respectively.

Table 1 Properties of nanocomposite TiSiN films with variation of Carbon dosing

Sample	Carbon dosing ($x10^{17}$ ions/cm^2)	Elastic Modulus(GPa)	Hardness(GPa)	Residual stress(GPa)	Co-efficient of friction
Unimplanted TiSiN	-	510	53	10	0.36
Sample C1	1	340	40	10	0.23
Sample C2	3	315	34.7	10	0.21
Sample C3	5	285	30.7	9.4	0.20
Sample C4	7	267	28.6	4.5	0.18
Sample C5	10	258	27	2.2	0.15

6.5 Conclusion

The structural, mechanical and tribological properties of TiSiN coatings implanted with high-energy carbon ions have been studied and following conclusion were drawn:

(1) After the carbon ion implantation, a thin carbon-implanted surface layer with a thickness of 152–320 nm was formed on the top of the TiSiN bulk coatings. The microstructure of the top layer was changed with the formation of amorphous carbon layer and forming a lubricating layer on the top of the films.

(2) The results showed that the coatings post-treated with carbon ion implantation exhibited an excellent tribological performance in terms of friction co-efficient with decreasing yield strength and hardness. The friction coefficient dropped to 0.18 with the lowest carbon ion dose of 1×10^{17} ions/cm^2 and to 0.13 with the highest dose of 10×10^{17} ions/cm^2.

(3) The residual stress is reduced with the increase of carbon ion implantation .Meanwhile the adhesion strength, indentation subsurface damage and nanoscratching sub surface damage showed the best condition in the medium dosing of carbon ions on the TiSiN samples.

6.6 References

1. Beake, B.D., G.S.F. Rabinovich, G.S.F., S.C. Veldhuis, S.C., S.R. Goodes, S.R., Coating optimisation for high speed machining with advanced nanomechanical test methods, Surface & Coatings Technology, 203 (2009) 1919-1925.

2. Pesch, P., Sattel, S., Woestmann, S., Masarczyk, P., Herden, K., Stucky, T., Martense, A., Ulriche, S., Holleck, H., Performance of hard coated steel tools for steel sheet drawing, Surface & Coatings Technology, 163-164 (2003) 739-746.

3. Martínez-Martínez, D., López-Cartes, C., Fernández, A., Sánchez-López, J.C., Influence of the microstructure on the mechanical and tribological behavior of TiC/a-C nanocomposite coatings, Thin Solid Films, 517 (2009) 1662-1671.

4. Zeng, Z.X., Zhou, Y., Zhang, B., Sun, Y., Zhang, J., Designed fabrication of hard Cr-Cr_2O_3-Cr_7C_3 nanocomposite coatings for anti-wear application, Acta Materialia, 57 (2009) 5342-5347.

5 P.J. Martina, P.J., A. Bendavid, A., J.M. Cairney, J.M., Nanocomposite Ti–Si–N, Zr–Si–N, Ti–Al–Si–N, Ti–Al–V–Si–N thin film coatings deposited by vacuum arc deposition. Surface & Coatings Technology, 200 (2004) 2228-2235.

6. Barshilia, H.C., Deepthi, B., Prabhu, A.S.A., Rajam, K.S., Superhard nanocomposite coatings of TiN/Si_3N_4 prepared by reactive direct current unbalanced magnetron sputtering, Surface & Coatings Technology, 201 (2006) 329-337.

7. Zhang, C.H., Lu, X.C., Wang, H., Luo, J.B., Shen, Y.G., Li, K.Y., Microstructure, mechanical properties, and oxidation resistance of nanocomposite Ti-Si-N coatings, Applied Surface Science, 252 (2006) 6141-6153.

8. Chang, C.L., Lin, C.T., Tsai, P.C., Ho, W.Y., Liu, W.J., Wang, D.Y., Mechanical and corrosion properties of (Ti,Si)N coating synthesized by cathodic arc plasma evaporation. Surface & Coatings Technology, 202 (2008) 5516-5520.

9. Chang, C.L., Wu, C.W., Tribological and corrosion behaviors of TiSi(N,O) coatings prepared by cathodic arc plasma deposition, Thin Solid Films, 2009.517 (2009) 5219-5223.

10. Chang, C.L., Hsieh, T.J., Effect of C_2H_2 gas flow rate on synthesis and characteristics of Ti-Si-C-N coating by cathodic arc plasma evaporation, Journal of Materials Processing Technology 209 (2009) 5521-5526.

11. Cheng, Y.H., Browne, T., Heckerman, B., Meletis, E.I., Mechanical and tribological properties of nanocomposite TiSiN coatings Surface & Coatings Technology, 204 (2010) 2123-2129.

12. Serro, A.P., Completo, C., Colaço, R., Dos Santos, F., Lobato da Silva, C., Cabral, J.M.S.,

Araújo, H., Pires, E., Saramago, B., A comparative study of titanium nitrides, TiN, TiNbN and TiCN, as coatings for biomedical applications, Surface & Coatings Technology, 2009 203 (2009) 3701-3707.

13. Shum, P.W., Li, K.Y., Shen, Y.G., Improvement of high-speed turning performance of Ti-Al-N coatings by using a pre-treatment of high-energy ion implantation, Surface & Coatings Technology, 198 (2005) 414-419.

14. Y.F. Xu, Y.F., P.W. Shum, P.W., Z.F. Zhou, Z.F., K.Y. Li, K.Y., Effect of high-energy carbon ion implantation on Ti–Al–Si–N coatings by metal vapour vacuum arc, Surface & Coatings Technology, 204 (2010) 1914-1918.

15. Ensinger, W., Lensch, O., Knecht, J., Volz, K., Matsutanid, T., Kiuchi, M., Pitting corrosion of aluminum coated by ion beam assisted deposition of carbon with argon ions at different ion-to-atom arrival ratios, Surface and Coatings Technology, 158-159 (2002) 594-598.

16. P.Budzynski, P., Skuratov, V.A., Kochanski, T., Mechanical properties of the alloy Ti–6Al–4V irradiated with swift Kr ion, Tribology International, 42 (2009) 1067-1073.

17. Pelletier, H., Nelea, V., Mille, P., Muller, D., Mechanical properties of pulsed laser-deposited hydroxiapatite thin films implanted at high energy with N+ and Ar+ ions. Part II : Nano-scratch test with spherical tipped indenter, Nuclear Instruments & Methods in Physics Research B, 216 (2004) 275-280.

18. Perry, A.J., Valvoda, V., Rafaja, D., Williamson, D.L., Sartwell, B.D., On the residual stress and picostructure of titanium nitride films I: Implantation with argon or krypton, Surface & Coatings Technology, 54-55 (1992) 180-185.

19. Tonghe, Z., Yuguang, W., Yenwen, Z., Formation and behaviour of ceramic layer by ion-deposited Ti coating using FMEVAD and Ti and C-dual implantation, Nuclear Instruments & Methods in Physics Research B, 184 (2001) 509-514.

20. Chang, Y.Y., Wang, D.Y., Wu, W.T., Tribological enhancement of CrN coatings by niobium and carbon ion implantation, Surface & Coatings Technology, 177-178 (2004) 441-446.

21. Chang, C.L., Wang, D.Y., Characterization of surface enhancement of carbon ion-implanted TiN coatings by metal vapor vacuum arc ion implantation, Nuclear Instruments & Methods in Physics Research Section B, 194 (2002) 463-468.

22. Shum, P.W., Zhou, Z.F., Li, K.Y., A study of the structural, mechanical and tribological properties of Ti-Al-N coatings Post-treated by carbon Implantation, Advanced Materials Research, 75 (2009) 7-12.

23. Shum, P.W., Zhou, Z.F., Li, K.Y., Enhancement of adhesion strength and tribological performance of pure carbon coatings on Ti-6Al-4V biomaterials with ion implantation pre-treatments, Tribology International, 40 (2007) 313-318.

24. Sharkeev, Y.P., Bull, S.J., Perry, A.J., Klingenberg, M.L., Fortuna, S.V., Michler, M., Manory, R.R., Shulepov, I.A., On high dose nitrogen implantation of PVD titanium nitride, Surface & Coatings Technology, 200 (2006) 5915-5920.

25. Bull, S.J., Sharkeev, Y.P., Fortuna, S.V., Shulepov, I.A., Perry, A.J., Mechanism of TiN-coated tool life by nitrogen implantation, Materials Research Society , 16 (2001) 3293-3303.
26. Bilek, M.M.M., McKenzie, D.R., Tarrant, R.N., Lim, S.H.M., McCulloch, D.G., Plasma-based ion implantation utilising a cathodic arc plasma, Surface & Coatings Technology, 156 (2002) 136-142.
27. Shum, P.W., Zhou, Z.F., Li, K.Y., Optimisation of carbon implantation pre-treatments on the adhesion strength of amorphous carbon coatings on AISI 440C steel substrates, Surface & Coatings Technology, 166 (2003) 213-220.
28. Endrino, J.L., Galindo, R.E., Zhang, H.S., Allen, M., Gago, R., Espinosa, A., Anders, A., Structure and properties of silver-containing a-C(H) films deposited by plasma immersion ion implantation, Surface & Coatings Technology, 202 (2008) 3675-3682.
29. Ahmed, M.S., Zhou, Z., Munroe, P., Li, K.Y., Xie, Z., Control of the damage resistance of nanocomposite TiSiN coatings on steels: roles of residual stress, Thin Solid Films, 519 (2011) 5007-5012.
30. Pang, W.K., Low, I.M., O'Connor, B.H., Sun, Z.M., Prince, K.E., Oxidation characteristics of Ti_3AlC_2 over the temperature range 500–900° C, Materials Chemistry & Physics, 117 (2009) 384–389.
31. Heinke, W., Leyland, A., Matthews, A., Berg, G., Friedrich, C., Broszeit, E., Evaluation of PVD nitride coatings, using impact, scratch and Rockwell-C adhesion tests, Thin Solid Films, 270 (1995) 431-438.
32. Oliver, W.C., Pharr, G.M., Measurement of hardness and elastic modulus by instrumented indentation: Advances in understanding and refinements to methodology, Journal of Materials Research, 19 (2004) 3-20.
33. Swadener, J.G., Olivas, E.R., Nanoindentation measurement of surface residual stresses in particle-reinforced metal matrix composites, Scripta Materialia, 54 (2006) 263-268.
34. Wo, P.C., Munroe, P.R., Vasiliev, M., Xie, Z.H., Alameh, K., Kotov, V., A novel technique for microstructure characterization of garnet film, Optical Materials, 32 (2009) 315-322.
35. Mayrhofer, P.H., Mitterer, C., Hultman, L., Clemens, H., Microstructural design of hard coatings, Progressive Materials Science 51 (2006) 1032-1114.
36. Manory, R.R., Perry, A.J., Rafaja, D., Nowak, R., Some effects of ion beam treatments on titanium nitride coatings of commercial quality, Surface and Coatings Technology 114 (1999) 137–142.
37. Ahmed, M.S., Munroe, P., Jiang, Z-T, Zhao, X-P, Rickard, W., Zhou, Z-F, Li, L.K.Y., Xie, Z. Corrosion behaviour of nanocomposite TiSiN coatings on steel substrates, Corrosion Science, 53 (2011) 3678-3687.
38. Manory, R.R., Mollica, S., Ward, L., Purushotham, K.P., Evans, P., Noorman, J., Perry, A.J., The effects of MEVVA ion implantation on the tribological properties of PVD-TiN films deposited on steel substrates, Surface and Coatings Technology , 155 (2002) 136-140.

39. Zhang, S., Bui, X.L., Zeng, X.T., Li, X., Towards high adherent and tough a-C coatings, Thin Solid Film, 482 (2005) 138- 144

40. Bhowmick, S., Jayaram, V., Biswas, S.K., Deconvolution of fracture properties of TiN films on steels from nanoindentation load–displacement curves, Acta Materialia, 53 (2005) 2459-2467.

41. Xie, Z., Singh, R., Bendavid, A., Martin, P.J., Munroe, P.R., Hoffman, M., Contact damage evolution in a diamond-like carbon (DLC)coating on a stainless steel substrate, Thin Solid Films, 515 (2007) 3196-3201.

42. Wo, P.C., Munroe, P., Xie, Z, Zhou, Z., Li, K.Y., Three-dimensional Visualization of Scratch-Induced Subsurface Damage in TiSiN/TiN Multilayer Coating Using Focused Ion Beam–Scanning Electron Microscopic Tomography Technique, Journal of American Ceramic Society, 94 (2011) 1598- 1604.

7 General discussion

In this research project, the structural, mechanical and corrosion resistance properties of nanocomposite TiSiN coatings have been characterized to determine the effect of thermal annealing and carbon ion implantation. Techniques were developed to characterize the controlled structure, surface chemistry, deformation and damage mechanism and successfully applied to the qualitative and quantitative determination of residual stress and its effect on the damage mechanism and corrosion morphology of the coatings.

The key point of the coatings is synthesizing the nanocomposite microstructure, by the process control deposition through the unbalanced magnetron sputtering process. The thermodynamic driving force which provide the perfect process parameters for nanostructured deposition on tool steel substrate. The applied background pressure lower than 2×10^{-6} Torr and a bias voltage of -500 V was used to bombard the substrate for removing the oxide layer and impurities on the surface. During deposition, the bias voltage was reduced to -60 V, and the working pressure of Ar/N_2 mixed gas was fixed at 1.3×10^{-3} Torr. A Ti buffer layer of ~0.22 μm in thickness and a TiN transition layer ~1 μm in thickness were deposited primarily to improve the adhesion of the TiSiN coatings to the substrates. The substrates were rotated at a fixed speed of 10 rpm to obtain homogenous composition through the coatings. The surface temperature of the central heater (5 kW) was kept at 550 °C during deposition. The tool steel substrate temperature was measured to be 400 °C. The coating composition was adjusted by controlling the sputtering power applied to each target. The resultant TiSiN coatings were ~3 mm in thickness and composed of ~40 at.% of Ti, ~10 at.% of Si, and ~50 at.% of N. The deposition process followed by the thermal annealing modifies the surface chemistry and the mechanical properties of the coatings. After deposition, the coating samples were annealed for 3 h in a vacuum furnace ($1x10^{-6}$ Torr) at 400°, 500°, 600°, 700°, 800°, and 900°C, respectively. The microstructure of both the as-deposited and samples annealed at 800° and 900°C was examined using FIB. For all these coatings, a TiN transition layer is visible underneath the outer nanostructured TiSN coating is. The TiN layer is bonded to the steel substrate by a thin Ti buffer layer. No significant change in microstructure can be observed with the increasing thermal annealing temperature.

The surface composition and the crystalline phases were characterized by the XPS and XRD methods respectively. The XRD analysis showed the expected peaks corresponded to (1 1 1), (2 0 0), (2 2 0) and (3 1 1) crystal planes of cubic B1 NaCl-type TiN crystalline phase. The (220) peak is sharpened and shifted for the stress relaxation. The oxide phase is formed at

900°C in annealed sample ensured by XPS. The oxide phase consequently affected the mechanical properties of the nanocomposite coatings. During thermal annealing, atoms in the as-deposited locations moved to less energetic, stable positions, driven by the reduction of strain energy introduced during film growth. The exact extent of structural recovery apparently depends on the annealing temperature. The residual stress is measured by the nanoindentation technique with spherical indenter adapting the methods developed by G. Swadener et al. The thermal stress distribution has been demonstrated through finite element analysis. Compressive residual stress, as high as ~10 GPa, was measured for the as-deposited TiSiN coatings, and the magnitude of residual stress in the as-deposited coatings can be reduced up to ~1 GPa by thermal annealing at 900°C. The hardness of the coating was regulated by the Hall-Petch effect. A marked decrease in hardness for the sample annealed at 900 °C apparently resulted from the formation of a thin, soft TiO layer at the outer surface of the TiSiN coating. Beneath the thin TiO layer, the mechanical properties of the TiSiN coating would remain comparable to that of the samples annealed at lower temperatures, indicated by their similar microstructure in this work. The reduction of hardness was also attributed to both a decrease in dislocation density and the growth of new, stress-free grains.

The damage mechanism and the coating adhesion strength affected by the residual stress, has been characterized by the FIB-SEM of crack morphology and Rockwell C test of the as-deposited and thermally annealed samples. The microstructural deformation was performed by the nanoindentation technique. The observation showed that residual stress played a crucial role in controlling both the damage resistance and adhesion of the nanocomposite coatings on steel substrate. With the presence of high residual stress, the coating behaved in a rather brittle manner, manifested by the formation of relatively large ring and lateral cracks. By reducing the residual stress, the rotation and/or sliding of nano-sized TiN grains was supposed to be activated in the composite structure, demonstrated by the formation of an increasing number of microcracks beneath the indentation. Considerable energy was dissipated and the damage resistance of the coatings was found improved by reducing of residual stress. A further reduction in residual stress may weaken the ability of the nanocomposite structure to arrest the cracks and create widespread microcracks that would adversely affect the damage resistance of the coatings.

The grain shearing, the residual stress and the mechanical damage have a noticeable effect on the corrosion morphology of the coatings. The corrosion morphology of the highest and lowest stressed coatings have been characterized by the immersion test for 96 hours followed by nanoindenation and finite element analysis of the stress distribution at corrosion sites of the coatings. Detailed mechanistic insights into the mechanism of initiation and propagation of corrosion and the factors that control the expansion of pitting in nanocomposite coated steels were investigated. In this research, FIB, along with XRD, X-ray photoelectron

spectroscopy (XPS) and nanoindentation testing, were used to characterise the microstructural evolution in both surface and subsurface after corrosion tests and determine key factors that control the corrosion process. The change of mechanical properties of the coatings under the influence of corrosion was quantified, and the effect of residual stress on the corrosion progression was also clarified by finite element analysis (FEA).

Surface imperfections, such as pinholes and microparticles, are often found in PVD prepared ceramic coatings, and these defects played an important role in the initiation and expansion of corrosion damage in the coatings in corrosive solutions. The thin oxide layer formed during annealing was observed to act as a barrier to restrict lateral expansion and merging of localised corrosion. It may explain why the annealed samples showed greater Young's modulus and hardness than the as-deposited after eight days corrosion tests. The propagation of cracks induced by localised corrosion was suppressed by high compressive residual stress in the as-deposited coatings. In contrast, the corrosion cracking occurred in low residual stressed sample with little resistance preferentially through structural defects, i.e., the boundaries of exposed columnar TiN grains and the interface between sublayers, causing appreciable damage around the pinholes. The FEA model demonstrated that the residual stress was more effective in resisting the infiltration of corrosive agents at an early stage of corrosion development. The maximum precent area reduction was noted to occur near the cavity tip, in particular for the shallow cavities or pits, indicating the residual stress played a critical role in resisting the corrosion advance.

Corrosive agents may penetrate into the ceramic coatings through deposition defects, such as pores and micro-particles and attack the metal substrates. Passive oxide layer was reported to form on the surface of both columnar CrN and nanocomposite TiSiN coating in previous research. The integrity of the oxide layer is critical to amend the structural defects and restore the ability of the coated metals against corrosion. The nature of the oxide layer formed on both types of coatings and its role in corrosion prevention was compared. The surface bonding structure of the coatings was probed by X-ray photoelectron spectroscopy (XPS). The oxide layer formed on the surface of CrN coatings more effectively compared to TiSiN, isolated such defects from the corrosive agents, enabling a greater resistance to corrosion. Potentiodynamic polarisation measurements were conducted to determine the corrosion resistance of the coated steels. The surface morphology before and after polarisation measurements was examined by electron microscopy to allow investigation of the roles of surface oxide layers in controlling the corrosion resistance of the coatings. In addition, nanoindentation was conducted, in combination with immersion tests and subsurface observations, to clarify how prior mechanical damage regulated the corrosion resistance of the coated steels. Through the shear sliding of columnar grains, the open cracks were avoided in the CrN coatings, preventing the steel substrates from corrosion damage. In contrast, open cracks

occurred extensively in the TiSiN coatings. These cracks formed a passage for corrosive agents to move through the coatings, leading to severe corrosion damage in the substrates.

Finite element analysis was carried out to visualize the stress fields developed in the coatings during indentation and correlate the observed cracks in both TiSiN and CrN coatings with stress concentrations in them. The surface and subsurface structures of the indents was investigated with assistance of a FIB microscope to generate localised cross-sections for both the reference and corroded samples before and after immersion tests. For the reference TiSiN sample, intensive cracks were observed in the form of ring and lateral cracks. Ring cracks apparently initiated near the surface and propagated into the coating. Following the immersion test severe surface and subsurface corrosion damage was observed, presumably caused by the penetration of corrosive agents through the open crack networks in the TiSiN coating into the substrate. By comparison for the CrN sample, the shear sliding occurred between the vertically aligned columnar grains in the coatings under indentation loading. No open cracks appeared and the structural integrity was maintained. Consequently, no corrosion damage occurred at the indented sites in the CrN coated steel. The experimental results demonstrated that both the presence of a surface oxide layer, the deformation mode and the residual stress played significant roles in controlling the corrosion damage of ceramic coatings on steels. The oxide layer formed on the surface of CrN coatings and the shear sliding of columnar grains with lower stress effectively blocked open cracks and isolated defects from the corrosive agents, enabling a greater resistance to corrosion. In contrast, open cracks occurred extensively in the higher stressed TiSiN coatings. These cracks formed a passage for corrosive agents to move through the coatings, leading to severe corrosion damage in the substrates.

Ion implantation has been found to be an alternative and efficient method to modify surface properties without affecting the originally excellent properties (e.g. high hardness) of in-depth layers. Many studies have been carried out on the effect of the implantation of noble-gas ions (Ar+, Kr+, Xe+), metal ions, carbon and nitrogen ions on various substrates for improving adhesion, mechanical and wear resistance properties in the field of mechanical application. The post-treatment of carbon ion implantation has been shown to be of great interest recently for improving the tribological behaviour of hard ceramic coatings with reduced residual stress, yielding increased wear resistance and life time of the tools. The application of carbon implantation may modify the structure and chemistry of the surface layer of the ceramic coatings to impart self-lubricating ability to them.

The compressive residual stress was reduced in TiSiN coating with the increase of carbon dosing from the as-deposited no carbon dosing to highest carbon dosing sample. To develop a complete understanding of the damage resistance of implanted nanocomposite TiSiN coatings under the influence of residual stress, subsurface damage was examined with the assistance of sub-surface FIB observation. The damage was formed by both Berkovich and

spherical nanoindentation. The mode of damage pattern are bit same for two indenters. For the as-deposited sample, large cracks were observed in the form of ring and lateral cracks. Moreover, lateral cracks formed at the interface between the TiSiN coating and the TiN interlayer. For the lowest dosed sample, ring cracks were reduced in terms of number and magnitude, but the lateral cracks remained. With carbon dosing increasing to medium (i.e., a further decrease in residual stress), microcracks became increasingly pervasive relative to the large ring and lateral cracks. For the highest implanted sample, microcracks were excessive in the structure, leading to a highly deformed indentation site. The lowest compressive residual stress has failed to hold the structural integrity of the coating in this case.

Scratch testing reveals a decrease of friction coefficient with carbon dosing, indicating that deformation that results in the film and the substrate contributes to this decrease. To reveal the subsurface crack patterns, cross-sections were prepared both parallel (at positions equating to normal loads of 290 mN) and perpendicular (at positions equating to normal loads of 290 mN) to the scratch direction. Ring cracks, start at the trailing edge of the indenter, are dominant at the parallel subsurface of the scratch track. In addition, lateral cracks followed by ring cracks are observed at the normal direction of the scratch track. No delamination is observed at the coating/substrate interface. A ring crack is observed to initiate on the coating surface, propagating into the coating away from the sliding direction at an acute angle to the surface. Like mechanical damage pattern, sever microcracks observed by nanoscratching in highest dosed carbon implanted sample.

8 Conclusion and future outlook

The present research provides some ideas and knowledge which can be used in nanocomposite coating design in applications involving cutting, drilling, milling and forming application with unique and superior mechanical properties and corrosion resistance. The residual compressive stress is the inevitable key part of the performance of the coating in terms of mechanical properties. The residual stress is the structural and growth defect of coatings introduced during processing. It was found and modelled that the intrinsic component of residual stress was considerably greater than thermal component of the nanostructured coatings. Intrinsic stress can be reduced significantly by the thermal annealing. The extent of stress relaxation depended on thermal annealing temperature. Thermal annealing at temperatures up to 800 °C had little impact on the grain boundary structure and bonding states in TiSiN coatings which was observed by FIB-SEM. Therefore excellent mechanical properties were maintained up to that temperature. Annealing up to 900 °C formed of a thin, ductile TiO layer on the top surface of the coating from the contamination during annealing process. The significant decrease of mechanical properties resulted for the formation of the oxide layer on the surface. In this research, residual stress was measured with the spherical indenters of nanoindentation followed by FEM modelling. The observed result should be compared with the berkovitch indentation and XRD residual stress measurement method. In the future work, the stress will be measured by the berkovitch indentation and XRD $\sin^2\psi$ method and compared for the possibility of more research and study. The microstructural characterization with the thermal annealing will be more precise and accurate with the help of TEM observation for growth of TiN grains.

Through FIB sub-surface observation and nanoindentation damage, this research showed that both the damage resistance and the adhesion strength of nanocomposite TiSiN coatings on steel substrates can be controlled by modulating the residual stress through thermal annealing. The fracture mode changes from brittle to ductile with the decrease of residual stress; but eventually lowest amount of residual stress activates microcracks which adversely affect the coating structural integrity and damage resistance. Adhesion strength of the coating increased with the decrease of residual stress and thermal annealing at certain temperature contaminates the surface with oxide layer which produced severe damage on the surface affecting the adhesion strength severely during processing. The more study will be needed in the future for precise microstructural observation by TEM for visualizing the grain shearing or rotation for fracture toughness at particular crucial stress level.

The subsurface observation by FIB with nanoindentation in 70% nitric acid immersion test was performed and modelled to probe the corrosion evolution of TiSiN coated steels, with a

focus on the roles of surface oxide layer and compressive residual stress in controlling the development of localised corrosion. Pitting corrosion was observed to be dominant in TiSiN coatings, originated from surface defects such as pinholes. Thin oxide layer formed during thermal annealing and inhibited the penetration of acidic solution through the surface of the annealed coating, and consequently an overall protection of the coated steels was observed. Compressive residual stress caused the shrinkage of open corrosion cavities or pores in the coatings, resisted the propagation of corrosion-induced cracks through the sublayer interface and the boundaries of columnar TiN grains. Surface oxidation treatment might be helpful in conjunction with the control of compressive residual stress to provide an effective protection against localised corrosion in PVD-prepared ceramic coatings on steels. The x-ray diffraction in the corrosive solutions provides the necessary information of insitu corrosion crystallography with the change of residual stress which opens the door for future research.

Ceramic coatings such as CrN and TiSiN with two distinct microstructures were studied and the effect of coating surface chemistry and microstructure on the corrosion resistance of the coated steels was clarified with the help of XPS, FIB and Finite element modelling. Chromium oxide was found to be dominant on the surface of the CrN coatings that helped prevent corrosive agents from penetrating through the surface defects and consequently pitting in the coated steels was suppressed. The shear deformation in the columnar structure of CrN coating, reduced the stress concentration and blocked the formation of open cracks during mechanical loading, provided the greater corrosion resistance. Open cracks were observed from shear stress concentration in the TiSiN coatings during mechanical loading. These cracks acted as the pathway of corrosive agents, causing severe damage in the steel substrates. The grain shearing and microstructural observation of these coatings in biochemical solutions will be much probation of future study and research.

In this research, the structural, mechanical and tribological properties of TiSiN coatings post implanted with high-energy carbon ions have been studied. The study has been conducted by differing the carbon ion doses on the coating with the explanation of the result from TEM, XPS, XRD, EDX, Rock-well C test, residual stress and friction measurement. After carbon ion implantation, a thin carbon-implanted surface layer with a thickness of 152–320 nm was formed on the top of the TiSiN bulk coatings. The microstructure of the top layer was changed with the formation of amorphous and lubricating carbon layer on the top of the films. The results showed that the coatings post-treated with carbon ion implantation, exhibited an excellent tribological performance was shown in terms of friction coefficient with dropping of elastic modulus and hardness. The friction coefficient dropped to 0.18 for the lowest carbon ion dose of 1×10^{17} ions/cm^2 and to 0.13 for the highest dose of 10×10^{17} ions/cm^2. The residual stress is reduced with the increase of carbon ion implantation. Meanwhile the adhesion strength, indentation

subsurface damage and nanoscratching sub surface damage showed the desirable condition in the medium dosing of carbon ions on the TiSiN samples. The depth profilometry followed by 3D simulation FEM modelling can be done for better understanding the effect of the depth of carbonaceous layer on the friction and wear. The effective FEM modelling of microstructural change followed by nanoscratching modelling and friction measurement can give significant information and ideas in terms of microstructure, carbon doping and tribological properties in the future.